An infrared study of a sample of optically selected galaxies

Mobasher, Bahram

An Infrared Study of a Sample of Optically Selected Galaxies

by

Bahram Mobasher

A Thesis presented in candidature for the degree of
Doctor of Philosophy at the University of Durham.

February 1987

ABSTRACT

Infrared and optical photometry of a complete sub–sample of 194 galaxies in the *Anglo–Australian Redshift Survey* are presented. The Colour–Redshift diagrams are constructed and used, in a self–consistent manner, to reduce the data to zero–redshift colours at a fixed aperture size. Infrared and optical–to–ir Colour–Luminosity relations are analysed both as a function of morphological type and, in conjunction with published data, as a function of environment.

An infrared Colour–Luminosity relation is found for all galaxy types. The slope seen for E-SO galaxies strengthen the hypothesis that metallicity is the driving factor in the relation at infrared and optical wavelengths. The Colour–Luminosity relations for spirals have slopes that are substantially steeper. The infrared Colour–Luminosity relations of spirals do not vary significantly with Hubble type and the type–dependence of their optical–ir Colour–Luminosity relation disappears when corrections for bulge contamination are made. The results imply that both bulge and disk material have distinct enrichment histories that depend on luminosity in a simple way irrespective of the host galaxy type.

Comparison with stellar synthesis models has revealed that the optical–to–ir colours of spirals are also sensitive to metallicity variations. Moreover, a change in the slope of the initial mass function of star formation (from X=1.35 to X=3) is needed to produce their optical–ir colours over the observed range.

The infrared Colour–Luminosity relation is fairly tight; the intrinsic scatter is small and does not appear to be environmental dependent. The relation for the field E-SOs, analysed in this study, agrees closely with that seen in both the Virgo and Coma clusters and is consistent with recent estimates of the Local Group motion; there is no evidence for any anomalous population of cool stars in the Virgo cluster galaxies. Although promising as a distance indicator in cluster sample, infrared photometry of high precision is required.

The optical–ir relation for spirals, however, has an intrinsic scatter which is most likely due to varying amounts of star formation at a fixed luminosity and bulge–to–disk ratio. An application of the bulge–corrected optical–ir Colour–Luminosity relation to Bothun et al.'s sample of cluster spirals, reduces the scatter in the mean optical–ir colours amongst the clusters. However, the scatter is still larger than that observed in the infrared Tully–Fisher relation.

A detailed analysis of the infrared luminosity function of 'field' galaxies is carried out in conjunction with its optical counterpart. The infrared luminosity function is found to be type–dependent. This implies that the E-SOs and the bulges of spirals have different evolutionary or formation histories. Moreover, the

infrared luminosity function for a given morphological type of galaxies is found to be the same as its optical counterpart shifted by the respective mean optical–ir colours. Regarding this result, it is proposed that galaxies with strong/weak near–ir emission are not very common. The sensitivity of the luminosity function to inhomogeneities in the galaxian distribution is investigated. The best estimates for the luminosity function parameters are then used to predict deep number–magnitude counts at 2.2 μm ($K \sim 18 - 20$ mag).

Acknowledgements

First of all I would like to thank my supervisor Professor Richard Ellis for guiding me through this project and for his continuous encouragement during the course of the work.

I am grateful to Drs. Tom Shanks, Ray Sharples, John Lucey and Warrick Couch for useful discussions over the past years. I am particularly indebted to Dr. Ray Sharples for his help in making the observations and for his continuous criticism of my work.

Dr. Nigel Metcalfe is acknowledged for allowing me to use his data prior to publication. I am indebted to Dr. Richard Fong for first introducing me to cosmology, and for providing financial support at the stage it was needed.

I appreciate useful discussions with my friends and colleagues; Dr. Fred Stevenson, Dr. Brian Boyle, Mr. Iain McClarean and Mr. Tom Broadhurst. I thank them for making my stay in Durham so enjoyable.

I am grateful to Dr. Chris King for supplying me with his stellar synthesis model. Computations in this thesis were carried out on a VAX 11/750 STARLINK computer. I express my thanks to Mr. Alan Lotts for maintaining the system and helping me whenever needed (even at weekends!).

This work was supported financially by a research grant from the 'Committee of Vice–Chancellors and Principals'. The receipt of this grant is greatly appreciated.

Last, but by no means least, I am very grateful to my parents for financing my education and for their encouragement, patience and understanding throughout the years of my studies.

CONTENTS

CHAPTER I

EXTRAGALACTIC ASTRONOMY AT INFRARED WAVELENGTHS

1.1 Introduction

Advances in technology over the last two decades have had a great impact on observational astronomy. It was during this period that a careful study of different regions of the electromagnetic spectrum began. Astronomers today regularly explore the gamma–ray, X–ray, ultraviolet, infrared and radio–wave radiation from stars, composite stellar systems and galaxies as well as the cosmic ray particle energy spectrum. Study of each of these regions is followed by discovery of new objects and an explanation of their physical properties is then required.

By combining observations made at different wavelengths one can study a diverse range of phenomena. For example, observations at radio wavelengths led to the discovery of pulsars and elucidation of complex molecules in our Galaxy. UV radiations originate from stars and gas clouds at temperatures between $3\times10^{4^\circ}$ K and $1\times10^{6^\circ}$ K while X–rays are produced in gas clouds having a temperature between $1\times10^{6^\circ}$ K and $1\times10^{9^\circ}$ K and residing in clusters of galaxies. At the extreme edge of the electromagnetic spectrum is the gamma–ray region which provides information about non–thermal processes such as the collision of cosmic rays with nuclei of gas atoms in space.

Amongst the discoveries in the 'new astronomies' the achievements in the field of infrared astronomy have been substantial. Much attention in recent years has been focused on the nature of the infrared radiations from gas clouds, star clusters and galaxies. Far–infrared radiation is known to be produced in regions of dust at temperatures of 30°–300° K. In our Galaxy such dust is either found in dense clouds in regions of star formation or is ejected from old stars. In external galaxies and quasars, however, this radiation either comes from extensive dust clouds or is due to activities at their nuclei. Near–infrared radiation, on the other hand, can penetrate through gas clouds unattenuated. Also, the near–infrared radiation from composite stellar systems is mainly dominated by cool, old stars of late spectral types. Therefore, any detailed investigation of the stellar population of these systems requires a simultaneous study of their behaviour at optical and infrared wavelengths.

This thesis is concerned primarily with extending optical studies of galaxies to infrared wavelengths. The detection of infrared radiation came a year before the discovery of ultraviolet radiation and almost a century before radio

waves (1888), X–rays (1895) and gamma–rays (1900) were produced and identified in laboratories. After the construction of big radio telescopes and the launch of X–ray and UV satellites in the late 1970s, however, radio, X–ray and ultraviolet astronomy became far more advanced than infrared astronomy. This is because of three main difficulties which restrained early progress in infrared astronomy. The first is simply that sensitive infrared detectors were not available until the 1960s and 1970s. Secondly, objects at room temperature (300° K), the sky and telescope all emit infrared radiations at wavelengths of 5–50 micrometers. Thirdly, water vapour and carbon dioxide in the air absorb infrared radiation and therefore infrared observing sites must be carefully chosen to be as dry as possible.

Observations at infrared wavelengths are useful for investigating the following questions:

1. Does an object contain dust clouds which are heated, for example, by nearby sources?

2. Is there ionised gas producing free–free emission?

3. Are there cool stars associated with the object which radiate more prominantly at longer wavelengths?

4. How heavily reddened is the object? This question can be addressed because the extinction by normal dust particles is a strong function of wavelength, being less in the infrared than the optical.

This chapter briefly reviews the modern techniques and scientific achievements of infrared astronomy. The applications of infrared astronomy are discussed in the next section. This is followed by a summary of its techniques in section 1.3. A review of the infrared properties of nearby galaxies is presented in section 1.4. The aim of the thesis and its layout are discussed in section 1.5.

1.2 Applications of Infrared Astronomy

The most important application of Galactic infrared astronomy is in the study of star formation regions surrounded by dust. Dust absorbs starlight and emits infrared radiation at wavelengths dictated by the temperature of the grains. A substantial fraction of Galactic infrared emission originates in this way, though occasionally, in well shielded clouds, the grains absorb little starlight and are heated primarily by collisions with ambient molecules. These sources emit at wavelengths as large as 10 μm.

Of particular importance in these studies are observations of two kinds of regions:

1. Clouds in the temperature range $30° < T < 3000°$ K. Such clouds are too cool to produce optical excitation lines, but are sufficiently warm to emit in the infrared. This class of objects comprise gas at the interface between fully ionised and molecular clouds, or shocked neutral regions in which high–lying levels of diatomic molecules can be collisionally excited.

2. Gas sufficiently warm to emit optical lines, but obscured by dust to an extent that makes a determination of optical line intensities unreliable. Infrared radiations can pass through such clouds relatively unattenuated and hence provide information on their local condition. These types of objects include HII regions obscured by dust and planetary nebulae containing dust.

The mechanisms which change the physical parameters amongst the stars and star clusters produce different effects in the infrared than at visible wavelengths. Therefore, the infrared measurements offer a new way to compare these systems. Star clusters are potentially useful for elucidating the stellar population and dynamical and chemical evolution of galaxies. The globular clusters, for example, provide a base for constructing synthesis models of more complex systems such as elliptical galaxies which contain stars with different metallicities (Aaronson et al 1978). They are also useful in tracing the metal–enrichment sequence and early history of our Galaxy (Zinn 1980).

The usefulness of the globular cluster infrared data for studying the stellar content of galaxies was demonstrated by Aaronson et al (1978). They found the broad–band infrared colours and narrow–band indices (CO at 2.4μm and H_2O at 2.μm) to be sensitive to bolometric luminosity and the location in effective temperature of the composite giant branch, which is related to the mean metal abundance. These data also set limits on the relative numbers of giants and dwarfs and on allowable giant branch luminosity functions.

Metallicity differences act directly on galaxy colours by changing the broad–band infrared colours and narrow–band indices of individual stars and indirectly through changes in the stellar luminosity functions. This is because metals are primary electron donors in the outer envelope of the giant stars. Therefore, the metal abundance controls the number of H^+ ions at the surface of a star and hence the envelope opacity. For convective stars, the envelope opacity indicates the stellar radius and hence the temperature of the star at a given luminosity.

Cohen, Frogel and Persson (1978) obtained infrared data for a selected sample of globular clusters. From a comparison of these data with predictions from model atmosphere calculations they find that over a range of $3800° < T_{eff} < 5250°$ K the optical-ir colours are insensitive to metallicity and surface gravity and can therefore be used to derive the effective temperature of stars. The narrow band CO ($2\ \mu m$) index, which is primarily sensitive to luminosity and effective temperature for population I giants, is found to be sensitive to the metal abundance for very metal poor stars. These data were subsequently used to find empirical bolometric magnitudes and hence to construct the theoretical HR diagram ($log\ L/L_{\odot}$ versus $log\ T_{eff}$).

In the infrared region one essentially receives light from the Rayleigh–Jeans part of the spectrum. Therefore, the sensitivity of the surface brightness (and hence magnitude) of a star to temperature variations is reduced by a factor of four compared to that in the optical. This, for example, results in a reduction in the cosmic scatter in the Cepheid period–luminosity relation caused by both temperature effects and the width of the instability strip on the HR diagram (McGonegal et al 1983; see also Longmore et al 1986).

There are further advantages of studying objects at infrared wavelengths. Firstly, the interstellar extinction law shows that the attenuation of starlight in the infrared is reduced by a factor of 10 compared to the optical. This is of fundamental importance in photometric studies of stars and galaxies. Secondly, near–infrared ($\lambda < 2\ \mu m$) radiation from galaxies and composite stellar systems is dominated by cool old stars and, therefore, in the infrared, galaxy colours are more homogeneous along the Hubble sequence and less affected by star formation rate differences. Moreover, by combining the infrared and optical measurements of composite stellar systems we can construct wide colour baselines which are sensitive to giant–to–dwarf ratios in these objects.

1.3 Techniques of Infrared Astronomy

The most serious difficulty associated with ground–based infrared observations is the existence of water vapour in the earth's atmosphere. This is the principal cause of absorption of infrared radiations. Therefore, the appropriate infrared observing site must be at high altitude and have a very dry climate. Throughout the infrared part of the spectrum there are broad and deep molecular absorption bands (e.g. CO and H_2O) of sufficient strength to absorb all the radiation of the appropriate wavelength. Only at wavelengths in the narrow gaps between the molecular bands– the so–called atmospheric windows– can the radiation penetrate to ground level relatively unimpeded. Usually the windows are sufficiently narrow that one may refer to a single discrete wavelength, the effective wavelength. The infrared part of the spectrum is divided into three regions; *near–infrared (*1.1 *μm to* 2.4 *μm), mid–infrared (*3.0 *μm to* 40 *μm) and far–infrared (*40 *μm to* 330 *μm).* The standard infrared wavebands, their symbolic names and the range covered by each filter are given for reference in Table 1.1.

Table 1.1

Waveband *μm*	Effective Wavelength *μm*	Symbolic Letters	Sky Transparency	Sky Brightness
1.1-1.4	1.25	J	high	low at night
1.5-1.8	1.65	H	high	very low
2.0-2.4	2.20	K	high	very low
3.0-4.0	3.50	L 3-3.5	fair	low
		3-4.0	high	
4.6-5.0	4.80	M	low	high
7.5-14.5	10.0	N 8-9.0	fair	very high
		10-12.0	fair	
		rest	low	
17.0-40.0	20.0 17-25	Q	very low	very low
	35.0 28-40	Z		
330.0-370.0	350.0		very low	low

The absorption of radiation by the atmosphere is not the only difficulty facing infrared observations. The sky emits strongly in the infrared with a temperature of about 250° K. Even when the emissivity is low, the energy received from the sky at the detector can be very large compared to the energy of the source under consideration. The sky transparency and its brightness at different infrared wavebands are also indicated in Table 1.1. The problem is most acute in the 10 *μm* band where a 270° K blackbody peaks. Also, at J, H and K (from 1 to 2.2 *μm*) atmospheric thermal radiation and scattering of radiation by small particles cause the sky to be bright and hence contribute to the noise. These problems can be alleviated by choosing a site with suitable atmospheric conditions, employing the appropriate infrared observing techniques (e.g. chopping) and using small beam sizes of only a few arc seconds.

In order to subtract the sky background, astronomers employ a technique

called *chopping*. Two neighbouring patches of sky are presented alternately to the detector and their difference is calculated. There are two main reasons why chopping is used:

1. The response of the detector might vary even when the incident flux does not change.

2. Chopping provides the necessary discrimination against a bright sky and cancels the background noise from the two beams.

As at optical wavelengths, infrared photometry consists of focusing onto a detector the radiation from a star or other object of interest and measuring the energy radiated by it. The most important properties of a detector are its sensitivity, its operating temperature and the time required for it to respond to the incident radiation. The most widely used detectors with the highest sensitivity are: the *lead sulphide (PbS) cell, indium antimonide (InSb) and the doped germanium bolometer.*

Lead sulphide is a photosensitive material which changes its resistance when stimulated by light. The PbS cell is sensitive to radiation from 1 μm to 4 μm wavelength. This detector must be cooled considerably below room temperature. For this purpose liquid nitrogen is used which is cheap and boils at a temperature of 77° $K(-196°\ C)$.

A more sensitive detector for this wavelength range is indium antimonide (InSb). This has an order of magnitude higher sensitivity than PbS cells and also provides a greater improvement at 5 μm over doped germanium detectors (see below). In recent years, the InSb detectors have replaced PbS cells at most infrared observatories. These detectors must be cooled by liquid nitrogen.

Beyond about 4 μm the energy carried by individual photons is too low to produce a change in PbS (and to a lesser extent InSb) and therefore other detectors are needed. A doped germanium detector can be used in this spectral region. In normal metals the electrons move freely and allow the conduction of electricity; in the germanium crystal the electrons are loosely bound and can be freed by only a small amount of external energy. By introducing small impurities, a process called *doping,* the germanium crystal can be made to respond to the desired energy (e.g. infrared radiation). If copper or mercury are the impurities, the germanium crystal becomes conductive under the influence of radiation in the 5 to 15 μm region. Such detectors are more sensitive than PbS and InSb cells and must be cooled far below liquid nitrogen temperatures to about 10° or 20° K. Ge:Cu and Ge:Hg are normally cooled in liquid helium which has a boiling point of 4.2° K and is the coldest known liquid.

A more sensitive detector of this kind is germanium with impurities of gallium (Ge:Ga). This works over a much greater range and for infrared photometry its sensitivity is greater than Ge:Cu and Ge:Hg by an order of magnitude. It must, however, be cooled to less than 2° K. To achieve such a low temperature, liquid helium kept in a low pressure container is used. By lowering the pressure inside the container the boiling temperature of the liquid helium is reduced.

Progress in infrared photometry over the next years largely relies on integrated 2-D detector arrays which have the ability to form images directly. These infrared panoramic detectors will soon be commissioned and work is currently in progress on 32 × 32 charge coupled device (CCD) InSb arrays for the 1 μm to 5 μm spectral region. An analysis of Ge:Cu arrays for wavelengths beyond 30 μm is also underway.

1.4 Extragalactic Infrared Astronomy

In a review article on the infrared emission from extragalactic sources, Rieke and Lebofsky (1979) classify these objects into three broad types.

Their first class of objects consists of normal galaxies in which the near–ir light is dominated by direct radiation from stars, mostly late type giants (Aaronson 1977, 1978; Frogel et al 1978).

In the second class, the infrared emission is produced by thermally re–radiated flux caused by obscuring material (i.e. gas or dust) in an extragalactic object. Starburst galaxies and nuclei of many spiral and irregular galaxies are the likely sources of this type of radiation (Rieke and Lebofsky 1978; Scoville et al 1983).

The third class contains active galactic nuclei, such as Seyfert galaxies and quasars, in which a large fraction of the luminosity is thought to arise from sources other than nuclear processing in stars. The exact nature of the emission mechanism in these objects is not yet clearly understood but energy release from material accreting onto a central massive black hole seems most plausible (Weedman 1977; Rieke 1978).

This thesis is primarily concerned with objects in the first category. The following sections present a review of recent extragalactic work on normal galaxies at near–infrared wavelengths.

1.4.1 Infrared Radiation from Normal Galaxies

I. Ellipticals and Lenticulars

Elliptical and lenticular galaxies (E-SO) are simple systems with little gas or dust. Therefore, one expects the star formation in these objects to have been terminated a long time ago. Studies of E-SO galaxies (Johnson 1966; Frogel et al 1978) have revealed that their light is dominated by late–type stars whose energy distributions peak in the near–infrared. Infrared observations of E-SOs, combined with the luminosity and temperature sensitive spectral indices, can therefore determine the details about the spectral mix of the old populations in these systems and pave the way for a self–consistent scenario for their evolutionary history (Aaronson et al 1978).

A comprehensive study of stellar evolution in early–type galaxies can be carried out by looking at their present stellar mix. For example, comparison of the observational data with stellar synthesis models has confirmed the composite nature of the spectral energy distribution of E-SOs (Tinsley and Gunn 1976; O'Connell 1976). Models with rich giant branches and flat main sequence luminosity functions appear to be consistent with the observations (Frogel et al 1978).

The integrated colours of E-SO galaxies become redder with increasing metallicity because of a combination of a decrease in the temperature of the giant branch, a shift of the horizontal branch from the blue to the red, a redder turn off point for the main sequence and an increase in line blanketing. The infrared colours are therefore useful for tracing metallicity variations because of their insensitivity to the intermediate age horizontal branch and blue main sequence stars. For example, in a comprehensive study of E-SO galaxies, Frogel et al (1978) found that the $J - K$ colours become redder towards the nuclei of these objects implying the presence of metallicity gradients.

A detailed study of the relation between near–ir colours and absolute magnitudes for E-SO galaxies was carried out by Frogel et al. Such relations have been found for shorter wavelengths and are thought to reflect metallicity differences (Faber 1973). The apparent absence of an infrared colour–luminosity relation for E-SO galaxies led Bothun et al (1984) to conclude that the optical and optical–ir colour–luminosity relations for these systems are the result of a change in the number of horizontal branch stars. Clearly, a complete infrared redshift survey will be needed to investigate this question. The optical–ir colour–luminosity plots (Frogel et al 1978; Aaronson et al 1981) show a scatter somewhat more than the observational errors. It is important to understand the origin of this scatter (e.g. whether a second physical parameter is needed). More extensive measurements of distant 'field' samples must be employed to demonstrate how metallicity, population mix, age and environmental effects ('field' or cluster galaxies) affect the colours of E-SOs.

The infrared luminosity–velocity width relation (Tully–Fisher relation) is amongst the most widely used methods for determining extragalactic distances to spiral galaxies (Aaronson, Mould and Huchra 1980; Aaronson et al 1980;

Aaronson et al 1986). However, an independent method is desirable to check distances derived from this relation. Since infrared colours are insensitive to residual amounts of star formation, reddening and population mix, they might therefore be considered as potential distance indicators comparable to the infrared Tully–Fisher relation. However, in a combined optical–ir study of E-SO galaxies in two nearby clusters (Virgo and Coma), Aaronson et al (1981) showed that infrared colour–luminosity relations do not have a universal zero–point and hence discarded their use as reliable distance indicators. More infrared observations of E-SO galaxies in rich clusters and the general 'field' are necessary to study the environmental dependence of infrared colour–luminosity relation and its cosmic scatter.

Stellar synthesis models constructed for early–type galaxies (Bruzual and Kron 1980) suggest that the shape of the near–ir spectral energy distribution is almost constant to look–back times of $Z \sim 1$ and therefore the infrared colours could be useful redshift indicators. It is well known that the optical colours at large redshifts ($Z > 0.5$) are affected by morphology, redshift and evolution. The addition of infrared colours to an optically selected sample could therefore help to separate the effects of redshift from those of evolution and morphology (Ellis and Allen 1983).

Lilly and Longair (1982) carried out an infrared study of radio galaxies spanning a large range in redshift. At moderate redshifts, $Z < 0.40$, the near–ir colours of these galaxies were found to be the same as normal ellipticals and at high redshifts they showed no evidence for strong spectral evolution. The optical–ir colours, on the other hand, showed significant deviations from the theoretical relations at high redshifts which can be explained by the evolution of their stellar population. If so, these colours support models with relatively slowly decaying star formation rates.

Ellis and Allen (1983) investigated the infrared properties of a sample of optically–selected faint galaxies and found some early–type galaxies with large infrared colours ($J - K > 1.3$ mag.). Such red colours had not been previously found in any other survey of normal galaxies (e.g. Aaronson 1977; Frogel et al 1978). If the infrared colours are reliable redshift indicators, these galaxies must lie at reasonably large distances. An equally valid explanation, however, is the existence of a population of very red nearby galaxies. These objects, at moderate redshifts, can be placed at the bright end of the 'field' galaxian luminosity function (by virtue of an infrared colour–luminosity relation) and therefore a 'field' infrared luminosity function is essential for exploring this possibility.

Finally, the infrared observations of elliptical galaxies have been used for constructing the evolutionary correction to the cosmological deceleration parameter, q_0. The most direct determination of q_0 comes from searching for non–linearities in the Hubble diagram (magnitude–redshift diagram) at large redshifts (Sandage 1975). Lilly and Longair (1982) constructed the infrared (2.2 μm) Hubble diagram for their sample of powerful radio galaxies and indicated a value of q_0 in excess of one. This method relies on observations of the light from elliptical galaxies at ages substantially earlier than the current epoch, when galaxies would appear more luminous than at present (Spinrad 1977) and hence require a correction for luminosity evolution (Tinsley 1973). The large value of q_0 found

by Lilly and Longair can therefore only be reconciled with an open Universe ($q_0 < 0.5$) if there is appreciable luminosity evolution due to the changes of stellar population with cosmological epoch. Observations of the CO index and an accurate conversion of this index to the giant–to–dwarf ratio provides another way for estimating this evolutionary correction.

II. Spirals and Irregulars

Spiral galaxies consist of a population of young stars which dominates their optical light and an underlying old population radiating in the near–infrared. Studying the near–ir emission from spirals is important for two main reasons. Firstly, infrared colours are not affected by hot, young stars which vary from galaxy to galaxy and so can be used to study the underlying old population in these objects. Therefore, one can examine whether spirals and E-SOs have similar stellar populations. Secondly, there are intermediate age stellar populations such as asymptotic giant branch stars, carbon stars and red supergiants whose photometric signature would be obvious on infrared colour–colour plots. Infrared observations of composite stellar systems can isolate these intermediate age populations and give us a clue as to the nature of star formation in these objects (e.g. the Magellanic clouds (Persson et al 1983)). Identification of these stars is also of fundamental importance for studying the evolutionary history of galaxies, for distance determination purposes and for distinguishing between thermal and non–thermal radiations from these galaxies.

A simultaneous study of spirals at optical and infrared wavelengths would help to investigate if they are inherently like E-SOs with young stars added. If the two classes of objects are the same with the only difference being their star formation histories, their infrared colour–luminosity relations will be identical whereas the optical–ir relations will differ due to the effect of star formation.

Tully, Mould and Aaronson (1982) showed that the E-SO and spiral galaxies in the Virgo cluster form two different sequences on the optical–ir colour–luminosity diagram. Clearly a 'field' sample with available optical and infrared data, containing both early and late–type galaxies, is needed to study the cause of this difference and to investigate the extent of this result and its possible sensitivity to dynamical effects. These authors also successfully modelled spiral galaxies on the $(B - H) - M_H$ colour–luminosity plane by assuming that the star formation rate decreases monotonically from the epoch of galaxy formation to the present. However, they also required the initial mass function (IMF) to be flatter and the metal abundance to be lower in low luminosity ($M_H > -20$ mag.) spirals.

A study of the infrared colour–luminosity relation for spirals will be useful for constraining the IMF slope and tracing the metallicity variations amongst these galaxies. However, the infrared colours provide little information on the giant–to–dwarf ratios. The optical–ir colours (e.g. $V - K$), on the other hand, are more sensitive to population mix and age (Struck–Marcell and Tinsley 1978) and can therefore be used to constrain the giant–to–dwarf ratio in these galaxies.

Results from a compilation of optical and infrared data for bulges of spirals

reveal that the blue stars from young stellar systems with ages less than 10^8 years make a significant contribution to their optical light (Frogel 1985). The infrared light, however, is dominated by an older and more metal–rich stellar population (of the same type as in E-SOs) with an age of a few Gyrs. Therefore, the E-SO galaxies and bulges of spirals appear to contain similar stellar populations although they may have different dynamical histories (see King and Ellis 1985 for a discussion of this point).

The infrared luminosity–velocity width relation has proved extremely useful for determination of extragalactic distances (Aaronson et al 1980). The use of infrared magnitudes for this purpose is desirable in order to minimise the effect of internal extinction in edge–on galaxies. Moreover, since the infrared light of spirals is dominated by the old population, which is homogeneously distributed throughout the galaxy, the ratio of total mass to infrared luminosity in these systems is nearly constant. Therefore, a tighter relation is expected between mass (HI velocity width) and luminosity at infrared wavelengths compared to that in the optical.

It has been suggested that the slope of the Tully–Fisher relation is wavelength dependent, increasing by a factor of two from the optical to the infrared (Tully et al 1982; de Vaucouleurs et al 1982). This results in a relation between the optical–ir colour and the mass (luminosity) of spirals. Therefore, the optical–ir colours of spiral galaxies can be used to find their intrinsic luminosities. The advantage of this method over the Tully–Fisher relation is that it can be applied directly to face–on galaxies. Furthermore, it provides an independent check on the distances derived from the Tully–Fisher relation.

Bothun et al (1985a) studied the optical–ir colour–luminosity relation for spirals in 8 nearby clusters and found significant differences in their zero–points. This may indeed be expected if spirals have different evolutionary and enrichment histories, depending on their environments. Prior to any investigation of the universality of the spirals' optical–ir colour–luminosity relation, the questions concerning its morphological type dependence and cosmic scatter must be properly answered. A sample of 'field' galaxies, not affected by local velocity inhomogenieties, is urgently needed to tackle these questions.

1.5 The Aim of the Thesis

Discussions in the last section reveal that the infrared samples of nearby galaxies studied so far are either in rich clusters or in fields affected by local velocity perturbations. A more extensive study of the intrinsic properties of galaxies at infrared wavelengths, using a distant 'field' sample, is therefore worthwhile. Such a sample could address the following questions:

1. Is the optical–ir colour–luminosity relation of E-SOs due to a metallicity variation or, as suggested by Bothun et al (1984), is it the result of a change in the number of their horizontal branch stars?

2. Does a metallicity sequence exist for disks of spirals ? If so, is it different from that of the E-SOs?

3. Does the scatter in the spirals' optical–ir colours reduce if a second parameter is introduced?

4. How tightly could one constrain the slope of the stellar initial mass function by using combined optical and infrared data?

Before investigating the universality of the spiral optical–ir colour–luminosity relation, the morphological type dependence of its zero–point must be examined. This can be addressed by employing a large sample of galaxies of all morphological types, drawn from the same environment. A 'field' survey is therefore essential to disentangle these effects.

A redshift survey, complete in infrared wavebands, is crucial for constructing the first infrared luminosity function of 'field' galaxies. It has been found that the apparent value of the cosmological deceleration parameter, q_0, derived from optical Hubble diagrams for radio galaxies (Gunn and Oke 1975) differs from that implied by studies of local galaxy dynamics (Peebles 1979a; Bean et al 1983) and the discrepancy implies a strong luminosity evolution in the 'field' counts (Ellis 1982). At the infrared wavelengths, on the other hand, the stellar evolution is mainly that of post–main sequence stars and is therefore slow. The infrared luminosity function is essential for predicting deep number–magnitude counts at 2.2 μm. Using the number–magnitude counts at this wavelength, one could then constrain the evolution in the optical counts. The time is ripe for such a project with 2–D infrared detectors becoming ready for commissioning. Such an infrared luminosity function also provides the basis for investigating possible differences between the optical and infrared selected surveys.

In this thesis attention is concentrated on the near–ir radiation from normal galaxies. The radiation at this wavelength is known to be dominated by starlight. A sub–sample of the *Anglo-Australian Redshift Survey (hereafter AARS)*, selected in optical wavebands, will be employed to construct a complete infrared survey. In chapter 2 the sample of galaxies, the observations and the data reduction techniques are presented. Chapter 3 investigates the colour–redshift relations and the appropriate corrections for correcting the photometric data to the rest–frame. The corrected data will be used in chapter 4 to study the stellar population

of nearby galaxies. Chapter 5 investigates the application of the infrared and optical–ir colours of E-SO and spiral galaxies to the determination of extragalactic distances. The 'field' infrared luminosity function is presented and analysed in chapter 6. Finally, the conclusions and a summary of the future highlights of this project are discussed in chapter 7.

CHAPTER II

Infrared Observations of the AARS

2.1 Introduction

The compilation of the *Anglo–Australian Redshift Survey (hereafter AARS)* was started in 1979. The primary aim of this project was to investigate the cosmic virial theorem (Bean et al 1983), the spatial correlation function of field galaxies (Shanks et al 1984) and the optical field luminosity function (Efstathiou et al 1987). The survey covers 5 small fields to an average magnitude limit of $B_J = 17$, and is thus expected to be unaffected by local inhomogeneities and be representative of the Universe on scales of 100–200 Mpc.

Similar studies were undertaken at about the same time by two other groups, Kirshner et al (1978, hereafter KOS) and Huchra et al (1983, hereafter CFA). The KOS sample consists of eight separate fields in the north and south galactic hemishperes each having 20–30 galaxies to a magnitude limit of $m_J = 15.50$. The small number of galaxies in each field and the relatively small solid angles they subtend made the statistical analysis of the correlation function uncertain. The CFA survey has redshifts and magnitudes for about 2400 galaxies and is complete to $m_z = 14.50$. This sample, although it provides an invaluable library for nearby galaxies, has two disadvantages. Firstly, it is dominated in the north by the Local Supercluster and hence the luminosity function derived from it is rather sensitive to the assumed Virgocentric flow model. Secondly, it is based on Zwicky's magnitude system which is known to suffer from systematic errors as large as 0.5 mag. The need for a new survey was hence motivated by a desire to avoid these problems.

Details about the AARS and the original analysis of the data are given elsewhere (Bean 1983). In this complementary study I investigate the extension of the survey photometry to infrared wavelengths. The motivation for this extension is twofold. Firstly, I wish to study the infrared and optical–ir Colour–Luminosity relations for field galaxies both as a function of morphology and environment. Secondly, the large redshift sample provides a base for constructing the first infrared galaxy luminosity function which is a necessary prerequisite for understanding a variety of cosmological studies that can be undertaken in the infrared.

In the present chapter the observational techniques and data reduction will be discussed. A brief account of the general features of the AARS will also be presented. The next section gives a background to the survey and its selection

criteria. A summary of the infrared observational techniques and reduction of the photometric data will be given in section 2.3. Redshift measurements will be discussed in section 2.4. Section 2.5 presents the data and the corrections applied to the observed magnitudes. A brief description of general properties of the AARS is given in section 2.6.

2.2 Selection of the AARS

The main constraint in selecting the sample was to fix the total number of galaxies in the survey. With an optimal observing set–up on the Anglo–Australian Telescope (AAT), it was estimated that one could measure the redshift of a typical galaxy to an accuracy of better than 50 Km/sec in 15 to 20 minutes. Thus, measuring redshifts for a minimum sample of 200 galaxies would occupy about ten clear nights, a reasonable demand on the AAT. The following criteria were initially considered for selecting the fields:

1. The limiting magnitude of the survey.

2. The angular size of each field.

3. The number of fields.

Since the project was primarily intended for correlation function studies and there was already evidence from the Zwicky and KOS counts for inhomogeneities to $B = 15.50$ it seemed desirable to go deeper than a limiting magnitude of $B = 16.00$. Catalogues of galaxies could be constructed from UK Schmidt plates, which have an unvignetted region of typically $4° \times 4°$. Down to a magnitude limit of $B_J = 16.50$ (photographic B_J band lying between 4000 and 5500 $A°$) counts reveal around fifty galaxies in this area and hence a reasonable sample of galaxies can be formed using about four fields. Reducing the angular size of the fields, although allowing more fields to be studied, would have reduced the number of pairs contributing to the correlation function and increased photometric preparations. Statistical fluctuations in the redshift distribution would have been significant if the width across a field at its characteristic depth had been smaller than the correlation length ($r = 5$ Mpc.).

In addition to the above criteria the AARS fields were chosen to be well–separated fields at high Galactic latitude in order to avoid extinction in our Galaxy. The resulting survey contains 5 fields (2 northern and 3 southern fields), having a total of 329 galaxies. For the infrared studies in this project only the three fields listed in Table 2.1 are observed. The other two fields had declinations ($\delta = -49°\ 42'; \delta = -45°\ 06'$) which were not accessible from the United Kingdom Infrared Telescope (UKIRT) used for the infrared observations (the lowest declination reached by UKIRT is about $\delta = -46°$). This reduces the number of accessible AARS galaxies to 210.

Table 2.1

Characteristics of the AARS fields

Field	Field Centers α h min	δ deg min	bII deg	isophotal B_J limits	No of galaxies with $m < B_J$	Area $deg.^2$
S1	00 57	–28 02	–90	16.75	74	14.06
N1	13 41	0 00	60	16.75	68	13.95
N2	10 40	0 00	49	16.50	68	13.91

2.3 Photometry

2.3.1 UKIRT and Observational Techniques

a) The Telescope

The 3.80 m United Kingdom Infrared Telescope is the largest telescope in the world designed specifically for infrared observations. Its location on the summit of Mauna Kea, Hawaii, at an altitude of 4200 m (13800 ft) is exceptionally well suited for infrared programmes requiring low water vapour and low thermal sky emission. The primary mirror is made from an unusually thin glass disk, and consequently weighs $\frac{1}{3}$ of that of conventional telescope mirrors. This allows an extremely light–weight supporting structure to be used with consequent saving in cost. The small secondary mirror of the telescope acts as an aperture stop to reduce thermal effects. The effective aperture of the telescope is 3.75 m. The mirrors are supported in a light telescope tube. This open tube is mounted inside a large yoke, so that it can rotate about two bearings for tracking purposes. The small dome size, coupled with this mounting arrangement, restricts the telescope elevation to altitudes greater than 23 degrees above the horizon. A more serious limitation is that the small dome and light–weight structure make the telescope more sensitive to vibration by the wind than most other conventional telescopes. The telescope is completely computerised. A DEC PDP 11/40 computer (upgraded to a VAX in 1984) is dedicated to monitoring and controlling the telescope position and drives.

The basic configuration and instrumentation is shown in Figure 2.1. Below the primary mirror (C) is the instrument rotator flange (D). All common user instrumentation is mounted on the 'gold dustbin' (E) that can be attached to the instrument rotator. A dichroic mirror (F) reflects the infrared radiation through 90 deg. into the side–ways looking cryostats (B). Optical light passes through the dichroic, and a TV camera (H) is mounted on an X–Y crosshead (G) that is attached to the base of the 'gold dustbin'. This TV is normally used to guide the telescope. For this purpose offset guiding can be used. The X–Y crosshead has a range of travel of $\pm$13 arcmin. at $f/9$ and $\pm$4 arcmin. at $f/35$. The TV itself has a field of view of 72 $\times$ 54 arcsec. in both configurations.

The detector used in this study was an *Indium Antimonide (InSb)* photovoltaic device. The detector, the filters and the aperture wheels were cooled to

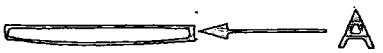
A

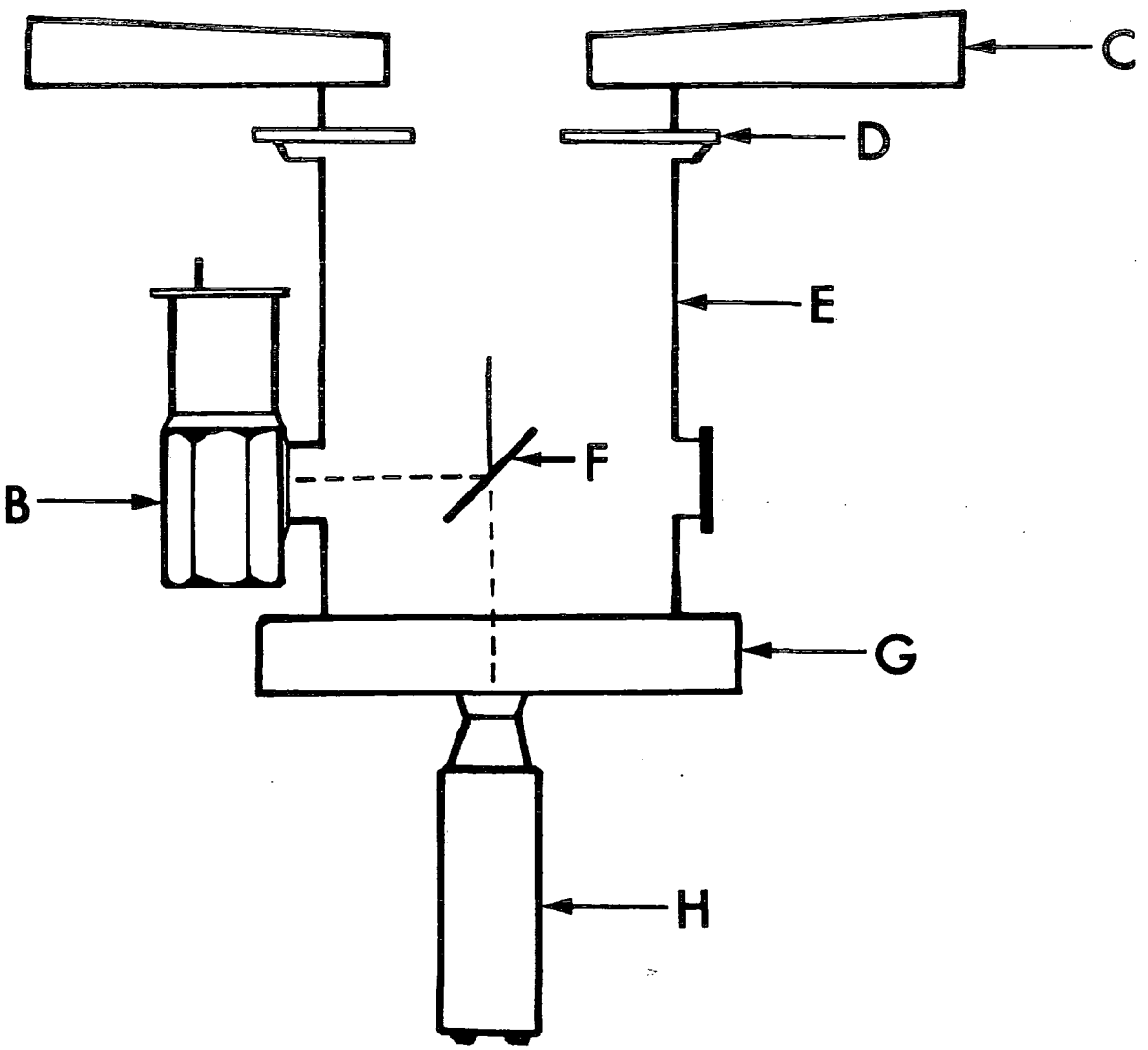
C
D
E
F
B
G
H

55° K using liquid helium. The instrumentation is controlled by another DEC PDP 11/40 computer which is linked both to the instrumentation and to the telescope control computer.

b) Infrared Observing Techniques

At wavelengths longer than 3 μm the level of the infrared background is very high and is completely dominated by thermal emission from the atmosphere and the telescope itself, which are both radiating at 250° – 300° K. These problems are overcome by the techniques called *chopping* and *nodding*. To subtract the background from the object signal, the telescope is first pointed at the source then at a nearby patch of empty sky and the two signals are compared. This is done by moving the secondary mirror back and forth with a frequency of 5–10 Hz. In one position of the mirror the detector sees a portion of the sky and in the other the source and its surrounding patch of sky.

The signal from the detector is first amplified by a preamplifier at the cryostat before being sent to the control room. Here the signal is modulated by a square–wave that is phase–locked to a signal from the chopping device. The square wave modulation has the effect of subtracting the reference area flux from that received from the object area. The modulated signal, measuring the emission from the source only, is displayed on a strip chart pen recorder and sent to the instrument computer. The chop size has a maximum value of about 100 arcsec.

While observing, it is necessary from time to time to exchange star and sky positions by moving the telescope so that the source is now seen by the detector during the opposite half of the chopping cycle of the secondary mirror. This manoeuvre, called 'nodding', is done at intervals of a few tens of seconds and is important for the overall efficiency of observing. This removes any systematic effects caused by astronomical seeing or by the two beams having slightly different ray–paths through the telescope and consequently seeing different areas of the primary mirror. This technique also removes the effects of a uniform gradient in the background.

2.3.2 Infrared Observations and Data Reduction

All the infrared observations presented in this thesis were made during 16 scheduled observing nights on UKIRT in the period April 1982–November 1983. The dates of these runs, the telescope configuration and the number of galaxies observed in each run are listed in Table 2.2. The observations were made in three passbands J ($\lambda = 1.25\ \mu m$, $d\lambda = 0.30\ \mu m$), H ($\lambda = 1.65\ \mu m$, $d\lambda = 0.30\ \mu m$) and K ($\lambda = 2.20\ \mu m$, $d\lambda = 0.40\ \mu m$) using an InSb detector (UKT6).

Table 2.2

Observing record for UKIRT (1982-83)

Date	No of allocated nights	No of clear nights	Telescope configuration	No of observed galaxies
Apr 1982	6	0	f/9	0
Sept 20–26 1982	6	4	f/9	36
Apr 8–14 1983	6	6	f/35	124
Oct30–Nov2 1983	4	2	f/35	55

All the nuclear positions were acquired by offsetting precisely from nearby bright guide stars with known positions. The galaxies were often too faint to be seen on the TV screen and in a few cases where guide stars were not available the peak 2.20 μm flux was used to find the centre of the galaxy after setting the telescope to the rough position of the object. The separation of the signal and reference beams was typically twice the aperture diameter so any contamination of the reference beam by the object is avoided. Because the AARS is a deep sample, corrections for extended galaxian flux in the reference beam (Aaronson, Huchra and Mould 1979) are negligible (< 0.02 mag.). All the infrared measurements were made over 20 arcsec. aperture. A large aperture was chosen to get the magnitudes as close as possible to the total. This simplifies the task of interpreting the results from the luminosity function and number–magnitude counts. Choosing large apertures also provides an increased tolerance to positional errors.

The atmospheric extinction is small in the infrared on a good site such as Mauna Kea. Typical corrections are about 0.05 mag. per air mass for H and K and 0.08 mag. per air mass for J. The corrections for the atmospheric extinction were calculated each night by frequent measurements of the standard stars (Elias et al 1982) close to each field. The agreement between the observed magnitudes of the standard stars measured on different nights, and reduced by using the extinction relation appropriate to that night, was found to be better than $\pm$ 0.04 mag. The colour equations from Frogel et al (1978) were employed to convert the standards' colours to those in the Johnson system.

During the second run in September 1982 the performance of the autoguider was not always satisfactory. This led to positional errors which gave poor repeatability for some of the galaxies observed in that run. Some of those galaxies were observed again in November 1983. The mean difference between the J, H and K magnitudes of galaxies measured in both of these runs is 0.08, 0.08 and 0.07 mag. respectively. The magnitudes of those galaxies only measured on the first run are of poorer quality and will only be used in the luminosity function

analysis where such photometric errors are tolerable. Furthermore, a few galaxies in the S1 field in November 1983 were observed in poor conditions. Only K magnitudes for these galaxies were measured. These are estimated to be accurate to $\pm$ 0.10 mag. and will only be used for luminosity function studies. Excluding these uncertain measurements reduces the total number of galaxies with accurate J, H and K magnitudes from 194 to 154.

In order to get an estimate of the repeatability of the more precise infrared magnitudes, 31 galaxy measurements were repeated on different nights and reduced independently. The root mean-square (r.m.s.) scatter in these measurements is 0.05 (J), 0.04 (H) and 0.05 (K) magnitudes. The r.m.s. scatter in the infrared colours is typically 0.04 mag. These are taken as reasonable estimates of the accuracy of the infrared photometry of the AARS.

2.3.3 Optical Photometry

The optical photometry of the AARS was done photographically by Dr. Bruce Peterson from IIIa-J plates taken by the UK Schmidt Telescope unit. The plates were hypersensitized and exposed for ten minutes through a GG395 filter, defining a photographic B_J band, extending between 4000 and 5500 $A°$. Photographic saturation in the centers of the images of bright galaxies was hence avoided. The magnitudes were measured by scanning an area around each galaxy on a PDS microdensitometer using a 10×10 μm (0.67 arcsec.) scanning aperture. Density measurements were made over an area of 240 by 240 pixels around each programme object. Blocks of 2×2 pixels were co–added to improve signal/noise and the final 120×120 arrays were smoothed with a 3×3 Gaussian with a sigma of 1 pixel. To find the background density for the entire area of the plate, a series of spot measurements were made and the surface density of the night sky was assumed to produce this background density. The calibration of the plate was carried out by using photoelectric standard stars in each field and deriving a relation between density on the plate and the light intensity required to produce that density in a given exposure time. By cross–correlating the local frequency histogram with an appropriate Gaussian a background sky intensity map was constructed. The isophotal image of a galaxy was then taken to be all contiguous pixels above the local sky by a density threshold of dD=0.08, corresponding to a B_J surface brightness of approximately 23.60 mag./arcsec^2.

The calibration of density to relative intensity was done with respect to the average night sky background. The zero–point of the relative intensity scale was set by photographic photometry of photoelectric standard stars on the plate. Independent CCD frames for individual AARS galaxies selected in most fields were also inspected. These confirm the absolute scale to better than 0.10 mag.

To check the random photometric errors, 24 galaxies were measured on three different plates of the same field. Using the same relative calibration curve, the galaxy magnitudes were independently determined. The r.m.s. error of an individual isophotal magnitude on a single plate is only 0.06 mag. For a more elaborate discussion of the optical photometry of the AARS the reader is referred to Peterson et al (1986).

In order to find the optical–ir colours, the optical magnitudes must be mea-

sured over the same aperture as the infrared data. By multiplying the PDS intensity images of each galaxy with the average of the beam profiles through each of the three infrared filters the total intensity inside the infrared aperture was found. Using different beam profiles measured on different nights and through different infrared filters I find B_J aperture magnitudes which agree within $\pm$ 0.05 mag. This error represents systematic effects caused by wavelength dependence and irregularities of the beam profiles.

In order to examine the sensitivity of the infrared magnitudes to positional errors I used the PDS frames of a sample of randomly chosen AARS galaxies to find B_J magnitudes at different positions across the galaxies. It was found that positional errors of 5 arcsec. change the aperture magnitudes on average by less than 0.10 mag.

2.3.4 Corrections to the Photometry

The optical aperture magnitudes derived from the above procedure are all measured using the observed beam profiles. However, due to the effects of astronomical seeing and imperfect optics a small rounding of the edges of the beam profiles occurs. To correct the aperture magnitudes for this effect I multiply the PDS intensity image of each galaxy with a square beam profile (i.e. flat–top beam profile) corresponding to a 20 arcsec. infrared aperture to find the B_J aperture magnitude. The difference between this and the B_J magnitude found over the observed beam profile was calculated for each galaxy. The infrared magnitudes of that galaxy were then corrected by this value (assuming no colour gradient). The mean beam profile corrections were 0.11, 0.08 and 0.07 mag. for the S1, N2 and N1 fields respectively. The final photometry is then equivalent to that observed through a perfect 20 arcsec. aperture.

The three fields are all at high Galactic latitudes ($|b| > 48°$) and no corrections for Galactic absorption have been applied (c.f. Sandage 1973). Corrections for internal absorption (to face–on magnitudes) have been made using the prescription given in Fisher and Tully (1981). Absorption as a function of inclination is estimated from

$$A_i = -m \left(Ln(exp(-sec(i)) + n \right) + 1 \right) \qquad (2.1)$$

where $m = 0.30$ and $n = 0.01$ and the inclination is calculated using Hubble's relation (Hubble 1926)

$$Cos^2(i) = \left[(a/b)^2 - r_0^2 \right] / \left(1 - r_0^2 \right) \qquad (2.2)$$

where a and b are major and minor axis diameters respectively and r_0 is the ratio of minor–to–major axis diameters when the galaxy is viewed face–on, and is taken to be 0.20. The correction is assumed to be zero for E-SO galaxies and independent of morphological types for the spirals. Therefore, one will not introduce morphological type uncertainties into the inclination corrections. This correction is poorly–defined for inclinations greater than about 70°. The precision of this important correction has been checked by applying three different methods defined by the Second Reference Catalogue of Bright Galaxies (de Vaucouleurs,

de Vaucouleurs and Corwin 1976, hereafter RC2), Fisher and Tully (1981) and Bothun et al (1985a). For spirals with $i < 70°$ (64% of the AARS spiral sample) the inclination corrections agree at the ± 0.03 mag. level. No correction for internal absorption will be applied to the infrared magnitudes. The AARS galaxies are distant enough for the K–corrections to be significant. A detailed description of corrections for redshift effects will be given in the next chapter.

2.4 The Redshift Measurements

The spectra of the AARS galaxies were all measured by the original AARS team in eight observing quarters spaced over two years (from 1979 to 1981). A full account of the redshift measurement and a detailed description of the error analysis is given in Bean (1983) and Peterson et al (1986). The redshift measurements were made using the 3.90 m Anglo–Australian Telescope and the Royal Greenwich Observatory spectrograph with a grating offering a reciprocal dispersion of 33 $A°/mm$ at 3700 $A°$. With the Image Photon Counting System (IPCS) each galaxy spectrum was recorded at a resolution of 1 $A°$ from 3700 to 4700 $A°$. In this wavelength range there are many strong absorption features, including the two CaII lines (H and K) needed to obtain high accuracy absorption redshifts. The cross–correlation technique of Tonry and Davis (1979) was used to obtain the final velocities. From tests of possible internal and external errors on the derived radial velocities an error < 45 Km/sec is estimated for the redshifts. The error does not appear to correlate with apparent magnitude, velocity or galaxy type.

2.5 Corrections to the Observed Magnitudes

The observed magnitudes of the AARS galaxies correspond to different metric sizes because of the range in distances involved. For example, a nearby galaxy will not entirely lie inside the aperture and therefore only a fraction of it will contribute to the light we receive. However, the observed aperture magnitude of a compact galaxy could well correspond to its total light. To avoid this problem one must normalise the aperture magnitudes to the size of the galaxy.

Major and minor axis diameters of the galaxies at the 25 B_J mag./arcsec.^{2} isophote were measured using the standard Starlink software *Image Analysis Mode (IAM)* developed at the Royal Observatory Edinburgh (Martin and Lutz 1979). The IAM algorithm is basically a thresholding procedure and only images brighter than a threshold percentage above the sky are detected. The diameter values were compared in one field with independently reduced CCD frames kindly provided by Dr. N.Metcalfe. They were found to agree within ± 4 arcsec.

The diameters are corrected for inclination via the following formula taken from the RC2

$$\log(D_0) = \log D_{25} - 0.235 \log R_{25} \qquad (2.3)$$

where D_{25} and D_0 are the observed and inclination–corrected diameters at 25 mag./arcsec.^{2} respectively and $R_{25} = \frac{a_{25}}{b_{25}}$ is the ratio of the major–to–minor axis diameters at the same isophote.

A further correction to the diameters due to a change in surface brightness (by a factor of $(1+Z)^4$) and K–dimming is needed (c.f. Aaronson et al 1980). To derive the size of this correction I assume Freeman's (1970) surface brightness distribution for an exponential disk. Any correction due to a difference in surface brightness distributions between E-SO and spirals is a second order effect and expected to be small. I also take a mean optical K–correction of $K(B_J) = 2.5 \times Z$. The change in diameters with redshift is then

$$d(\ \log(D)\ ) = 0.90 \times Z \tag{2.4}$$

The mean correction (due to redshift and inclination) to the diameters of the AARS galaxies is found to be 11%. Taking the slope of the optical growth curve used in this study (see below) this corresponds to an average correction of 0.06 to the magnitudes.

I now calculate the ratio of the infrared aperture to the isophotal diameter ($\log(A/D_0)$) for individual galaxies and present the $\log(A/D_0)$ distribution in Figure 2.2. For the observing aperture of A=20 arcsec., used in this study, the $\log(A/D_0)$ distribution is approximately Gaussian and peaks close to a value of 0.00. Therefore, it is reasonable to reduce all the magnitudes to $\log(A/D_0) = 0.00$ as this requires the least extrapolation of the data.

Since the appropriate infrared growth curves are not yet available for these large effective apertures (Aaronson, Huchra and Mould 1979), I use the type–dependent blue growth curves from the RC2 to correct magnitudes to $\log(A/D_0) = 0.00$. To avoid complicating the correction by introducing too detailed a type–dependence I adopt a mean growth curve (corresponding to T=3) from the RC2 (de Vaucouleurs 1977a) for all the spirals and the SO (T=−2) growth curve from the same source for E-SOs. Corrections for mean $V-K$ colour gradients were taken from Aaronson (1977,1978) and combined with $B-V$ colour gradients for E-SOs (Sandage and Visvanathan 1978a) and spirals (Griersmith 1980a). The mean slopes of optical–ir colour–aperture relations as a function of morphological type are

$$\begin{aligned} d(B_J-K)\ /\ d(\log(A/D_0)) &= -0.16 \quad for\ E-SOs \\ d(B_J-K)\ /\ d(\log(A/D_0)) &= -0.36 \quad for\ spirals \end{aligned} \tag{2.5}$$

The infrared colour gradients are small (Aaronson 1977; Frogel et al 1978) and hence explicitly neglected. Because the distribution of effective apertures in this sample is strongly peaked the uncertainties introduced by these corrections to a fixed $\log(A/D_0)$ are expected to be less than 0.20 mag. to the magnitudes and 0.05 mag. to the colours. Considering uncertainties in growth curves and beam profiles I therefore estimate a total error of 0.20 mag. in the standard optical magnitudes and 0.15 mag. in B_J-K colours.

To compare the optical luminosity function found in the present study (Chapter 6) with that from all the five AARS fields (Efstathiou et al 1987) a relation is needed to relate the original isophotal magnitudes with the new standard aperture ones. The B_J magnitudes at $\log(A/D_0) = 0.00$ as derived in this section ($B_J(0.00)$) are plotted against their corresponding isophotal magnitudes

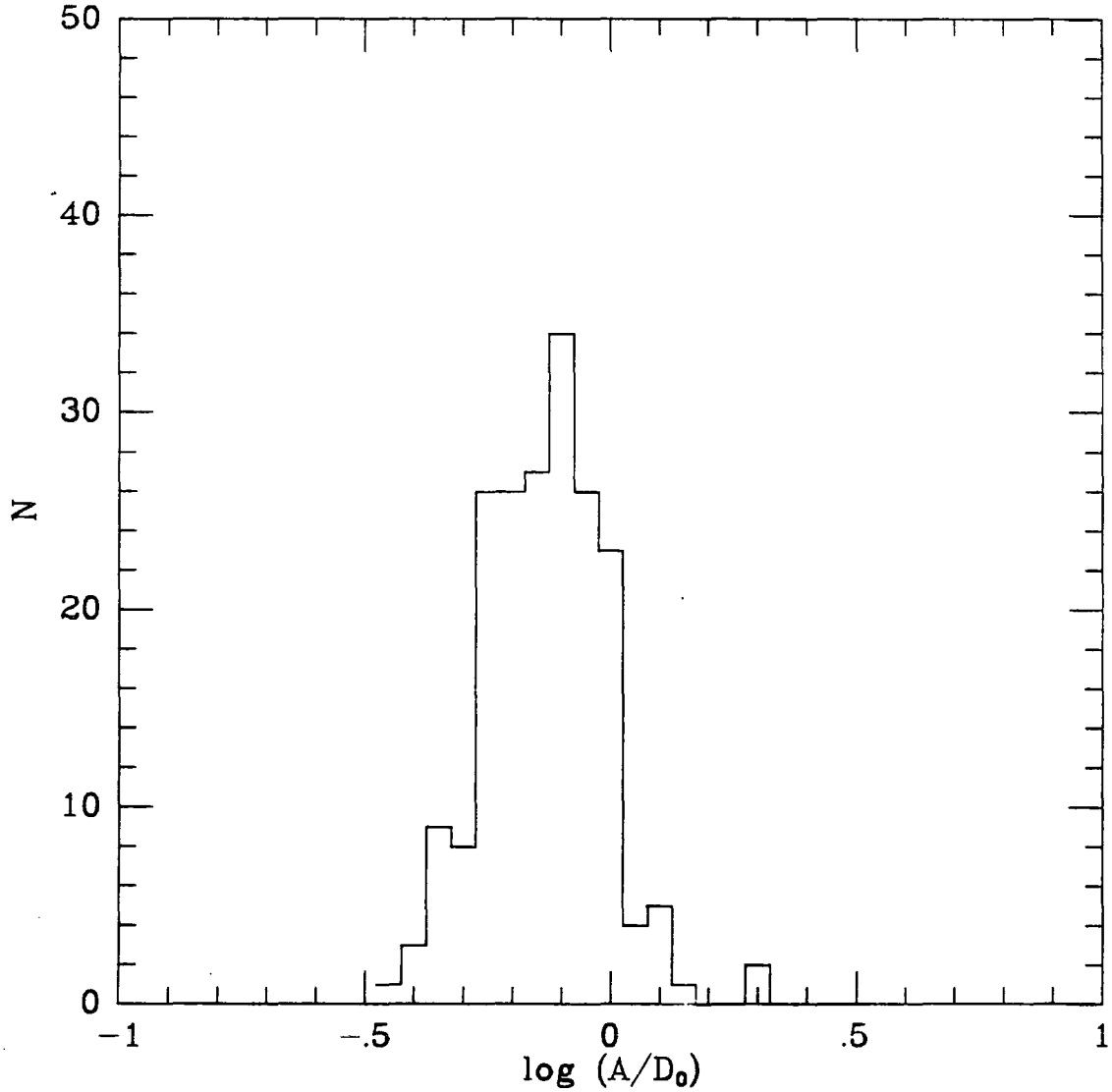

Figure 2.2

$\log(A/D_0)$ distribution for the AARS galaxies.

from Peterson et al (1986)-($B_J(BAP)$). A least squares fit gives

$$B_J(BAP) = (1.20\pm.03)\times B_J\ (0.00) - (3.18\pm.04)\ \ r = .96\ \ r.m.s. = .20\ \ N = 192 \tag{2.6}$$

which can be used to convert B_J magnitudes at $\log(A/D_0) = 0.00$ to the Peterson et al (1986) system.

I now investigate how close the estimated magnitudes at $\log(A/D_0) = 0.00$ are to total magnitudes. Employing the mean blue growth curve from the RC2 I estimate

$$B_J(total) = B_J(0.00) - 0.15 \tag{2.7}$$

which will be useful to convert the present magnitudes to the total.

The infrared catalogue is listed in Table 2.3. There are a total of 194 galaxies with available optical and infrared data. Morphological types were kindly provided by H. Corwin except for one field (N2) which was classified by the members of the Durham Cosmology Group. Table 2.3 contains the raw data and is explained more fully as follows:

Column 1: The name of the galaxy.
Column 2: Heliocentric velocity.
Column 3: Morphological types.
Column 4: log of the major–to–minor axis diameter ratio $\log(a/b)$ at 25 mag./arcsec.^{2} isophote. These diameters are in the RC2 system.
Column 5: $\log(D_0)$ in arcsec. corrected for inclination and redshift.
Columns 6,7,8 and 9: Observed $J-H, H-K, B_J-K$ colours (not corrected for inclination and redshift) and K magnitudes at 20 arcsec. aperture.
Columns 10 and 11: Observed B_J-K colours and K magnitudes at $\log(A/D_0) = 0.00$.

Table 2.3

Observed Photometry of the AARS

					at 20" aperture				$\log(A/D_0) = 0.00$	
Name	Z	Type	log (a/b)	log (D_0)	$J-H$	$H-K$	B_J-K	K	B_J-K	$K(0)$
S1 Field										
GSA002	0.0187	Sc	0.03	1.65	0.70	0.29	4.05	11.15	3.92	10.83
GSA004	0.1075	SO	0.21	1.50	0.75	0.43	4.52	12.80	4.49	12.69
GSA001	0.0187	Sbc	0.01	1.72	0.74	0.30	4.21	10.71	4.06	10.28
GSA003	0.0404	Sbc	0.04	1.46	0.72	0.37	3.32	11.64	3.26	11.55
GSA005	0.0187	Sb	0.59	1.34	0.82	0.37	3.86	11.54	3.85	11.52
GSA007	0.0190	Sbc	0.14	1.51	0.68	0.32	3.40	12.36	3.33	12.22
GSA006	0.0179	Pec	0.30	1.29	0.51	0.25	2.19	13.08	2.19	13.08
GSAN01	0.0690	Sb	0.42	1.14	0.75	0.43	4.23	12.58	4.29	12.60
GSA008	0.0584	SO	0.16	1.39	0.75	0.44	4.28	11.42	4.27	11.38
GSA009	0.0589	Spe	0.37	1.54	0.73	0.35	4.06	11.65	3.97	11.47
GSAN02	0.0324	Sbc	0.18	1.46	0.72	0.29	3.35	12.44	3.29	12.34
GSAN04	0.0341	Sab	0.10	1.66	0.65	0.32	3.21	13.02	3.08	12.70
GSA012	0.0195	SbP	0.34	1.45	0.61	0.27	2.92	13.09	2.87	13.00
GSA015	0.0360	Sb	0.31	1.45	0.57	0.37	3.69	12.50	3.64	12.41
GSA010	0.0578	SO	0.13	1.45	0.75	0.37	4.63	11.52	4.61	11.45
GSA011	0.0756	Sab	0.19	1.38	0.77	0.39	3.71	12.65	3.68	12.61
GSA014	0.0577	SO	0.10	1.42	0.74	0.36	4.25	11.87	4.23	11.82
GSA017	0.0357	Sb	0.12	1.41	0.75	0.24	3.33	12.91	3.29	12.85
GSA013	0.0378	SO	0.15	1.55	0.73	0.25	4.04	12.16	4.00	12.01
GSA020	0.0412	Spe	0.14	1.33	0.69	0.38	3.66	12.45	3.65	12.44
GSA021	0.0588	Sa	0.28	1.42	0.75	0.33	3.75	12.36	3.71	12.30
GSA019	0.0573	Sbc	0.19	1.44	0.74	0.33	3.64	12.79	3.59	12.71
GSA023	0.0521	Pec	0.18	1.43	0.67	0.38	3.56	12.75	3.51	12.67
GSA024	0.0581	Sa	0.28	1.42	0.77	0.34	4.27	12.37	4.23	12.30
GSA022	0.0185	SO	0.36	1.15	0.82	0.18	3.28	13.17	3.30	13.19
GSA025	0.0749	SO	0.11	1.49	0.66	0.40	4.05	12.24	4.02	12.14
GSA032	0.0395	Spe	0.36	1.41	0.61	0.38	2.80	13.50	2.76	13.44
GSA027	0.0497	SO	0.10	1.62	0.55	0.37	3.67	12.74	3.62	12.52
GSA018	0.0753	SO	0.05	1.28	0.79	0.37	4.09	12.34	4.09	12.35
GSA033	0.0576	Sab	0.28	1.38	0.45	0.21	2.55	13.88	2.52	13.84
GSA035	0.0402	Sa	0.12	1.51	0.59	0.29	3.62	12.81	3.55	12.67
GSA026	0.0481	Sa	0.19	1.32	0.69	0.37	3.46	12.96	3.45	12.95
GSA039	0.0578	Sb	0.11	1.34	0.72	0.36	3.61	12.91	3.59	12.89
GSA046	0.0064	Sdm	0.38	1.44	0.34	–0.05	2.12	14.67	2.07	14.59
GSA034	0.0773	E	0.10	1.36	0.75	0.41	4.49	12.12	4.48	12.10
GSA031	0.0402	SO	0.09	1.27	1.16	0.16	3.87	12.60	3.88	12.61
GSA023	0.0427	SO	0.07	1.31	0.72	0.29	3.84	12.55	3.84	12.55
GSA028	0.0580	Sa	0.03	1.34	0.81	0.29	3.92	12.60	3.91	12.58
GSA037	0.0577	Sa	0.23	1.27	0.80	0.42	4.51	12.22	4.52	12.23
GSA038	0.0513	SO	0.16	1.35	0.71	0.34	4.00	12.44	3.99	12.42
GSA043	0.0700	Pec	0.12	1.35	0.60	0.32	2.92	13.52	2.90	13.50
GSA036	0.1072	Spe	0.17	1.47	0.65	0.51	3.16	13.49	3.10	13.38
GSA131	0.0416	Sb	0.02	0.99	0.64	0.38	3.46	13.25	3.57	13.22
GSA030	0.0579	E	0.17	1.38	0.56	0.37	3.26	13.22	3.25	13.19

GSA047	0.0574	Sc	0.09	1.35	0.70	0.36	3.80	13.01	3.78	12.99
GSA052	0.0694	Sc	0.07	1.58	0.70	0.26	3.58	13.09	3.48	12.87
GSA041	0.0341	Sb	0.44	1.19	0.73	0.28	4.11	12.72	4.15	12.74
GSA048	0.1128	E	0.22	1.53	0.73	0.44	4.47	11.98	4.43	11.84
GSA053	0.0412	S	0.11	1.36	0.65	0.28	3.25	13.43	3.23	13.40
GSA040	0.0717	SO	0.05	1.43	0.72	0.32	4.32	12.37	4.30	12.31
GSA056	0.1074	Sb	0.14	1.45			3.86	12.91	3.81	12.82
GSA049	0.0640	Sb	0.12	1.27	0.70	0.35	3.89	12.95	3.90	12.96
GSA051	0.0977	Sb	0.23	1.39	0.69	0.49	3.84	12.91	3.81	12.87
GSA064	0.1003	Sc	0.03	1.46	0.70	0.34	4.46	12.39	4.40	12.29
GSA045	0.0740	SO	0.22	1.36			3.97	12.67	3.96	12.65
GSA062	0.0759	Sa	0.25	1.37			3.79	13.10	3.76	13.06
GSA058	0.0997	SO	0.20	1.50			4.65	12.50	4.62	12.39
GSA069	0.0764	Sbc	0.11	1.32			3.17	13.71	3.16	13.70
GSA050	0.0582	SO	0.18	1.38			4.46	12.52	4.45	12.49
GSA079	0.0188	Sc	0.43	1.45	0.56	0.22	2.91	14.08	2.86	13.99
GSA060	0.0646	SO	0.31	1.32			4.46	12.66	4.46	12.65
GSA061	0.0542	Sa	0.11	1.41			3.70	13.12	3.66	13.06
GSA070	0.0729	Sb	0.22	1.29			2.83	13.92	2.83	13.92
GSA074	0.0378	Sa	0.28	1.31			3.78	12.97	3.78	12.96
GSA078	0.0585	Sc	0.57	1.33			4.52	12.81	4.51	12.80
GSA090	0.0204	Pec	0.17	1.61			2.50	14.58	2.39	14.32
GSA087	0.0533	Sbc	0.26	1.39	0.63	0.31	3.10	13.94	3.07	13.89
GSA084	0.0228	Spe	0.05	1.50			2.51	14.25	2.44	14.11
GSA071	0.0404	SO	0.19	1.29			3.73	13.13	3.73	13.13
GSA091	0.0678	S	0.03	1.39			2.45	14.44	2.42	14.40
N2 Field										
GNB001	0.0187	Scd	0.15	1.60	0.69	0.34	3.89	11.00	3.78	10.75
GNB002	0.0189	E	0.07	1.53	0.71	0.27	4.21	10.55	4.17	10.41
GNB003	0.0161	Sab	0.13	1.51	0.74	0.31	4.02	11.22	3.94	11.07
GNB006	0.0383	Sc	0.08	1.58	0.70	0.35	3.79	11.62	3.69	11.40
GNB005	0.0064	Scd	0.17	1.58	0.62	0.28	3.27	12.48	3.17	12.26
GNB010	0.0277	SO	0.26	1.47	0.74	0.39	3.84	11.38	3.81	11.29
GNB015	0.0199	Sdm	0.38	1.37	0.57	0.31	2.85	12.61	2.83	12.58
GNB004	0.0389	E	0.10	1.55	0.70	0.35	4.43	11.17	4.39	11.02
GNB014	0.0186	Sdm	0.06	1.62	0.54	0.30	2.89	13.30	2.77	13.02
GNB009	0.0392	E	0.10	1.51	0.71	0.36	4.49	11.06	4.46	10.95
GNB013	0.0380	Sbc	0.41	1.47	0.71	0.39	4.44	11.40	4.38	11.29
GNB012	0.0389	E	0.05	1.49	0.71	0.36	4.42	11.12	4.39	11.02
GNB018	0.0393	Scd	0.08	1.64	0.65	0.39	3.98	12.04	3.86	11.73
GNB019	0.0408	Sc	0.09	1.58	0.65	0.39	4.09	11.95	3.99	11.73
GNB008	0.0189	Sab	0.19	1.54	0.71	0.28	3.89	11.73	3.80	11.56
GNB016	0.0377	Sbc	0.21	1.45	0.72	0.39	4.39	11.39	4.33	11.30
GNB024	0.0161	Sab	0.24	1.31	0.63	0.28	3.26	12.58	3.26	12.58
GNB020	0.0389	Scd	0.29	1.46	0.71	0.36	4.18	11.78	4.12	11.68
GNB021	0.0264	Spe	0.21	1.39	0.66	0.34	3.86	12.11	3.83	12.06
GNB017	0.0390	SO	0.02	1.46	0.72	0.34	4.51	11.41	4.48	11.33
GNB022	0.0366	SO	0.19	1.28	0.72	0.34	4.56	11.42	4.56	11.42
GNB023	0.0723	Sdm	0.10	1.53	0.71	0.44	4.52	11.68	4.44	11.52
GNB031	0.0526	Sbc	0.28	1.35	0.77	0.41	4.23	12.00	4.21	11.98
GNB026	0.0268	S	0.20	1.27	0.72	0.36	4.09	12.12	4.10	12.13
GNB050	0.0392	Scd	0.00	1.39	0.67	0.31	4.16	12.34	4.13	12.29
GNB075	0.0167	S	0.18	1.48	0.49	0.27	2.63	13.74	2.56	13.62

GNB029	0.0650	Scd	0.15	1.39	0.69	0.45	4.46	11.83	4.43	11.78
GNB034	0.0395	Sab	0.16	1.37	0.75	0.33	4.03	12.30	4.01	12.27
GNB030	0.0400	E	0.03	1.40	0.68	0.38	4.13	12.10	4.11	12.05
GNB025	0.0386	Sab	0.27	1.36	0.73	0.39	4.48	11.73	4.46	11.70
GNB041	0.0079	Sbc	0.29	1.29	0.74	0.38	3.95	12.44	3.95	12.44
GNB036	0.0382	Sab	0.15	1.32	0.68	0.41	4.11	12.13	4.10	12.12
GNB027	0.0402	Sbc	0.28	1.26	0.72	0.35	4.35	12.00	4.37	12.01
GNB032	0.0371	Scd	0.45	1.30	0.64	0.40	4.29	12.24	4.29	12.24
GNB033	0.0387	Scd	0.52	1.36	0.67	0.39	4.40	11.95	4.38	11.92
GNB028	0.0610		0.18	1.37	0.69	0.40	4.31	11.92	4.28	11.88
GNB040	0.0391	SO	0.04	1.32	0.66	0.38	4.10	12.12	4.10	12.11
GNB035	0.0382	Sbc	0.16	1.47	0.75	0.32	4.35	11.92	4.29	11.82
GNB011	0.0281	Sab	0.32	1.18	0.68	0.33	4.15	12.11	4.19	12.13
GNB038	0.0387	Pec	0.08	1.27	0.66	0.37	3.90	12.35	3.91	12.36
GNB039	0.0269	Sab	0.20	1.33	0.71	0.26	4.18	12.14	4.17	12.13
GNB037	0.0371	SO	0.14	1.24	0.70	0.34	4.23	12.07	4.24	12.08
GNB043	0.0183	Spe	0.51	1.37	0.62	0.33	3.02	13.23	3.00	13.20
GNB062	0.0189	S	0.34	1.34	0.61	0.23	2.94	13.44	2.92	13.42
GNB046	0.0713	Scd	0.50	1.49	0.69	0.42	4.24	12.18	4.17	12.06
GNB044	0.0380	Sa	0.36	1.21	0.83	0.35	4.38	12.16	4.41	12.18
GNB059	0.0366	Sab	0.21	1.30	0.63	0.37	3.40	13.27	3.40	13.27
GNB048	0.0375	Sbc	0.14	1.29	0.78	0.29	4.16	12.42	4.16	12.42
GNB047	0.0659	Sbc	0.13	1.51	0.66	0.35	4.41	12.08	4.34	11.94
GNB051	0.0400	Sc	0.18	1.49	0.69	0.40	4.14	12.57	4.07	12.44
GNB069	0.0724	Sbc	0.19	1.30	0.66	0.54	3.78	12.87	3.78	12.87
GNB052	0.0372	Sab	0.04	1.36	0.73	0.32	4.19	12.44	4.17	12.41
GNB053	0.0595	Sb	0.03	1.43	0.66	0.46	4.08	12.60	4.03	12.53
GNB055	0.0357	Sa	0.00	1.38	0.70	0.33	4.13	12.54	4.10	12.50
GNB057	0.0716	Sab	0.09	1.41	0.75	0.39	4.08	12.65	4.04	12.59
GNB056	0.0387	Sab	0.46	1.40	0.85	0.43	4.05	12.74	4.01	12.69
N1 Field										
GNA002	0.0227	Sa	0.20	1.64	0.74	0.39	4.00	10.68	3.88	10.38
GNA001	0.0229	Sb	0.18	1.58	0.69	0.39	3.62	10.79	3.52	10.56
GNA003	0.0126	Sab	0.24	1.48	0.66	0.25	3.97	11.06	3.91	10.95
GNA004	0.0404	Sbc	0.22	1.39	0.53	0.31	2.93	12.37	2.90	12.32
GNA005	0.0225	Sa	0.29	1.44	0.69	0.30	3.84	11.53	3.79	11.45
GNA006	0.0475	Sbc	0.01	1.46	0.62	0.35	3.10	12.64	3.04	12.54
GNA007	0.0474	Sb	0.21	1.52	0.61	0.37	2.89	13.21	2.81	13.05
GNA008	0.0149	Sb	0.23	1.42	0.65	0.33	3.08	12.92	3.04	12.85
GNA009	0.0480	SO	0.08	1.47	0.67	0.37	4.12	11.64	4.09	11.55
GNA010	0.0596	Sb	0.57	1.53	0.73	0.56	3.73	12.37	3.65	12.20
GNA011	0.0481	SO	0.16	1.43	0.69	0.35	4.29	11.71	4.27	11.65
GNA012	0.0153	Sc	0.05	1.51	0.55	0.25	2.81	13.60	2.74	13.46
GNA013	0.0220	SO	0.27	1.39	0.71	0.27	3.81	12.27	3.80	12.23
GNA014	0.0128	Sb	0.35	1.42	0.60	0.25	2.99	13.43	2.95	13.37
GNA015	0.0397	SO	0.38	1.34	0.76	0.35	4.22	12.06	4.21	12.04
GNA016	0.0726	Sb	0.07	1.62	0.71	0.41	3.51	12.84	3.39	12.56
GNA017	0.0475	Sbc	0.29	1.38	0.82	0.36	4.00	12.54	3.97	12.50
GNA018	0.0225	SO	0.09	1.36	0.67	0.33	3.91	12.54	3.90	12.52
GNA019	0.0572	SO	0.30	1.27	0.71	0.40	4.40	12.05	4.40	12.06
GNA020	0.0222	Sa	0.16	1.25	0.59	0.23	2.87	13.48	2.89	13.50
GNA021	0.0221	SO	0.12	1.33	0.59	0.29	3.01	13.32	3.01	13.31
GNA022	0.0222	Sa	0.29	1.31	0.49	0.30	2.60	13.80	2.60	13.80

GNA023	0.0219	Sa	0.35	1.46	0.63	0.24	3.61	13.18	3.55	13.08
GNA025	0.0714	Sa	0.32	1.54	0.78	0.61	3.28	13.76	3.19	13.58
GNA026	0.0918	Sc	0.12	1.62	0.63	0.45	4.31	12.53	4.20	12.26
GNA027	0.0616	Sc	0.16	1.36	0.65	0.31	3.36	13.44	3.34	13.41
GNA028	0.0775	SO	0.20	1.27	0.70	0.43	3.81	12.83	3.81	12.84
GNA029	0.0260	SO	0.25	1.40	0.62	0.35	3.59	12.95	3.57	12.91
GNA030	0.0897	SO	0.15	1.48	0.72	0.43	4.68	12.00	4.65	11.91
GNA031	0.0127	Sa	0.28	1.35	0.60	0.23	2.77	14.07	2.75	14.05
GNA032	0.0123	Scd	0.62	1.34	0.59	0.17	2.92	14.45	2.91	14.43
GNA033	0.0886	SO	0.15	1.34	0.72	0.40	4.43	12.14	4.42	12.13
GNA034	0.0577	Sb	0.31	1.33	0.71	0.38	3.66	13.12	3.65	13.11
GNA035	0.0601	Spe	0.56	1.54	0.69	0.54	3.93	12.86	3.84	12.68
GNA037	0.0771	Spe	0.36	1.26	0.49	0.26	3.33	13.67	3.35	13.68
GNA038	0.0785	SO	0.13	1.50	0.65	0.37	4.05	12.68	4.02	12.57
GNA039	0.0735	Sb	0.34	1.51	0.66	0.45	3.96	12.68	3.89	12.54
GNA040	0.0919	SO	0.02	1.69	0.79	0.35	4.27	12.60	4.21	12.30
GNA041	0.0479	Sb	0.19	1.29	0.67	0.34	3.53	13.32	3.53	13.32
GNA042	0.0134	Sc	0.39	1.27	0.56	0.26	3.00	14.18	3.01	14.19
GNA043	0.0904	Scd	0.09	1.65	0.64	0.50	3.60	13.31	3.47	12.99
GNA044	0.0887	SO	0.18	1.57	0.70	0.45	4.48	12.25	4.44	12.08
GNA045	0.0605	S	0.29	0.98	0.61	0.50	3.12	13.70	3.24	13.67
GNA046	0.0537	Sa	0.29	1.38	0.69	0.38	3.80	13.08	3.77	13.04
GNA047	0.0714	S	0.28	1.51	0.63	0.39	3.40	13.39	3.32	13.24
GNA048	0.0898	Sbc	0.11	1.47	0.65	0.39	3.72	13.19	3.66	13.08
GNA049	0.0706	SO	0.11	1.44	0.58	0.41	4.12	12.68	4.10	12.61
GNA050	0.0223	S	0.23	1.17	0.56	0.21	2.88	14.06	2.93	14.08
GNA051	0.0842	Sbc	0.34	1.50	0.68	0.42	3.94	13.01	3.87	12.87
GNA052	0.0615	Sbc	0.19	1.39	0.67	0.35	3.40	13.54	3.37	13.49
GNA053	0.0890	SO	0.17	1.51	0.70	0.42	4.53	12.35	4.50	12.23
GNA055	0.0886	SO	0.25	1.42	0.67	0.48	4.05	12.86	4.03	12.81
GNA056	0.0765	SO	0.26	1.40	0.71	0.40	4.53	12.39	4.51	12.35
GNA057	0.0868	SO	0.04	1.30	0.69	0.43	4.26	12.70	4.26	12.70
GNA058	0.0719	Spe	0.09	1.21	0.55	0.52	3.43	13.42	3.46	13.44
GNA059	0.0762	Sc	0.12	1.59	0.65	0.39	3.62	13.23	3.52	12.99
GNA060	0.0734	SO	0.13	1.54	0.70	0.36	4.32	12.55	4.28	12.41
GNA061	0.0525	S	0.19	1.32	0.58	0.42	3.09	13.86	3.08	13.85
GNA062	0.0395	SO	0.34	1.46	0.70	0.28	4.13	12.75	4.10	12.67
GNA063	0.0232	Sbc	0.27	1.26	0.54	0.26	2.73	14.32	2.74	14.33
GNA064	0.0580	Sd	0.27	1.25	0.62	0.36	3.26	13.76	3.28	13.78
GNA065	0.0584	Scd	0.36	1.41	0.68	0.36	4.08	12.94	4.04	12.88
GNA067	0.0755	SO	0.09	1.61	0.66	0.46	4.37	12.56	4.32	12.35
GNA068	0.0877	Scd	0.38	1.37	0.72	0.39	3.76	13.27	3.73	13.24
GNA069	0.0163	Sb	0.01	1.48	0.60	0.16	2.47	14.75	2.41	14.63
GNA070	0.0876	Scd	0.17	1.51	0.73	0.41	4.21	12.92	4.13	12.77
GNA071	0.0715	SO	0.25	1.44	0.68	0.41	4.43	12.63	4.41	12.57
GNA072	0.0000	SO	0.29	1.16	0.73	0.42	4.36	12.57	4.38	12.59
GNA073	0.0788	SO	0.16	1.51	0.71	0.38	4.21	12.69	4.18	12.57

2.6 General Properties of Infrared Subset of the AARS

This section gives a brief presentation of the general properties of the infrared subset of the AARS (referred to simply as AARS in future) before more detailed discussions in the following chapters. The distributions of the morphological types, magnitudes and redshifts of galaxies used in this project will be considered here.

The proportions of morphological types of 194 galaxies in three fields (S1, N1 and N2) are listed in Table 2.4. The fraction of galaxies with different morphological types in all the five fields, which is considered to be a *fair* sample of the Universe, is also given in this table. The agreement between the whole sample (5 fields) and the subsample (3 fields) is fairly good. This implies that the subsample of the AARS which will be used in the future studies in this thesis is a *fair* selection of the whole sample in terms of the morphological types.

Table 2.4

Proportions of different morphological types in the AARS

Type	Percentage of galaxies in S1,N1 and N2	Percentage of galaxies in all the 5 fields
E–S0	28%	30%
Sa–Sab	18%	19%
Sb–Sbc	23%	22%
Sc–Scd	14%	13%
Sd–Sdm	3%	5%
Unclassified and Peculiars	14%	11%

Notes to the table:

Total number of galaxies in S1,N1 and N2 fields 194

Total number of galaxies with classified types 169

Total number of galaxies in 5 fields altogether 329

The distribution of isophotal blue magnitudes which were originally used to select the AARS is given in Figure 2.3. These histograms are useful in investigating the completeness of each field. The redshift distribution for each field is presented in Figure 2.4. The existence of a cluster is clear in the N2 field at a redshift of about 0.04. Moreover, there is a lack of intermediate redshift galaxies in the N1 field. This will complicate the analysis of the 'field' luminosity function in Chapter 6 where a homogeneous and uniformly distributed sample is a desirable need. I postpone more detailed discussion on these points until the next chapters.

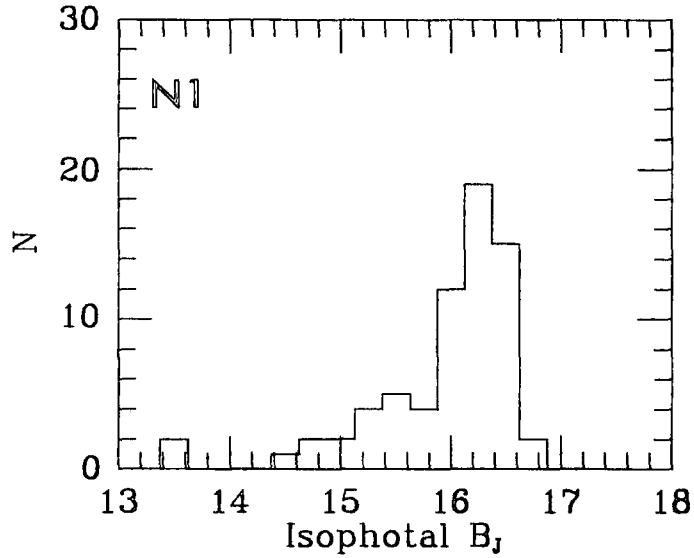

Figure 2.3

Distribution of the isophotal blue magnitudes for different AARS fields.

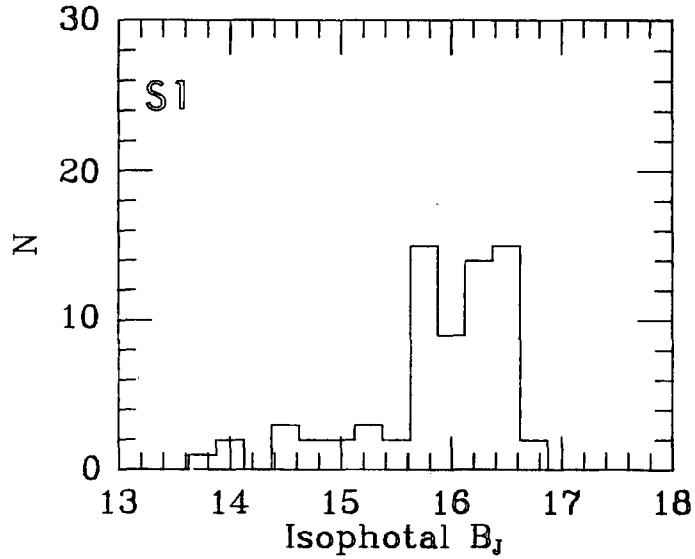

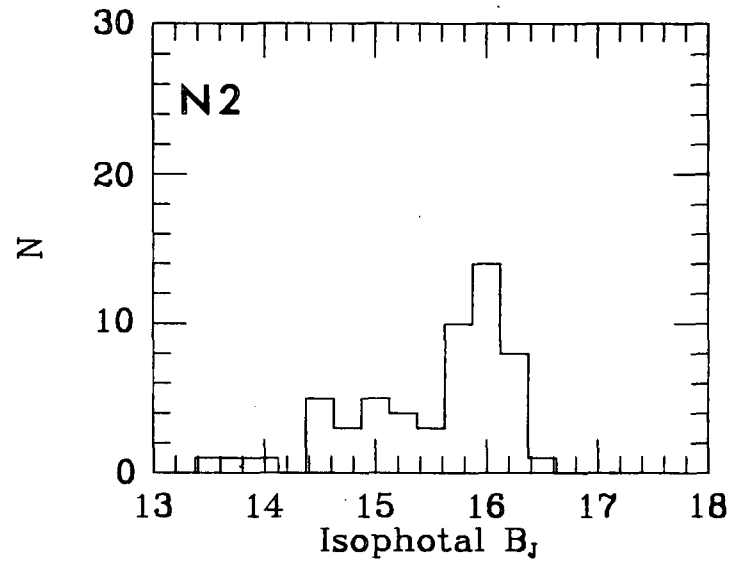

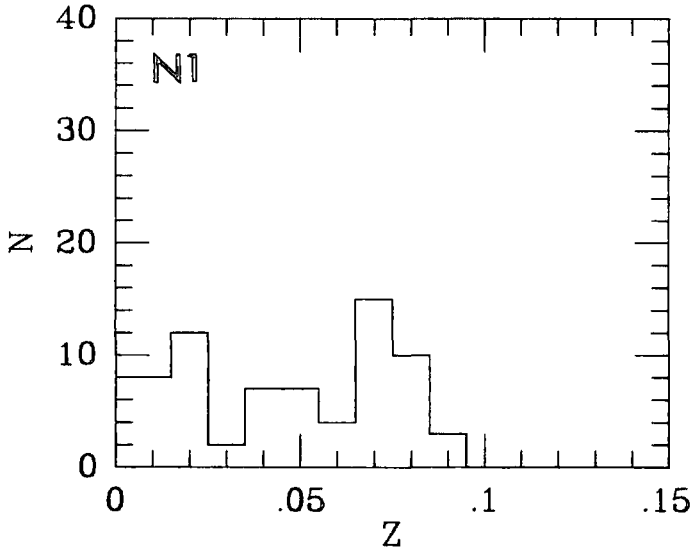

Figure 2.4

Redshift distributions for different AARS fields.

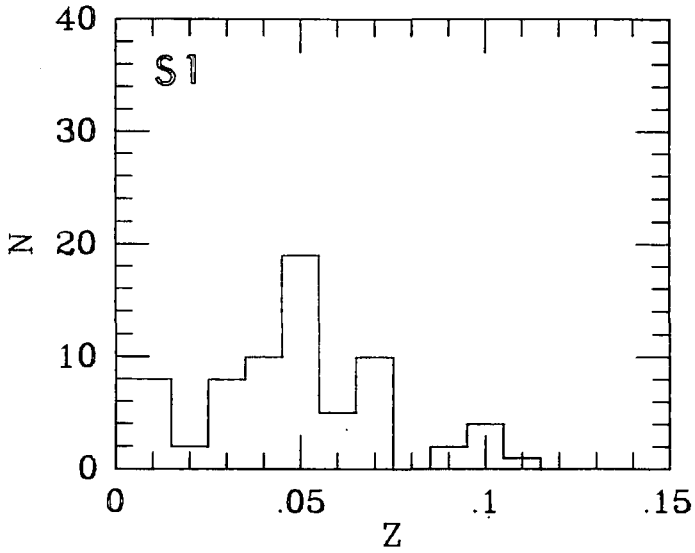

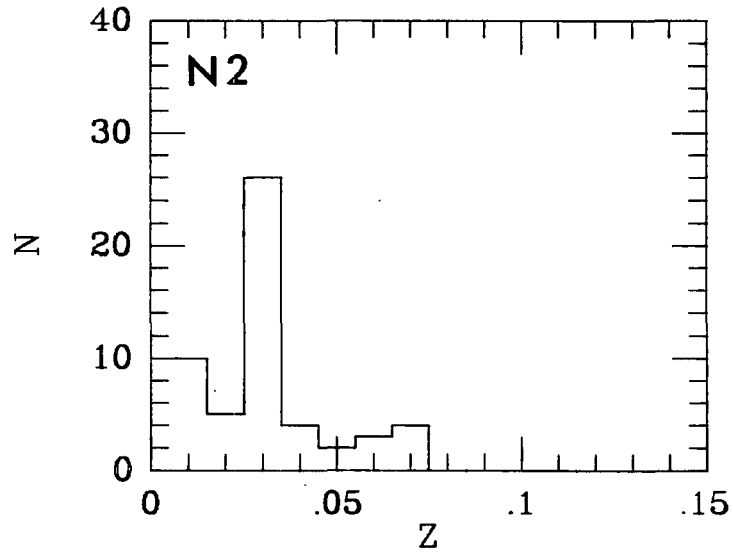

CHAPTER III

Colour–Redshift Relations

3.1 Introduction

The galaxies in the AARS are distant enough for redshift effects to be significant. Therefore, the observed colours and magnitudes presented in chapter 2 must first be reduced to the rest–frame prior to any analysis of the data. This correction is usually termed the K–correction when applied to magnitudes, and differences between the K–corrections for two passbands allows us to correct for the Colour–Redshift (hereafter C–Z) effect. A knowledge of K–corrections and C–Z relations will also be useful for other purposes in extragalactic astronomy.

The K–correction is defined as the change in magnitude with redshift due to the difference in flux at the rest–frame and observed wavelengths. For a galaxy with spectral energy distribution $F(\lambda)$ the observed magnitude at Z=0 is

$$m_\lambda\ (Z=0) = -2.5\ log \int F(\lambda)\ S(\lambda)\ d\lambda + C \tag{3.1}$$

where $S(\lambda)$ is the passband response. Therefore, at a given redshift Z the K–correction is

$$K(Z) = -2.5 \log\Big(\int F(\lambda)\ S(\lambda)\ d\lambda / \int F(\lambda/(1+Z))\ S(\lambda)\, d\lambda\Big) + 2.5 \log(1+Z) \tag{3.2}$$

The second term in equation 3.2 corresponds to the change with redshift in the effective band–width of the detector.

The conventional method for finding the K(Z) polynomial is via spectral energy distributions (SEDs). In order to apply this method properly, one needs reliable SEDs with a reasonably good resolution. Unfortunately, detailed infrared spectra of galaxies between $0.8 - 2\ \mu m$ are not yet available and hence finding the infrared K–corrections from this method is subject to some difficulty. It is possible, however, to exploit various techniques to construct the appropriate infrared SED. For example, the SED of a galaxy can be represented as a linear combination of the SEDs of many stellar types (Turnrose 1976; O'Connell 1980). This method, however, is sensitive to the relative contribution to the model from these various types and consequently a detailed knowledge of the stellar content of galaxies is needed to employ this technique accurately.

The alternative method used here for deriving redshift corrections is an empirical one based on the observed C–Z relation. The observed colour of a galaxy depends upon its redshift, morphology and luminosity. In order to disentangle these effects, I introduce the following procedure. First I confine the sample to the E-SO galaxies for which a preliminary Colour–Luminosity (hereafter C–L) relation is available from published results. Using this adopted C–L relation I reduce every AARS catalogue E-SO colour to that appropriate for a fixed absolute K luminosity. I then determine the variation in the colours as a function of redshift and hence the K–corrections. The analysis can then be extended to other morphological types following the expectation that the infrared K–corrections are type–independent (Aaronson 1977). Although this procedure starts with an assumed C-L relation, several intermediate checks confirm that it is consistent.

A preliminary C–L relation is derived from a compiled sample of published E-SO galaxies in section 3.2. These objects are close enough to be unaffected by even gross uncertainties in infrared K–corrections. In section 3.3 the infrared observations of a sample of nearby cD galaxies are presented. They are measured over the same redshift range as the AARS and provide an independent test for the K–corrections derived in this chapter. The C–L relations from the published data are used in section 3.4 to correct the colours of AARS E-SO galaxies to the same absolute magnitude and find the true variation of colour with redshift. Optical K–corrections are discussed in section 3.5, and in section 3.6 the morphological type–dependence of the infrared K–corrections is examined. Using the K–corrections derived in this chapter, I then calculate the rest–frame colours and magnitudes of the AARS galaxies in section 3.7. The main conclusions are summarised in section 3.8.

3.2 A Preliminary Colour–Luminosity Relation

A sample of nearby E-SO galaxies with published optical and infrared data will be employed here to establish the local C–L relations. The aim is to find a rough estimate of the infrared and optical–ir C–L trend for E-SO galaxies in order to correct the more distant AARS galaxy colours to the same absolute magnitude and derive the C–Z relation.

A comprehensive infrared survey of E-SO galaxies has been done by Frogel et al (1978) and Persson et al (1979). These data are compiled and reduced as follows. The sample of 'field' galaxies (28 galaxies) from Frogel et al is combined with the E-SO galaxies in Virgo (29 galaxies), Coma (20 galaxies) and an extra sample of 'field' galaxies (48 galaxies) from Persson et al. I will refer to this sample as the 'literature E-SO sample'. All the infrared colours are taken from the tables of these papers and are measured over $\log(A/D_0) = -0.6$ (in the system of the RC2 diameters). The colours were then converted to the system of Johnson (1966) using the relation given in Frogel et al (1978).

To form the $B_J - K$ colours for the Persson et al galaxies the data in Table 6 of their paper were used to get $B - K$ colours. These colours were then converted to $B_J - K$ via the following relation provided by Dr. N. Metcalfe (private communication)

$$B_J - K = (B - K) - 0.12 (B - V) \qquad (3.3)$$

For the Virgo, Coma and the 'field' galaxies of Frogel et al, the $B-V$ colours were not available. Here $b-V$ colours, corrected for redshift and absorption, were taken from Sandage and Visvanathan (1978b) and, together with the relation $(B-V) = 1.25(b-V) + 0.22$, were used to get $B-V$. The $B-V$ colours were then combined with $V-K$ to find $B-K$ and finally B_J-K via equation 3.3.

The E-SO optical growth curve from the RC2 was employed to reduce the magnitudes of the literature galaxies to $\log(A/D_0) = 0.00$. These magnitudes were then corrected for optical–ir colour gradient following the prescription given in chapter 2. The published infrared and optical–ir colours are measured at $\log(A/D_0) = -0.6$. A correction of 0.10 mag. is applied to B_J-K to allow for colour gradients. No correction has been applied to the infrared colours.

The published E-SO sample, their infrared and optical–ir colours and M_K magnitudes at $\log(A/D_0) = 0.00$ are listed in Table 3.1 and their C–L diagrams are presented in Figure 3.1. A value for Hubble's constant of $H_0 = 50$ Km/sec/Mpc will be used throughout this thesis. A trend is clear in all C–L relations with brighter galaxies being intrinsically redder. I remind the reader that there are galaxies from the 'field', small groups and rich clusters in these diagrams and hence an assumption concerning the universality of the C–L relations is necessary to use any relation derived from this figure. However, only the slope of the C–L relations is required in order to derive an appropriate C–L correction for E-SO galaxies to correct colours to a fixed absolute magnitude. A detailed discussion of the universality of C–L relations will be presented in chapter 5.

Table 3.1

Fully corrected colours and magnitudes (reduced to $\log(A/D_0) = 0.00$) of E-SO galaxies compiled from literature. A value of $H_0 = 50$ Km/sec/Mpc is assumed.

GALAXY	$J-H$	$H-K$	B_J-K	M_K
FROGEL ET AL				
N205	0.61	0.15	2.57	-16.80
N221	0.72	0.21	3.80	-19.22
N404	0.71	0.13	3.21	-16.28
N584	0.74	0.20	3.93	-25.59
N596	0.70	0.16	3.81	-24.89
N1023	0.72	0.22	3.82	-24.40
N1600	0.80	0.20	4.00	-26.60
N2300	0.80	0.19	4.21	-25.57
N2549	0.63	0.17	3.93	-24.03
N2672	0.75	0.21	3.98	-25.89
N2768	0.76	0.17	3.98	-25.43
N3158	0.79	0.22	4.18	-26.90
N3193	0.73	0.18	3.91	-23.99
N3607	0.75	0.21	4.06	-24.53
N3608	0.76	0.20	3.95	-23.50
N3613	0.72	0.17	3.84	-24.94
N3998	0.76	0.23	4.21	-25.00
N4278	0.72	0.20	4.01	-24.29
N4283	0.73	0.23	3.93	-22.41
N4464	0.76	0.16	3.75	-22.44
N4494	0.73	0.18	3.73	-24.14
N4649	0.79	0.19	4.08	-25.90
N5813	0.77	0.20	4.11	-25.05
N5846	0.80	0.23	4.21	-25.59
N5866	0.76	0.28	4.13	-24.60
N5982	0.71	0.20	3.82	-25.59
N6702	0.79	0.24	4.05	-25.70
N7626	0.77	0.20	4.11	-26.00
PERSSON ET AL				
N1316	0.79	0.22	4.02	-26.50
N1332	0.81	0.24	4.22	-25.40
N1344	0.71	0.24	3.87	-24.30
N1379	0.69	0.18	3.79	-23.70
N1380	0.68	0.23	4.03	-25.20
N1387	0.72	0.24	4.35	-24.50
N1395	0.72	0.20	4.10	-25.30
N1399	0.71	0.23	4.18	-25.40
N1400	0.73	0.20	4.35	-21.50
N1404	0.73	0.18	4.01	-25.00
N1407	0.71	0.24	4.31	-25.20

N1527	0.71	0.20	3.94	−23.50
N1543	0.74	0.25	3.98	−24.30
N1549	0.72	0.20	3.88	−24.50
N1553	0.71	0.21	4.03	−25.10
N1574	0.70	0.21	4.03	−24.10
N1596	0.64	0.19	3.86	−24.10
N1700	0.70	0.20	3.90	−26.30
N2434	0.77	0.25	4.45	−23.70
N2784	0.77	0.25	4.43	−23.70
N2974	0.75	0.17	4.07	−25.00
N2986	0.65	0.23	4.03	−25.30
N3078	0.72	0.13	4.11	−25.10
N3115	0.72	0.21	4.05	−24.10
N3136	0.70	0.22	3.90	−24.50
N3250	0.71	0.24	4.05	−25.80
N3309	0.76	0.23	4.04	−25.60
N3557	0.75	0.22	4.10	−26.50
N3585	0.74	0.19	4.03	−24.90
N3640	0.69	0.15	3.91	−24.30
N3904	0.73	0.20	3.96	−24.60
N3923	0.73	0.22	4.16	−25.50
N3962	0.72	0.21	4.05	−24.80
N4697	0.74	0.22	3.96	−25.70
N4760	0.72	0.19	4.07	−25.90
N4958	0.65	0.25	3.95	−24.70
N4976	0.70	0.19	3.87	−24.90
N5018	0.72	0.23	3.96	−25.90
N5061	0.71	0.20	3.90	−25.30
N5102	0.71	0.13	3.09	−22.00
N6868	0.71	0.19	4.13	−26.10
N6958	0.68	0.20	3.90	−25.30
N7029	0.64	0.15	3.76	−24.80
N3377	0.75	0.17	3.75	−23.40
N3379	0.74	0.19	4.07	−24.60
N3384	0.70	0.18	3.93	−24.00
N4742	0.68	0.24	3.59	−23.50
N5363	0.72	0.22	4.18	−24.80

VIRGO CLUSTER (FROM PERSSON ET AL)

N4124	0.69	0.17	3.58	−23.10
N4179	0.72	0.23	4.04	−24.00
N4264	0.69	0.19	3.66	−21.50
N4270	0.72	0.21	3.73	−22.50
N4365	0.74	0.24	3.95	−25.10
N4371	0.74	0.20	3.87	−23.90
N4374	0.74	0.23	4.06	−25.40
N4377	0.68	0.20	3.75	−23.00
N4382	0.70	0.21	3.64	−25.30
N4387	0.65	0.21	3.73	−22.50

N4406	0.71	0.22	3.98	−25.40
N4435	0.80	0.28	4.24	−24.30
N4442	0.72	0.22	3.65	−24.70
N4458	0.61	0.16	3.73	−22.30
N4459	0.75	0.24	4.14	−24.50
N4468	0.68	0.23	3.67	−21.40
N4472	0.75	0.21	4.01	−26.20
N4473	0.73	0.17	3.91	−24.70
N4476	0.65	0.23	3.67	−22.20
N4478	0.69	0.21	3.91	−23.50
N4479	0.71	0.11	3.66	−21.80
N4486	0.79	0.22	4.12	−25.90
N4550	0.71	0.22	3.72	−23.30
N4552	0.74	0.25	4.12	−25.00
N4578	0.70	0.16	3.75	−23.30
N4621	0.75	0.23	4.04	−25.00
N4636	0.75	0.23	4.07	−25.00
N4660	0.69	0.22	3.85	−23.90
N4754	0.68	0.22	3.96	−24.50

COMA CLUSTER (FROM PERSSON ET AL)

N4874	0.76	0.23	3.88	−26.21
N4881	0.76	0.19	3.90	−24.90
N4883	0.75	0.19	3.87	−24.17
N4886	0.76	0.17	3.68	−24.08
N4889	0.81	0.22	3.98	−26.95
N4923	0.72	0.19	3.87	−24.55
I3998	0.72	0.20	3.93	−23.60
I4011	0.71	0.22	3.69	−23.24
I4012	0.79	0.21	3.98	−23.82
I4026	0.81	0.19	3.82	−23.73
I4042	0.81	0.21	3.91	−24.29
N4906	0.73	0.19	3.97	−24.17
N4921	0.72	0.23	4.05	−25.92
I4021	0.77	0.16	4.00	−23.62
RB37	0.72	0.42	3.54	−21.26
RB38	0.71	0.17	3.53	−22.36
RB40		0.19	3.58	−22.21
RB42	0.70	0.11	3.58	−22.31
RB45	0.74	0.24	3.96	−23.27
RB46	0.73	0.22	3.68	−22.63
RB74	0.72	0.14	3.50	−22.30
RB85		0.09	3.71	−20.96

Figure 3.1

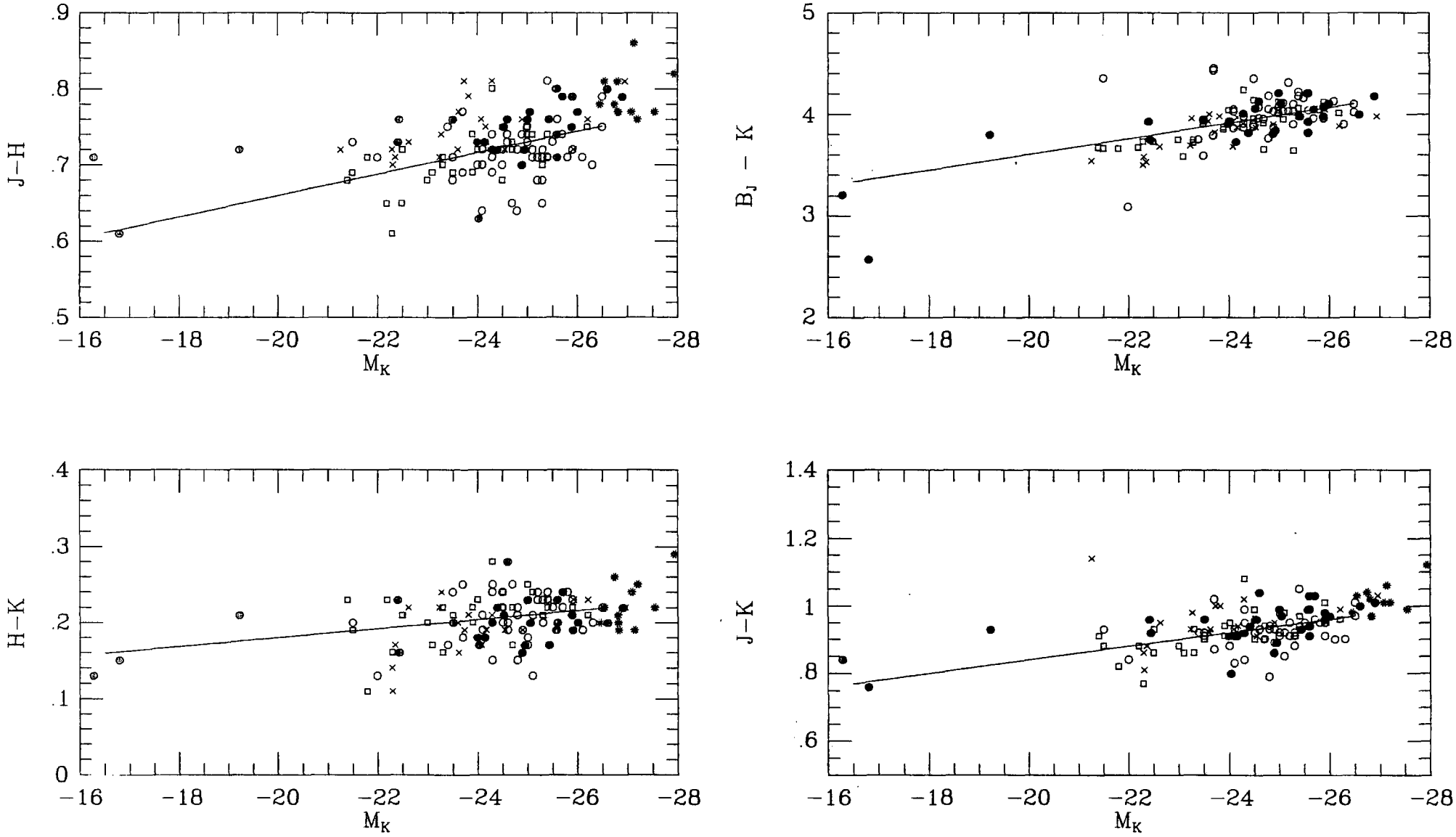

The linear least–squares fits to the C–L relations are listed in Table 3.2 and drawn in Figure 3.1. Three very faint galaxies ($M_K > -20$ mag.) have been excluded from the C–L diagrams and the least–squares solutions. These relations will be used to correct the E-SO colours of the deeper AARS sample to a fixed luminosity.

Table 3.2
Preliminary Colour–Luminosity relations for E-SO galaxies.

$$C = B + A\,(M_K + 25)$$

C	$-A$	B	r.m.s.
$J-K$	0.020 ±.004	0.94 ±.005	0.05
$H-K$	0.006 ±.002	0.21 ±.003	0.03
$J-H$	0.014 ±.003	0.73 ±.004	0.04
B_J-K	0.077 ±.014	3.99 ±.02	0.17

3.3 Infrared Observations of Nearby cD Galaxies

Here I present the infrared (JHK) magnitudes of a sample of 11 nearby cD galaxies kindly made available by Drs D. Carter and A. J. Longmore. These galaxies span the same redshift range as the AARS and will be used as independent checks on the infrared K–corrections derived in this chapter from normal E-SOs.

The infrared magnitudes were measured over a 12 arcsec. aperture. In order to be comparable with the AARS data they must be reduced to an effective aperture of $\log(A/D_0) = 0.00$. However, only three of these galaxies have isophotal diameters available from the RC2. The following steps are hence taken to find diameters for the remainder.

1. I select those E-SO galaxies in the Coma cluster with linear diameters tabulated in the RC2 (Table 3.3). Two of the biggest diameters in Coma are found to be .111 and .113 Mpc.

2. Next I consider the three Carter–Longmore cDs with known angular diameters from the RC2. Using their redshifts I calculate their linear diameters as listed in Table 3.4. The linear diameters of these cDs are in good agreement with the two biggest galaxies in the Coma cluster.

3. The mean of the metric diameters of the cDs (Table 3.4) and the two biggest galaxies in the Coma cluster is found to be .111 ± .007 Mpc. This is assumed to be the linear size of the rest of the cDs.

4. Having the redshifts (and consequently distances) of the cDs and assuming a mean metric diameter of .111 Mpc., their angular diameters are estimated.

Taking the infrared aperture of 12 arcsec. and the angular diameters, the $\log(A/D_0)$ values for each individual cD galaxy is found. The appropriate optical growth curve from the RC2 is then used to reduce their infrared magnitudes to $\log(A/D_0) = 0.00$. The infrared magnitudes were then corrected for optical–ir colour gradients by exploiting the relation given in chapter 2. The sample of cD galaxies is listed in Table 3.5. Columns 1, 2, 3 and 4 give their names, redshifts, distances and angular diameters (in arcmin.) respectively. The $\log(A/D_0)$ values are listed in column 5. The infrared J, H and K magnitudes all reduced to $\log(A/D_0) = 0.00$ are presented in columns 6, 7 and 8 respectively.

Table 3.3

Angular and linear diameters of E-SO galaxies in Coma.

Name	$logD_0$ (arcmin.)	D_0 (arcmin.)	d (Mpc.)
N4874	0.46	2.88	.111
N4881	0.05	1.12	.043
N4886	−0.05	0.89	.034
N4889	0.47	2.95	.113
N4923	0.12	1.32	.051
I4021	−0.50	0.32	.012

Note:

1. D_0 values are taken directly from the RC2.
2. A redshift of $Z = 0.022$ is taken for the Coma cluster corresponding to a distance of 132 Mpc.
3. The mean of the two biggest diameters in the Coma is $.112 \pm .001$ Mpc.

Table 3.4

cD galaxies with available diameters from the RC2.

Name	Z	Distance (Mpc.)	$logD_0$ (arcmin.)	Diameter (Mpc.)	Other name
A2654	.0315	189	.31	.112	N7720
A2666	.0273	164	.25	.085	N7768
N507	.017	102	.67	.139	

Table 3.5

List of the nearby cD galaxies.

Name	Z	D (Mpc.)	D_0 (arcmin.)	$log(A/D_0)$	J(0.00)	H(0.00)	K(0.00)
A2654	.0315	189	2.04	−1.01	10.36	9.53	9.23
A2666	.0273	164	1.78	−0.95	10.34	9.56	9.25
A2670	.0774	464	0.82	−0.61	12.37	11.64	11.21
A85	.0556	333	1.15	−0.76	12.19	11.42	11.04
A157	.0526	315	1.21	−0.78	11.72	10.99	10.64
N507	.0170	102	4.68	−1.37	8.52	7.77	7.49
N1129	.0180	108	3.53	−1.25	9.50	8.74	8.41
A401	.0752	151	2.53	−1.10	11.56	10.78	10.30
A496	.0326	196	1.95	−0.99	11.04	10.29	9.98
A779	.0201	120	3.18	−1.20	9.25	8.51	8.19
A957	.0437	262	1.46	−0.86	11.32	10.59	10.25

Note: cDs in Abell clusters are referred to by the Abell number of the cluster.

3.4 Colour–Redshift Relations for the E-SO Galaxies

We are now in a position to use the E-SO C–Z diagrams (corrected to a fixed absolute K luminosity) to derive an empirical estimate for the infrared K–corrections. In the case of spirals, variations in their star formation rates produce a large scatter in their $(B_J - K) - Z$ diagram and therefore any observed relation between their $B_J - K$ colour and redshift is uncertain and not appropriate for this purpose. Moreover, due to scarcity of published infrared data for spiral galaxies, the significance of a C–L trend for these types is not yet clear. This further complicates the task of correcting the C–Z relation of spirals for a C–L effect.

There are a total of 40 E-SO galaxies in the AARS with reliable infrared magnitudes plus 11 cD galaxies presented in section 3.3. The advantage of using the cDs is that they cover the same redshift range as the AARS sample and therefore provide an independent check on its C–Z trend. All the infrared and optical–ir colours of the AARS and cD galaxies are corrected to those appropriate for $M_K = -25.00$ mag., using the C–L relations found in section 3.2. This value is chosen because it is in the middle of the absolute magnitude range covered by the E-SO galaxies.

The infrared and optical–ir colours of the AARS and cD galaxies are plotted against redshift in Figure 3.2. The trend between the colours and redshifts in these diagrams should be entirely due to the K-term. It might be argued that the cDs and normal E-SOs are from different families but Figure 3.2 seems to suggest otherwise. In any case differences between these two types will not be crucial to the final results. Since there is no E-SO galaxy with $Z < 0.01$ in the AARS sample, I take the zero–points of the C–L relations from Table 3.2 as the zero–redshift colours in the C–Z diagrams. These represent the mean redshift–corrected colours at $M_K = -25.00$ mag. derived from the literature E-SO galaxies. Second order polynomials are then fitted to the C–Z relations, a weight of 4 being given to the zero–redshift colours.

The regressions about the 40 AARS E-SO galaxies are listed in Table 3.6 and plotted on Figure 3.2. The mean observed colours of the E-SO galaxies in the Coma cluster, corrected to $M_K = -25.00$ mag., are also shown on this diagram ($J-K = 1.04 \pm .01, H-K = 0.27 \pm .01$ and $B_J - K = 4.02 \pm .04$). The infrared colours of the Coma cluster E-SOs are in reasonably good agreement with their respective C–Z polynomials but the $B_J - K$ colour is 2 σ deviant from the AARS optical–ir C–Z relation.

The existence of a cluster at a redshift of 0.04 in the 'N2' field was discussed in chapter 2. A scatter in the colours of E-SOs in this cluster would make it difficult to determine the best C–Z polynomial. This effect is not significant on the infrared C–Z diagrams. However, because the scatter in the $B_J - K$ colours (at a fixed absolute magnitude) amongst the galaxies is larger than that in the infrared the effect is worth considering. For example, in this cluster the $B_J - K$ colours of 8 E-SO galaxies (corrected to a fixed absolute magnitude) cover a range of about 0.40 mag. I therefore replace all the 'N2' cluster galaxies on the $(B_J - K) - Z$ diagram (Figure 3.2) by the mean of their observed $B_J - K$ colours at the mean cluster redshift ($< B_J - K >= 4.32 \pm .14$ mag. at $< Z >= .0386 \pm .0011$). A linear fit to the $(B_J - K) - Z$ is all that the data justifies under the circumstances. This relation, combined with the E-SOs blue K–correction which is discussed in the next section, will be used to derive the change in infrared magnitudes (2.2 μm) as a function of redshift.

Unfortunately, there are few detailed representations of the infrared K–corrections with which comparisons can be made. Griersmith et al (1982) compare $H - K$ colours for a nearby and distant cluster elliptical and derive $K\ (H - K) = 0.20$ mag. at $Z = 0.10$ which agrees very well with the polynomial prediction of 0.19 mag., estimated in this section (see Table 3.6). The stellar synthesis models of Bruzual and Kron (1980) reproduce fairly well the present day E-SO colours and the overall infrared C–Z relations (Lilly and Longair 1982; Lilly 1984; Ellis and Allen 1983; Ellis 1984). K–corrections can be derived from these model SEDs but adjustments are necessary to normalise the infrared colours at zero redshift. The $(B_J - K) - Z$ predictions as derived from both α Tau stars and Bruzual's C model SEDs are also included in Figure 3.2. These K–corrections have arbitrarily been normalised to the zero–point in the observed $(B_J - K) - Z$ diagram. They appear to agree closely with each other. However, they are systematically larger at $Z = 0.1$ than those implied by the present method. The effect is small (0.2 mag.) and perhaps not significant considering the intrinsic scatter in the data. The only selection effects that might operate on the data at these redshifts would be a bias towards more luminous objects for which a large C–L correction would apply or morphological misclassifications. The former can be ruled out because the C–L correction at $M_K = -26.5$ mag. (Table 3.2) is only 0.1 mag. and an error of 0.2 mag. here is out of the question. It is important to resolve this discrepancy by obtaining more optical and infrared photometry of intermediate distance E-SOs.

Finally, I emphasis that the advantage of this technique for deriving redshift–corrections is that it is entirely empirical and therefore reliable for reducing colours to $Z = 0.0$ regardless of any selection processes involved.

Figure 3.2

Infrared and optical–ir Colour–Redshift relations together with the polynomial fits to the AARS E-SOs (•). The cD galaxies (*) are also shown on this diagram and fit the polynomials fairly well. All the colours are reduced to a fixed absolute magnitude ($M_K = -25.00$ mag.). The observed mean colours of the Coma E-SOs (×) are shown.

On the $(B_J - K) - Z$ diagram the 'N2' cluster galaxies are represented by a single mean colour (□). Also, the predicted $(B_J - K) - Z$ relations for the Bruzual's C model (dashed line) and an α Tau SED (dotted line) are shown.

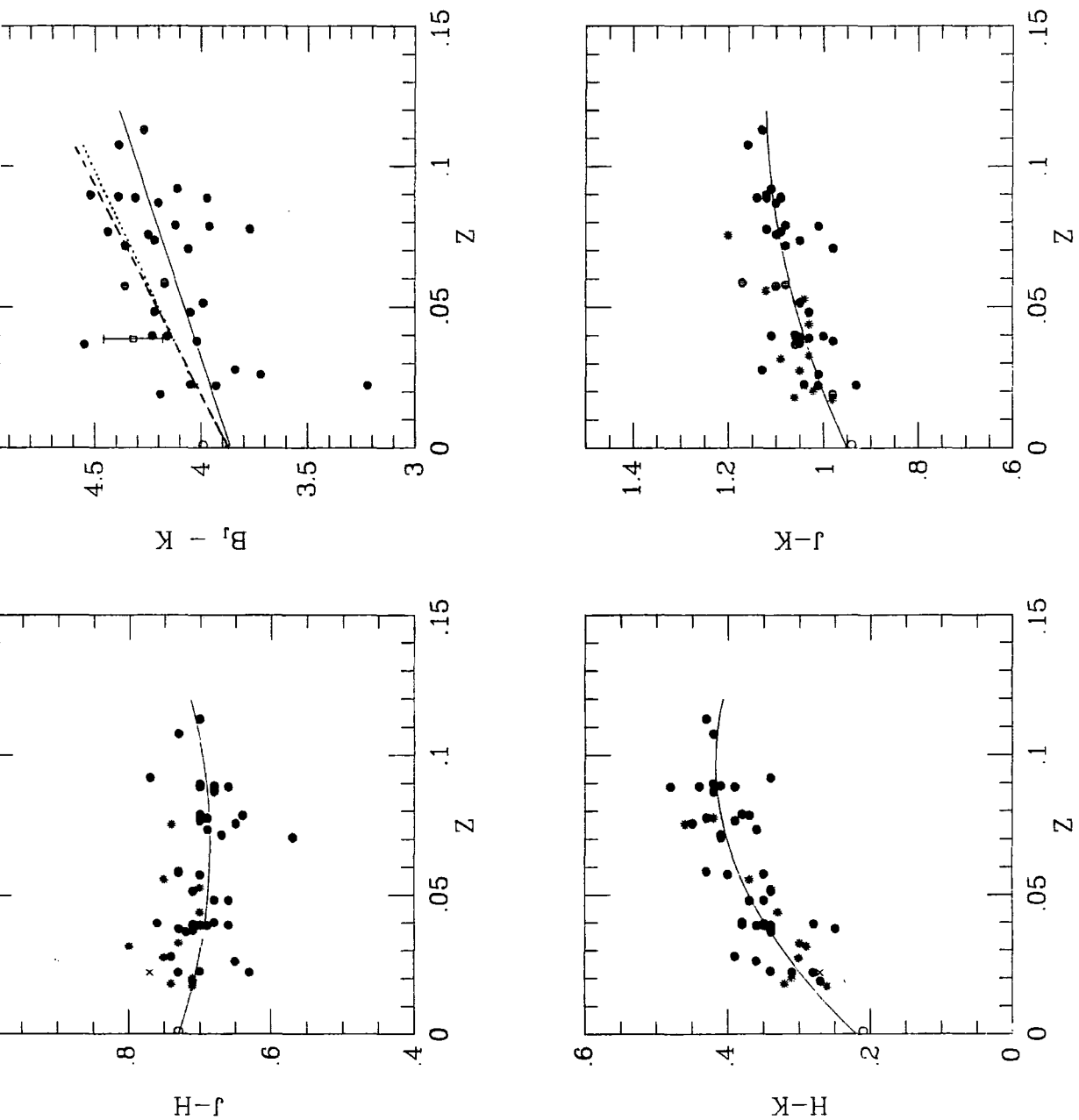

3.5 The K-Corrections for Optical and Infrared Magnitudes

The optical K–corrections used in this study are calculated from Pence's energy distributions for different morphological types (Pence 1976), shifted in redshift steps and convolved with the B_J filter at each step. The change in magnitude as a function of redshift for different morphological types is calculated and is represented by the polynomials listed in Table 3.7.

The E-SO K–correction in the K band can now be derived using the optical B_J K–corrections from Table 3.7 and the $(B_J - K) - Z$ relation discussed in the last section. At each redshift $B_J - K$ was corrected for the redshift effect in B_J and the resulting data used to determine the change in K with redshift. The result is listed in Table 3.6. I stress that all these redshift corrections are only valid for $Z < 0.10$ and that the polynomials should not be extrapolated beyond this range.

Table 3.6

List of the AARS Colour–Redshift polynomials and K–corrections for E-SO galaxies.

$$c = d + b\,Z + a\,Z^2$$

c	b	a	d	N	r.m.s.
$J-K$	2.72	−10.81	.95	40	.04
$H-K$	4.05	−20.83	.22	40	.03
B_J-K	4.38	—	3.86	34	.21
$K(K)$	−.69	3.19	—	–	

In order to test further the infrared K–corrections derived in this chapter, I use the polynomials from Table 3.6 and correct the infrared colours and M_K magnitudes of the cD galaxies to the rest–frame. I then compare the cDs with the rest–frame colours of nearby E-SOs by plotting them on Figure 3.1. It is clear that the cD galaxies lie at the bright end of the normal E-SO C–L diagram. The agreement supports the consistency of the infrared K–corrections derived in this chapter, provided cDs do not have an anomalous stellar content compared to other luminous E-SOs.

Table 3.7

Optical K–corrections from Pence's spectral energy distributions.

$$K\,(B_J) = a\,Z + b\,Z^2$$

Type	a	b
E–SO	3.69	3.19
Sa–Sab	3.00	2.16
Sb–Sbc	1.86	3.40
Sc–Scd	1.38	3.78
Sd–Sdm	0.59	4.74

3.6 Morphological Type Dependence of the Infrared K–Corrections

The infrared K–correction for E-SO galaxies was discussed in detail in section 3.4. The similarity of the stellar content of galaxies with different morphological types as apparent in the infrared should produce identical spectral energy distributions and consequently similar K–corrections for all the types (Aaronson 1977). The AARS provides the first opportunity for testing this hypothesis. Firstly, it has infrared magnitudes for galaxies of all morphological types and secondly it spans a redshift range over which the K–corrections are important.

The *observed* $J-K$ colour residuals for the spirals are calculated around the $(J-K)-Z$ polynomial of E-SO galaxies presented in Table 3.6. To explore the difference between the infrared C–Z relations of early–type and late–type galaxies, I plot the $J-K$ residuals against a type–dependent parameter such as B_J-K (Figure 3.3). The interesting feature of this diagram is that the $(J-K)$ residuals become smaller (the observed $J-K$ colours of spirals are bluer than the mean E-SO colours) as one approaches towards bluer B_J-K colours (later type galaxies). There could be two explanations for this trend :

1. The infrared K–corrections vary from early–to–late type galaxies.

2. The effect is due to a type–dependent $J-K$ C–L relation.

To investigate the first possibility I plot the $J-K$ residuals against redshift for all the AARS spirals in Figure 3.4; the slope is close to zero. A few blue galaxies at low redshift in Figure 3.4 have negative residuals and seem to produce a slight trend. However, this is more likely to be due to a C–L effect since these objects have a fainter luminosity with respect to the overall M_K distribution of the AARS spirals. One could therefore conclude that the trend in Figure 3.3 is mainly due to a type–dependence of C–L relation and not a difference between the infrared K–corrections of E-SO and spiral galaxies. I explore this in more detail in chapter 4.

Before closing this section I examine the AARS C–Z diagrams for possible sources of bias introduced by its magnitude–limited nature. If the late–type galaxies are on average fainter than early–types they will be preferentially found at lower redshifts. This would bias the spirals $(J-K)-Z$ relation if late–type galaxies have bluer mean infrared colours.

I investigate this point by calculating the mean redshift in morphological type bins and comparing the results in Table 3.8. It is clear from this table that there is *no correlation* between the mean redshifts and morphological types. This implies that the distribution of types is not dictated by redshift and therefore the infrared C–Z diagrams are not biased.

Figure 3.3

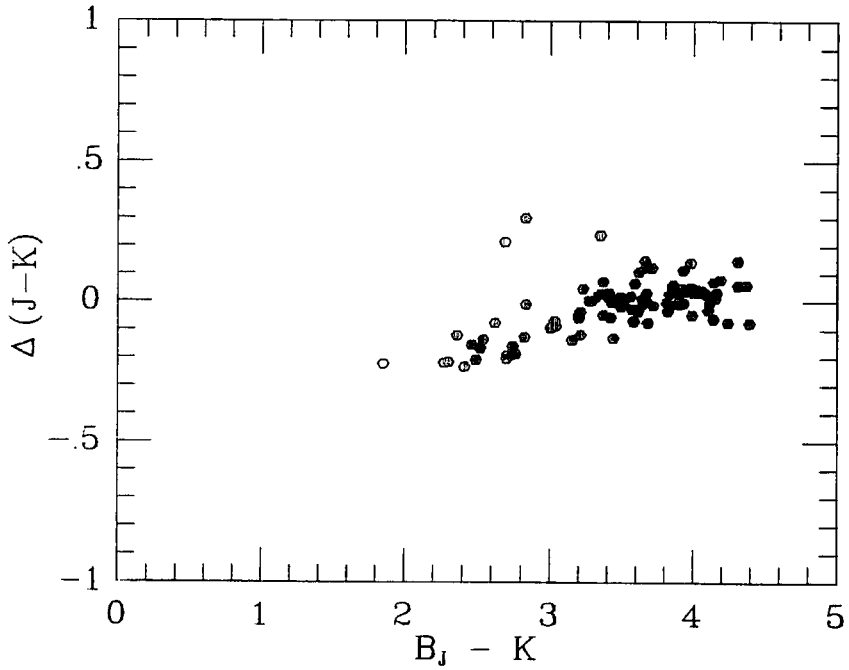

Figure 3.4

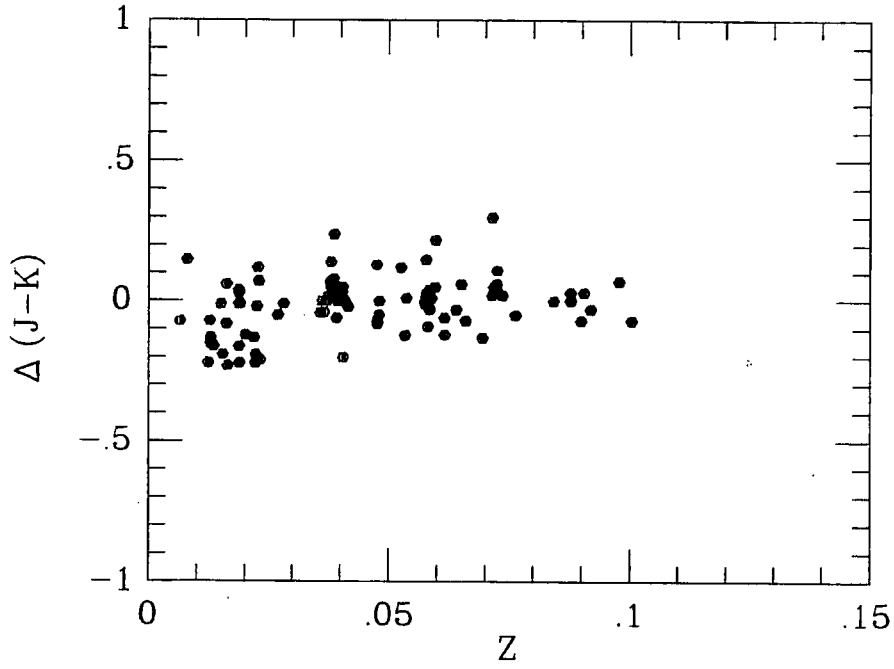

Table 3.8

Mean redshifts in morphological type bins.

Type	$< Z >$	N
E–SO	.0583	40
Sa–Sab	.0365	28
Sb–Sbc	.0482	36
Sc–Scd	.0494	27
Sd–Sdm	.0422	4

A second source of bias could be due to the exclusion of red (faint in B_J) galaxies from the sample. This will produce an artificial trend in the AARS C–L diagrams. In order to investigate this point I plot the difference between the $B_J - K$ and $J - K$ colours, corrected to a fixed absolute magnitude (using the relations derived in section 3.2), and their zero–redshift colours at $M_K = -25$ mag., as listed in Table 3.2, against the observed apparent B_J magnitudes in Figure 3.5. The slight trend in the $\Delta(B_J - K) - B_J$ diagram indicates the presence of a bias in our sample. However, considering the slope of this relation ($\sim 0.015 \pm 0.08$), the error introduced by the bias is significantly smaller than the intrinsic scatter in $B_J - K$ colours (see chapter 4) and hence it will not affect the results in the following chapters. One requires a deeper sample to establish the C–Z method properly. The study of C–Z relations in this chapter has proved to be a good start on the empirical derivation of K–corrections and a valuable independent check for them.

3.7 Fully Corrected Colours and Luminosities of the AARS Galaxies

Using the polynomials listed in Tables 3.6 and 3.7, I can now return to the original data (Table 2.3) and correct the observed colours and magnitudes of the AARS galaxies for the effect of redshift. Table 3.9 presents the fully–corrected infrared and optical–ir colours and K magnitudes for 135 galaxies in the AARS. Only objects with accurate infrared data and unambiguous morphological types are listed (galaxies which are classified as peculiars are excluded). Column 1 gives the name. Columns 2,3 and 4 list the inclination and redshift–corrected $J-H, H-K$ and B_J-K colours respectively. Columns 5 and 6 present the rest–frame apparent and absolute K magnitudes at $\log(A/D_0) = 0.00$. Morphological types are listed in column 7. The data from this table will be employed in the next chapters to study the infrared and optical–ir C–L relations.

Figure 3.5

Colour residuals between the $B_J - K$ and $J - K$ colours, corrected for C–L relation, and the zero–point colours as listed in Table 3.1, plotted versus the observed B_J.

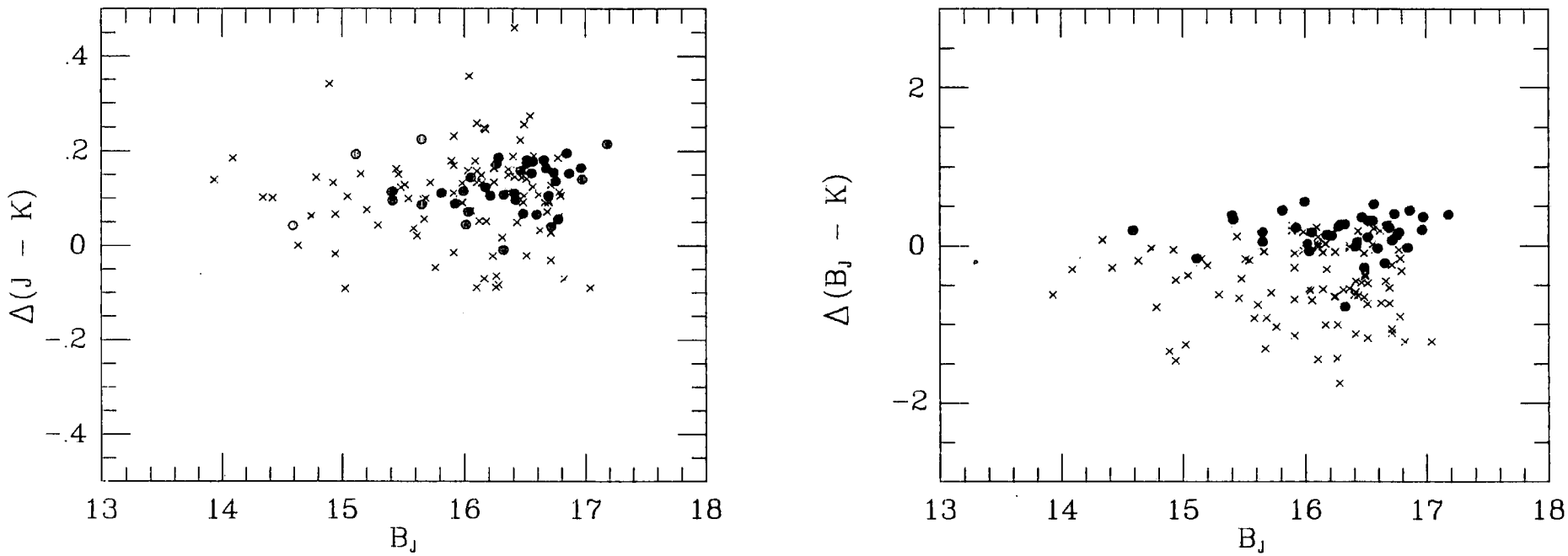

Table 3.9

Zero–redshift colours and absolute magnitudes of the AARS galaxies.

GALAXY	$J-H$	$H-K$	B_J-K	K	M_K	TYPE
S1 Field						
GSA002	0.72	0.22	3.87	10.84	−24.40	Sc
GSA004	0.78	0.24	4.02	12.73	−26.31	SO
GSA001	0.76	0.23	4.02	10.29	−24.95	Sbc
GSA003	0.76	0.24	3.15	11.57	−25.34	Sbc
GSA008	0.79	0.27	4.01	11.41	−26.31	SO
GSA014	0.78	0.20	3.98	11.85	−25.84	SO
GSA017	0.78	0.12	3.11	12.87	−23.78	SB
GSA013	0.77	0.13	3.83	12.03	−24.74	SO
GSA021	0.79	0.16	3.21	12.33	−25.40	Sa
GSA019	0.78	0.17	3.31	12.74	−24.94	Sbc
GSA024	0.81	0.18	3.73	12.33	−25.38	Sa
GSA026	0.73	0.22	3.11	12.98	−24.32	Sa
GSA039	0.76	0.20	3.37	12.92	−24.77	Sb
GSA028	0.85	0.13	3.69	12.61	−25.09	Sa
GSA037	0.84	0.26	4.10	12.26	−25.43	Sa
GSA038	0.75	0.19	3.76	12.45	−24.99	SO
GSA131	0.68	0.25	3.46	13.24	−23.74	Sb
GSA047	0.74	0.20	3.60	13.02	−24.66	Sc
GSA052	0.74	0.08	3.29	12.90	−25.19	Sc
GSA048	0.75	0.25	3.94	11.88	−27.27	E
GSA049	0.74	0.18	3.66	12.99	−24.92	Sb
GSA051	0.72	0.29	3.34	12.91	−25.93	Sb
GSA064	0.73	0.14	4.18	12.33	−26.56	Sc
GSA079	0.58	0.15	2.23	14.00	−21.25	Sc
GSA087	0.67	0.15	2.71	13.92	−23.60	Sbc
N2 Field						
GNB001	0.71	0.27	3.63	10.76	−24.48	Scd
GNB002	0.73	0.20	4.10	10.42	−24.84	E
GNB003	0.76	0.25	3.79	11.08	−23.84	Sab
GNB006	0.74	0.23	3.56	11.42	−25.38	Sc
GNB005	0.63	0.25	3.02	12.26	−20.65	Scd
GNB010	0.77	0.29	3.70	11.31	−24.79	SO
GNB015	0.59	0.24	2.33	12.59	−22.79	Sdm
GNB004	0.74	0.22	4.22	11.04	−25.79	E
GNB014	0.56	0.23	2.72	13.03	−22.20	Sdm
GNB009	0.75	0.23	4.28	10.97	−25.88	E
GNB013	0.75	0.27	3.78	11.31	−25.47	Sbc
GNB012	0.75	0.23	4.22	11.04	−25.79	E
GNB018	0.69	0.26	3.73	11.75	−25.10	Scd
GNB019	0.69	0.26	3.84	11.75	−25.18	Sc
GNB008	0.73	0.21	3.57	11.57	−23.69	Sab

GNB016	0.76	0.27	4.06	11.32	−25.44	Sbc
GNB024	0.65	0.22	2.97	12.59	−22.33	Sab
GNB020	0.75	0.23	3.75	11.70	−25.13	Scd
GNB017	0.76	0.21	4.31	11.35	−25.49	SO
GNB022	0.76	0.22	4.41	11.44	−25.26	SO
GNB023	0.75	0.26	4.27	11.55	−26.63	Sdm
GNB031	0.81	0.25	3.82	12.01	−25.48	Sbc
GNB050	0.71	0.18	4.06	12.31	−24.54	Scd
GNB029	0.73	0.27	4.17	11.81	−26.14	Scd
GNB034	0.79	0.20	3.73	12.29	−24.57	Sab
GNB030	0.72	0.25	3.94	12.07	−24.82	E
GNB025	0.77	0.26	4.05	11.72	−25.09	Sab
GNB041	0.75	0.35	3.64	12.45	−20.93	Sbc
GNB036	0.72	0.29	3.84	12.14	−24.65	Sab
GNB027	0.76	0.22	4.01	12.03	−24.87	Sbc
GNB032	0.68	0.28	3.59	12.26	−24.47	Scd
GNB033	0.71	0.26	3.48	11.94	−24.88	Scd
GNB040	0.70	0.25	3.93	12.13	−24.71	SO
GNB035	0.79	0.20	4.08	11.84	−24.95	Sbc
GNB011	0.71	0.23	3.75	12.15	−23.98	Sab
GNB039	0.74	0.17	3.89	12.15	−23.89	Sab
GNB037	0.74	0.22	4.08	12.10	−24.63	SO
GNB046	0.73	0.24	3.25	12.09	−26.06	Scd
GNB044	0.87	0.23	3.84	12.20	−24.58	Sa
GNB059	0.67	0.25	3.08	13.29	−23.41	Sab
GNB048	0.82	0.17	3.97	12.44	−24.31	Sbc
GNB047	0.70	0.17	4.10	11.97	−26.01	Sbc
GNB051	0.73	0.27	3.84	12.46	−24.43	Sc
GNB069	0.70	0.36	3.47	12.90	−25.28	Sbc
GNB052	0.77	0.20	4.01	12.43	−24.31	Sab
GNB053	0.70	0.29	3.87	12.56	−25.20	Sb
GNB055	0.73	0.21	3.98	12.52	−24.13	Sa
GNB057	0.79	0.21	3.72	12.62	−25.53	Sab
GNB056	0.89	0.30	3.21	12.71	−24.11	Sab

N1 Field

GNA002	0.77	0.31	3.63	10.39	−25.27	Sa
GNA001	0.72	0.31	3.31	10.57	−25.11	Sb
GNA003	0.68	0.20	3.63	10.96	−23.43	Sab
GNA004	0.57	0.18	2.62	12.34	−24.57	Sbc
GNA005	0.71	0.22	3.41	11.46	−24.18	Sa
GNA006	0.66	0.20	2.94	12.57	−24.70	Sbc
GNA007	0.65	0.22	2.50	13.08	−24.19	Sb
GNA008	0.67	0.27	2.79	12.86	−21.89	Sb
GNA009	0.71	0.22	3.89	11.58	−25.71	SO
GNA010	0.77	0.39	2.54	12.23	−25.53	Sb
GNA011	0.73	0.20	4.06	11.68	−25.62	SO
GNA012	0.57	0.19	2.67	13.47	−21.34	Sc
GNA013	0.73	0.19	3.70	12.24	−23.35	SO

GNA014	0.62	0.20	2.51	13.38	-21.04	Sb
GNA015	0.80	0.22	4.05	12.06	-24.82	SO
GNA016	0.75	0.23	3.16	12.59	-25.59	Sb
GNA017	0.86	0.21	3.57	12.53	-24.74	Sbc
GNA018	0.69	0.25	3.80	12.53	-23.11	SO
GNA019	0.75	0.24	4.15	12.09	-25.58	SO
GNA020	0.61	0.15	2.68	13.51	-22.10	Sa
GNA021	0.61	0.21	2.91	13.32	-22.28	SO
GNA022	0.51	0.22	2.22	13.81	-21.80	Sa
GNA023	0.65	0.16	3.07	13.09	-22.49	Sa
GNA025	0.82	0.43	2.57	13.61	-24.54	Sa
GNA026	0.67	0.25	3.90	12.30	-26.40	Sc
GNA027	0.69	0.14	3.08	13.44	-24.39	Sc
GNA028	0.74	0.24	3.47	12.88	-25.46	SO
GNA029	0.65	0.26	3.46	12.93	-23.03	SO
GNA030	0.76	0.23	4.26	11.95	-26.70	SO
GNA031	0.62	0.18	2.41	14.06	-20.34	Sa
GNA032	0.60	0.12	1.82	14.44	-19.90	Scd
GNA033	0.76	0.20	4.03	12.17	-26.45	SO
GNA034	0.75	0.22	3.17	13.14	-24.55	Sb
GNA038	0.69	0.18	3.68	12.61	-25.75	SO
GNA039	0.70	0.26	3.30	12.57	-25.64	Sb
GNA040	0.83	0.15	3.81	12.34	-26.36	SO
GNA041	0.71	0.19	3.25	13.35	-23.94	Sb
GNA042	0.58	0.21	2.49	14.20	-20.32	Sc
GNA043	0.68	0.30	3.22	13.03	-25.64	Scd
GNA044	0.74	0.25	4.04	12.12	-26.51	SO
GNA046	0.73	0.22	3.27	13.07	-24.47	Sa
GNA048	0.69	0.19	3.39	13.12	-25.53	Sbc
GNA049	0.62	0.23	3.79	12.64	-25.48	SO
GNA051	0.72	0.23	3.31	12.91	-25.60	Sbc
GNA052	0.71	0.18	3.07	13.52	-24.31	Sbc
GNA053	0.74	0.22	4.11	12.27	-26.36	SO
GNA055	0.71	0.28	3.64	12.85	-25.77	SO
GNA056	0.75	0.21	4.17	12.38	-25.92	SO
GNA057	0.73	0.24	3.88	12.74	-25.84	SO
GNA059	0.69	0.20	3.26	13.02	-25.27	Sc
GNA060	0.74	0.17	3.96	12.44	-25.77	SO
GNA062	0.74	0.15	3.93	12.69	-24.17	SO
GNA063	0.57	0.18	2.44	14.34	-21.37	Sbc
GNA064	0.66	0.20	2.92	13.81	-23.89	Sd
GNA065	0.72	0.19	3.49	12.91	-24.81	Scd
GNA067	0.70	0.27	3.99	12.38	-25.89	SO
GNA068	0.76	0.20	3.08	13.28	-25.32	Scd
GNA069	0.62	0.10	2.37	14.64	-20.30	Sb
GNA070	0.77	0.22	3.81	12.81	-25.79	Scd
GNA071	0.72	0.23	4.09	12.60	-25.55	SO
GNA073	0.75	0.19	3.83	12.61	-25.76	SO

3.8 Summary and Conclusions

The preliminary infrared and optical–ir C–L relations from nearby galaxies have been used to correct the observed colours of the AARS E-SO galaxies to a fixed absolute magnitude. These corrected colours have then been employed to determine the C–Z relation and the technique tested by using an independent sample of cD galaxies, observed over the same redshift range as the AARS.

The optical–ir C–Z relations of E-SOs have been used in conjunction with their optical K–correction to derive the variation in infrared magnitudes with redshift. The type–dependence of infrared C–Z relations has been examined and no variation in the infrared K–corrections with morphological type found. The rest–frame colours and magnitudes of the AARS galaxies have been calculated by employing the infrared K–correction polynomials derived from E-SOs and optical K–corrections from the appropriate SEDs.

CHAPTER IV

OPTICAL AND INFRARED COLOURS OF NORMAL GALAXIES

4.1 The Colour–Luminosity Relation

4.1.1 Background to the Colour–Luminosity Relation

The correlation between optical colours and luminosities of elliptical galaxies was first discovered by Baum (1959) and de Vaucouleurs (1961). Faber (1973) clarified the relation via observations of the strength of absorption features in the integrated spectra of these systems. She argued that the Colour–Luminosity (hereafter C–L) relation reflects the dependence of the mean metal abundance of elliptical galaxy stellar populations on the mass of the parent galaxy.

More recently, Sandage and Visvanathan demonstrated the existence of an optical C–L relation using a large sample of E-SO galaxies in clusters (Visvanathan and Sandage 1977) and in the field (Sandage and Visvanathan 1978b). By investigating the galaxian energy distributions, they searched for a colour index to maximise the C–L effect and also discussed the environmental dependence of this relation.

The C–L diagram for early–type galaxies was extended to near–infrared wavelengths by Frogel et al (1978) and Persson et al (1979) who studied the optical–ir C–L relations for E-SO galaxies in the field and in two nearby clusters, Virgo and Coma. These authors also considered the purely infrared colours, but did not find a significant change in infrared colours with absolute magnitudes.

In a study of the C–L relation for *disk* systems in the Second Reference Catalogue of Bright Galaxies (de Vaucouleurs, de Vaucouleurs and Corwin 1976; hereafter RC2), de Vaucouleurs (1977b) failed to find any significant correlation between optical colours and luminosities within a given Hubble type. If such a relation exists, presumably the contamination of optical colours by variable amounts of recent star formation would make its detection difficult. An optical–ir study of a sample of spiral galaxies of all Hubble types was carried out by Aaronson (1977) who also found no significant relation with luminosity, possibly because their absolute magnitude range was quite small. The first well–defined C–L relation for spiral galaxies was discovered by Griersmith (1980b), who studied the relation between optical colours of bulges of early–type spirals and their luminosities. However, he again failed to detect an infrared C–L relation for his sample (Griersmith et al 1982).

Employing both optical and infrared integrated magnitudes of spiral galaxies, Wyse (1982) and Tully et al (1982) independently found an optical–ir C–L relation consistent with a proportional increase of star formation in galaxies of lower luminosities, provided the metallicity decreases in these systems with decreasing mass or the mass function slope changes with mass. More recently, Bothun et al (1984) have found an infrared C–L relation for a sample of intermediate to late–type cluster spirals covering an absolute magnitude range of about 5 mag. By comparison with established infrared C–L relations from globular clusters with well determined metallicities, they claim that the mean metal abundance of the old disk population decreases with luminosity.

The variation of integrated colours of galaxies is expected to be a result of the chemical enrichment and star formation history, which give rise to a particular set of stellar contents. However, many fundamental problems are still unsolved. For example: why do the rate of star formation and chemical enrichment processes depend so tightly on the mass of the parent galaxy? What are the parameters that change as one moves along the C–L relation? What are the composite HR diagrams for stellar populations of different types of galaxies and how do they change as one moves along the Hubble sequence? What is the implication of type–dependence, if any, of the C–L relation? The data presented in this thesis will serve to consider these questions.

4.1.2 The AARS C–L Relation

Using the corrected colours and magnitudes of the AARS galaxies presented in Table 3.9 I now study their infrared and optical–ir C–L relations as a function of morphological type. The AARS is regarded as representative of a 'field' sample. The term 'field' is used loosely here to represent samples not connected to rich clusters like Virgo and Coma. The AARS does contain a representative number of galaxy groups because the correlation function found by Shanks et al (1984) matches well that seen in other more extensive, all-sky surveys. To improve statistics and increase the absolute magnitude range covered by E-SOs I also include the 'field' galaxies from the literature which were analysed in Chapter 3. In order to examine the possibility of type–dependence of the C–L relations I initially divide the AARS sample into two broad morphological bins: ellipticals and lenticulars (E-SO) and spiral galaxies (Sa-Sdm). In this section I study the infrared and optical–ir C–L relations for the two broad morphological classes, concentrating first on the infrared C–L relation.

The present situation concerning the existence or otherwise of an infrared C–L relation for galaxies is far from clear. Several studies (e.g. Frogel et al 1978) have failed to detect a significant infrared C–L relation for 'field' E-SO galaxies despite the provisional results in the last chapter. In addition, Bothun and Caldwell (1984) find no relation for dwarf ellipticals in nearby clusters, whilst Bothun et al (1984) interpret the well established optical C–L relation for normal E-SOs in terms of variations in the number of blue horizontal branch stars. The existence of an infrared C–L relation for E-SOs would argue against this and provide important information on the mass–metallicity relation as a function of morphology, since Bothun et al (1984) claim to observe an infrared C–L effect in late–type cluster spirals.

The infrared C–L relations for the two broad morphological classes are presented in Figures 4.1a and 4.1b and their linear least–square fits are listed in Table 4.1. The deviant point in the spirals' C–L relation (Figure 4.1b) is GNB041 which has anomalously red colours for its luminosity. This galaxy has a poorly determined redshift and could, therefore, conceivably have a higher luminosity. Upon excluding this galaxy, however, the slope of the spirals' C–L relation does not change significantly. The extinction vectors drawn on Figure 4.1 are found from Van de Hulst reddening curve no. 15 (Johnson 1966).

In the case of the E-SOs, the luminosity range of the AARS sample is rather restricted ($-22 < M_K < -27$) making it difficult to detect a reliable trend. Certainly it appears to be flatter than that for the spirals but the slope is highly uncertain. The fit is also sensitive to a few faint galaxies. This raises the question of whether a few faint and possibly misclassified objects could produce the apparent trend.

To overcome these problems I now exploit a published sample of 76 'field' E-SOs presented in Table 3.1. I exclude obvious cluster galaxies (such as those belonging to Virgo and Coma), so that the sample is drawn from a similar environment to that of the AARS. This doubles the number of E-SOs with $M_K > -22$ mag. and adds three much fainter galaxies. The trend is, however, still weak. Indeed the published sample has a slightly weaker relation with a flatter slope than the AARS.

The lack of low luminosity ellipticals in this sample could well have a strong effect on the slope of the E-SO C–L relation. For example, the presence of three galaxies (N205, N221 and N404) with $M_K > -20$ mag. is crucial for the existence of a reliable C–L relation for E-SOs in Figure 4.1a. Excluding these three galaxies, the correlation coefficient, r, of the $(J-K)-M_K$ relation reduces from -0.47 to -0.40. One might therefore ask: how significant is the slope of the infrared C–L relation of E-SO galaxies? A Student's t–test shows that the relation for the combined sample of 116 'field' E-SOs is significant at better than the 99% confidence level.

The $(B_J-K)-M_K$ diagrams are also plotted in Figures 4.1a and 4.1b with the least–square fits listed in Table 4.1. In the case of the E-SOs the published 'field' sample from Table 3.1 is also included. Again the E-SO slope is flatter than that seen for the spirals. The $(B_J-K)-M_K$ relations for the AARS and published E-SOs are in close agreement when a single anomalous emission–line galaxy (GNA021) is excluded. The spectrum of this galaxy shows $[OII]$ and weak $[OIII]$ emission lines and its B_J-K colour is relatively blue. There are a total of ten such objects amongst the AARS E-SO galaxies. Although $[OII]$ emission lines are found in $\sim$ 25% of 'field' E-SOs (Dressler, Thompson and Schectman 1985), type misclassifications cannot be ruled out in individual cases. The combined AARS/literature sample is therefore adopted as the best estimate of the 'field' $(B_J-K)-M_K$ relation for normal E-SOs.

Figure 4.1a

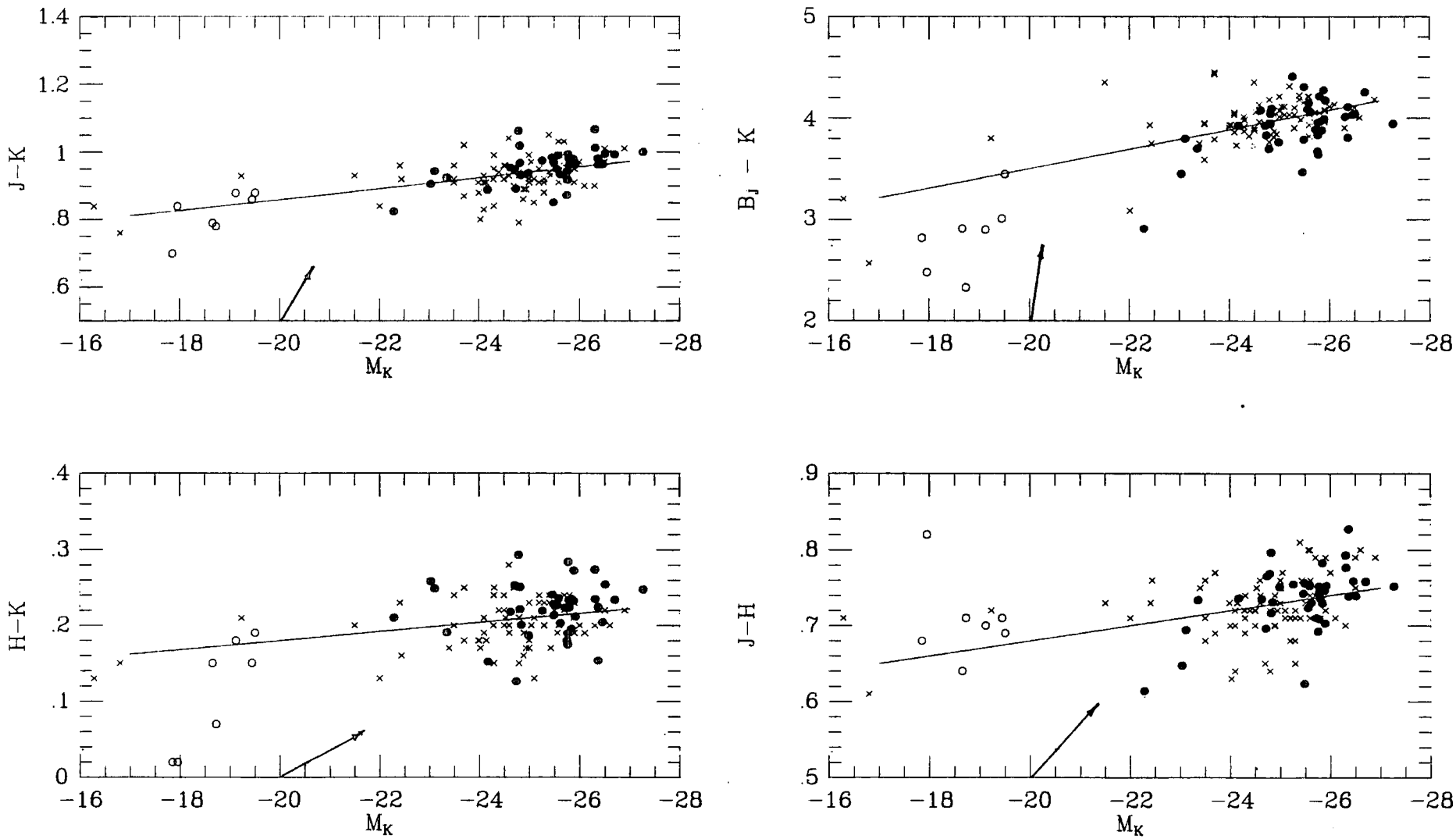

Figure 4.1b

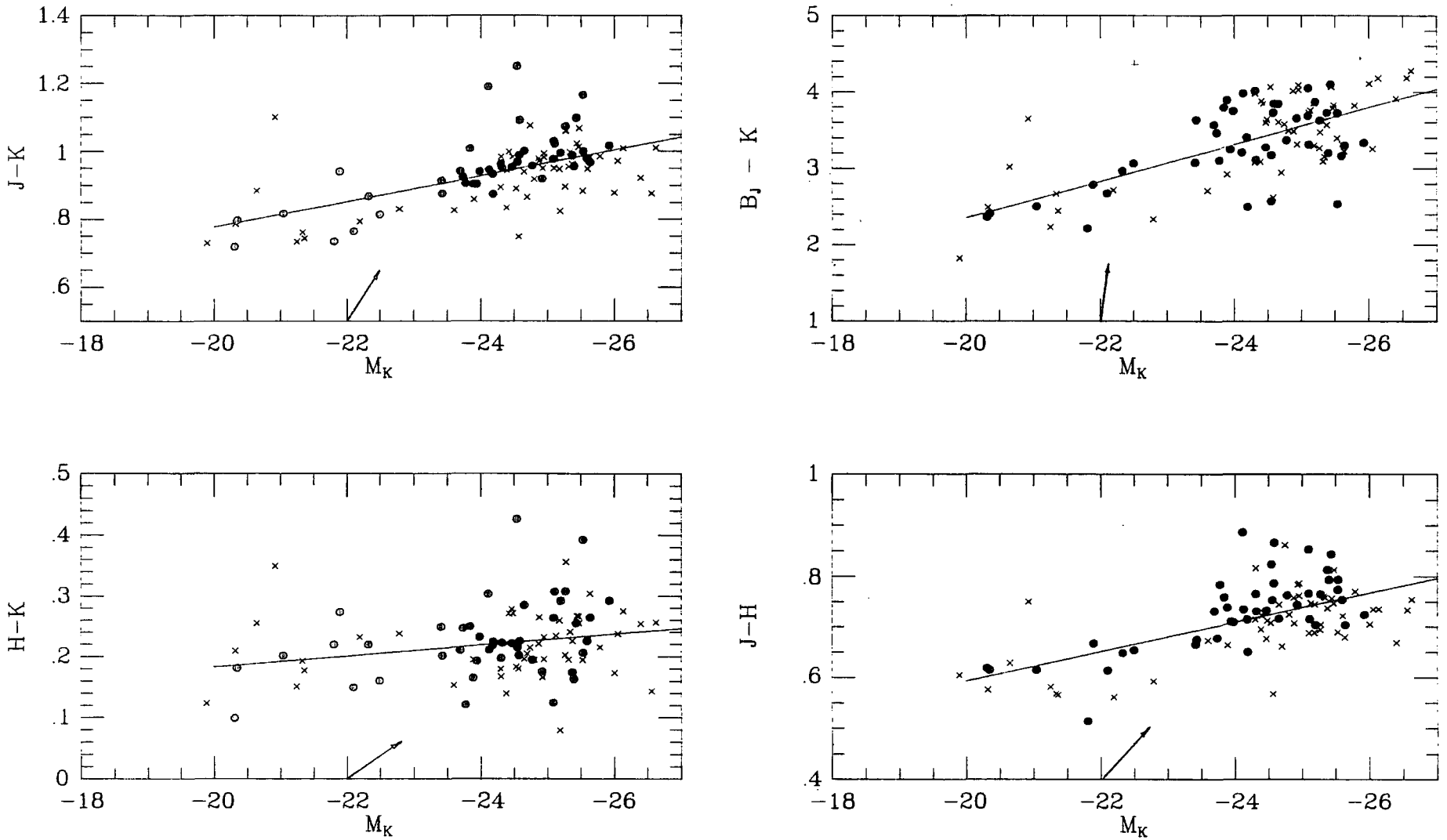

Table 4.1

Colour–Luminosity Relations

$$COL = A + B\,(M_K + C)$$

COL	A	$-B$	C	r	$r.m.s.$	N	Sample
E-SO							
$J-H$	0.73 ±.01	0.021 ±.006	25	−0.52	0.04	40	AARS
$J-K$	0.95 ±.01	0.023 ±.007	25	−0.50	0.04	40	AARS
B_J-K	3.91 ±.04	0.092 ±.04	25	−0.40	0.19	39	AARS
$J-H$	0.73 ±.01	0.008 ±.003	25	−0.34	0.04	76	Literature
$J-K$	0.94 ±.01	0.014 ±.003	25	−0.43	0.05	76	Literature
B_J-K	4.02 ±.03	0.096 ±.01	25	−0.64	0.20	76	Literature
$J-H$	0.73 ±.01	0.010 ±.002	25	−0.39	0.04	116	AARS + Literature
$J-K$	0.94 ±.01	0.016 ±.003	25	−0.47	0.05	116	AARS + Literature
B_J-K	3.98 ±.02	0.095 ±.013	25	−0.57	0.22	116	AARS + Literature
Sa-Sb							
$J-H$	0.69 ±.01	0.037 ±.006	23	−0.70	0.05	44	AARS
$J-K$	0.90 ±.01	0.055 ±.008	23	−0.72	0.08	44	AARS
B_J-K	3.08 ±.08	0.22 ±.05	23	−0.60	0.39	44	AARS
Sbc-Sdm							
$J-H$	0.67 ±.01	0.026 ±.005	23	−0.63	0.05	51	AARS
$J-K$	0.88 ±.01	0.030 ±.007	23	−0.55	0.08	51	AARS
B_J-K	3.06 ±.08	0.24 ±.04	23	−0.71	0.40	51	AARS

Sa-Sdm							
$J-H$	0.68 ±.01	0.029 ±.004	23	−0.62	0.06	95	AARS
$J-K$	0.89 ±.01	0.038 ±.006	23	−0.59	0.08	95	AARS
B_J-K	3.07 ±.05	0.24 ±.03	23	−0.67	0.40	95	AARS

The spiral galaxies in the AARS sample show a much greater range in B_J-K colours and a larger scatter at a fixed absolute magnitude. The B_J-K colour residuals (from rest–frame colours corrected for luminosity) have been checked against galaxy inclination but no clear trend is seen. More likely, variations in bulge–to–disk (B/D) ratio play an important role. It has been shown that optical–ir colours are strongly correlated with B/D ratios for a sample of 'field' Sa–Sc spirals (Whitmore 1984). Unfortunately, accurate decomposition of the surface brightness profiles of the faint AARS galaxies for determining B/D ratios is not feasible. Choosing a more indirect approach I will demonstrate later in this chapter that indeed a variation in B/D ratios is the likely parameter responsible for some of the scatter in the optical–ir colours of spirals.

In summary, there is fairly convincing evidence for an infrared C–L relation for both spiral and E-SO galaxies but the E-SO slope is considerably flatter. More observations of 'field' E-SOs in the $-22 < M_K < -18$ mag. range are needed to determine the slope precisely. Also, a statistically significant trend is found between the B_J-K colours and M_K luminosities of both E-SO and spiral galaxies and the E-SOs' relation is again relatively shallower. The AARS spirals show a larger scatter in B_J-K colours at a fixed luminosity.

4.1.3 Search for a Metallicity Indicator

In order to study the role of metal abundance in the C–L relation of disk galaxies, one requires a measure of metallicity which is insensitive to the changes in the young/old stellar population mix caused by on–going star formation processes. The infrared $J-K$ colours measure primarily the mean effective temperature of the giant branch which in turn is sensitive to metallicity (Cohen et al 1978)- (lower metallicity giants have higher effective temperatures). This can be understood through the following sequence: since metals are the primary electron donors in the outer envelope of giant stars, the metal abundance controls the number of H^+ ions per gram of material at the surface of a star and hence the envelope opacity. For fully convective stars, the envelope opacity indicates the stellar radius and hence the temperature of the star at a given luminosity.

The power of the $J-K$ colours as a metallicity indicator was tested by Aaronson et al (1978), who demonstrated the existence of a trend between metal abundance and $J-K$ colours for Galactic globular clusters. The insensitivity of $J-K$ colours to the blue light of a galaxy has been amply examined by Thuan (1983), who showed that the $(J-K)-[Fe/H]$ relation of globular clusters also fits a sample of dwarf galaxies with high star formation rate. This is also clear from Figure 4.2, which plots the $J-K$ and B_J-K colours against the $[OII]$

Figure 4.2

The $[OII]\lambda 3727$ equivalent widths versus $J-K$ and B_J-K indices for those AARS galaxies with noticeable emission lines.

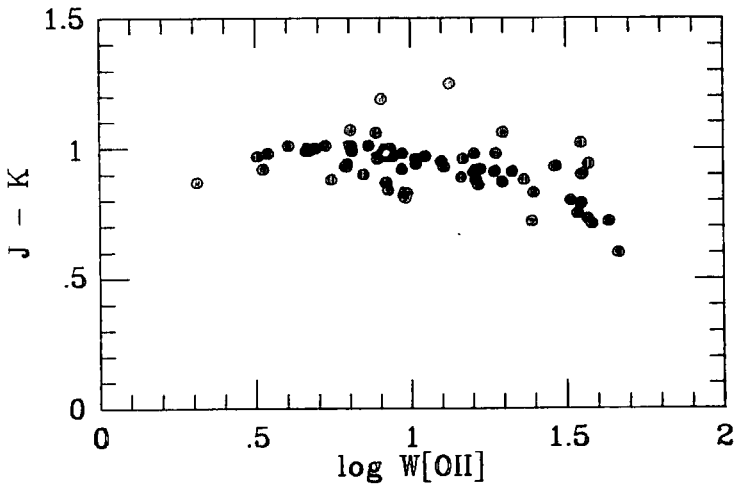

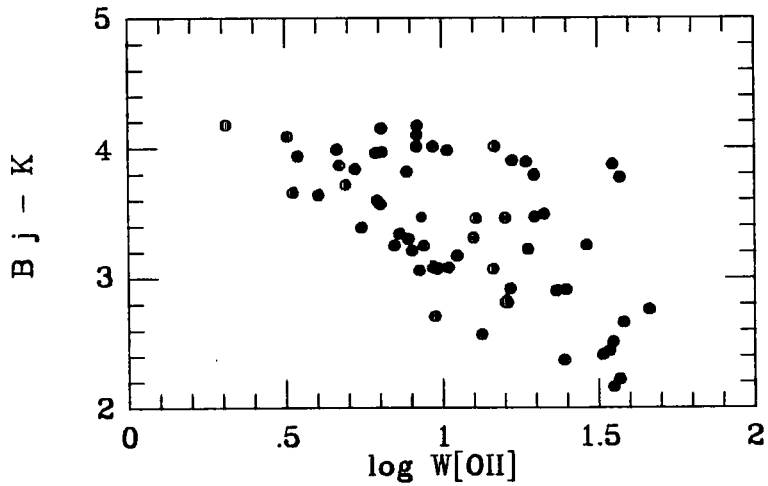

strengths of the AARS emission–line galaxies. In contrast to the $B_J - K$ colours, the $J - K$ colours hardly change with emission line strength (which indicates on–going star formation bursts in galaxies (Kennicutt 1983)). In galaxies with star formation activities, the $J - K$ colours could only be affected in a period when M supergiants are present. However, this time scale is short ($< 10^7$ yrs) and most galaxies would not be observed during this phase.

The only problem in using $J - K$ colours as a metallicity indicator is their sensitivity to the asymptotic giant branch (AGB) population which is the descending giant branch of intermediate age. The contribution to the infrared light from the AGB stars can be further investigated on a $(J - H) - (H - K)$ diagram (Persson et al 1983).

4.1.4 Dwarf Elliptical Galaxies

Infrared observations of dwarf ellipticals (dEs) when compared with the same data for giant ellipticals provide a new tool for studying the evolution of elliptical galaxies as a function of their mass and for extending the mass–metallicity relation of giant ellipticals to low mass objects. A sample of seven dwarf elliptical galaxies in the Virgo cluster with known infrared (Bothun et al 1985b) and optical (Caldwell 1983) magnitudes will be used in this section to explore these points. The following steps are taken to reduce their observed magnitudes to the AARS system.

Available visual surface brightness distributions for four of these galaxies (Caldwell 1983) were used to estimate their isophotal diameters at 25 mag./arcsec^2. The rest of the dwarf ellipticals were then assumed to have diameters corresponding to the mean diameters of these objects.

Infrared magnitudes from Bothun et al (1985b) are available over an 11 arcsec. aperture. The aperture–to–diameter ($\log(A/D_0)$) ratios were formed and the K–growth curve from Frogel et al (1978) was employed to estimate corrections to $\log(A/D_0) = 0.00$. This procedure makes the assumption that aperture–magnitude relations at infrared wavelengths are the same for giant and dwarf ellipticals since Frogel et al (1978) constructed their growth curve from normal E-SO galaxies. Aaronson, Huchra and Mould (1979) show that the infrared growth curves are similar for different morphological types. Although their result appears to support the above assumption, nevertheless, this remains the most serious question in this reduction procedure.

Caldwell (1983) presents optical photometry for dwarf elliptical galaxies over an aperture of $\sim$ 36 arcsec. which roughly corresponds to their diameters at 25 mag./arcsec^2. Therefore, the correction needed to convert the blue magnitudes to $\log(A/D_0) = 0.00$ is small and again is estimated following the above procedure.

The slope of the colour–aperture relation for dwarf ellipticals is not available and hence the correction required to the blue magnitudes due to colour gradients is unknown. Assuming the slope of spirals' $\Delta\,(B - K) - \log(A/D_0)$ relation (Chapter 2) and the mean $\log(A/D_0)$ values (~ -0.2), I estimate a correction of 0.08 mag. for the $B - K$ colour gradient. Taking the E-SOs' slope the correction

becomes 0.03 mag. The correction for colour gradient to the optical–ir colours of dEs is therefore small, and so is neglected in what follows.

The $B-K$ colours were converted to B_J-K by using the relation given in Chapter 3. The infrared colours from Bothun et al (1985b) were transformed to the Johnson system by employing the relation given in Frogel et al (1978). A distance modulus of 31.70 mag. was assumed for Virgo (Sandage and Tammann 1976). Infrared and optical–ir colours and magnitudes of dEs in the Virgo cluster (corrected to the AARS system) are listed in Table 4.2.

Table 4.2

Dwarf elliptical galaxies in the Virgo cluster.

	Name	$(H-K)$	$(J-H)$	(B_J-K)	M_K
M87	DW1	0.15	0.71	3.01	−19.44
	DW6	0.19	0.69	3.45	−19.50
	DW8	0.15	0.64	2.91	−18.65
	DW11	0.07	0.71	2.33	−18.72
	DW22	0.18	0.70	2.90	−19.11
	DW27	0.02	0.68	2.82	−17.85
	DW31	0.02	0.82	2.48	−17.95

Note: A distance modulus of 31.70 mag. is adopted for the Virgo (Sandage and Tammann 1976).

The dwarf elliptical galaxies are compared on Figure 4.1a with the E-SOs. They do not fit the faint end of the infrared C–L relation and are bluer in B_J-K than a linear extrapolation of the E-SO relation to faint luminosities. The mean $J-H$ colours of dEs are redder by 0.10 mag. and their $H-K$ colours are bluer by the same amount than normal E-SOs of the same luminosity. This deviation in the infrared is, however, a 1σ effect and is not significant. In the case of the B_J-K colours, a colour gradient term is too small to explain this difference. One therefore concludes that at a given absolute magnitude, the B_J-K colours of dwarf ellipticals are significantly bluer than normal E-SOs by as much as 0.80 mag.

4.1.5 A Surface Brightness – Colour Relation for the AARS Spirals

In this section I study the observed scatter in the $B_J - K$ colours of spirals at a given luminosity (section 4.1.2) by considering the relations between their optical–ir colours and other observable parameters.

Whitmore (1984) has already shown that $B - H$ colours are strongly correlated with B/D ratios for a sample of 'field' Sa-Sc spirals. Also, optical studies of spiral galaxies have revealed that bulges are both redder (Boroson 1981) and of higher mean surface brightness (Simien and de Vaucouleurs 1983; 1986) than disks. One could therefore anticipate that bulge dominated systems will have redder $B_J - K$ colours and higher surface brightnesses than disk dominated systems. This conjecture is supported by a correlation between infrared surface brightness and infrared luminosity discovered by Van den Bergh (1981; see also Kraan–Kortweg 1983 and Bosma 1985) for the cluster spirals of Aaronson, Mould and Huchra (1980) and Aaronson et al (1980). Since both infrared surface brightness (μ_K) and optical–ir colours depend strongly on infrared luminosity, it will be interesting to examine whether the residuals about the $(B_J - K) - M_K$ and $\mu_K - M_K$ relations are correlated for the AARS spirals.

Burstein (1982) has shown that the observed variation in the surface brightness parameter ($\mu_K = K_0 + 5 \log D_0$) is significantly larger than systematic effects like colour or type–dependence. The $\mu_K - M_K$ diagram for the AARS spirals is presented in Figure 4.3. Different types are shown by different symbols and the least–squares fit to this relation is found to be

$$\mu_K = (0.20 \pm .05)(M_K + 23) + (19.90 \pm .10) \quad r.m.s. = .73 \qquad 4.1$$

Equation 4.1 is combined with the spirals' $(B_J - K) - M_K$ relation in Table 4.1 to establish the surface brightness–colour residuals diagram as plotted in Figure 4.4.

Clearly there is a significant correlation between the surface brightness and colour residuals with redder galaxies having larger surface brightnesses. A least–squares fit gives

$$\Delta(B_J - K) = (-0.32 \pm .04)\,\Delta(\mu_K) - (0.01 \pm .03) \quad r.m.s. = .32 \qquad 4.2$$

This correlation is now used to correct the spirals in the $(B_J - K) - M_K$ diagram for any effect correlated with mean surface brightness. Whilst this reduces the scatter in the relation from 0.40 to 0.31 mag. it remains significantly larger than the estimated observational errors ($\sim$ 0.15 mag.). This intrinsic scatter in the C–L relation will be studied in section 4.3.

It is important to find the main parameter which is responsible for the observed trend between the residuals in Figure 4.4. The sample of Sa-Sc spirals with measured B/D ratios and $B - H$ colours is taken from Whitmore (1984). The surface brightness and $B - H$ colour residuals for individual galaxies in this sample were found and their mean values in B/D bins were calculated. There are at least five galaxies in each B/D bin. The trend on Figure 4.4 due to variation in B/D ratios is shown by a solid line. For large B/D ratios the mean line fits

Figure 4.3

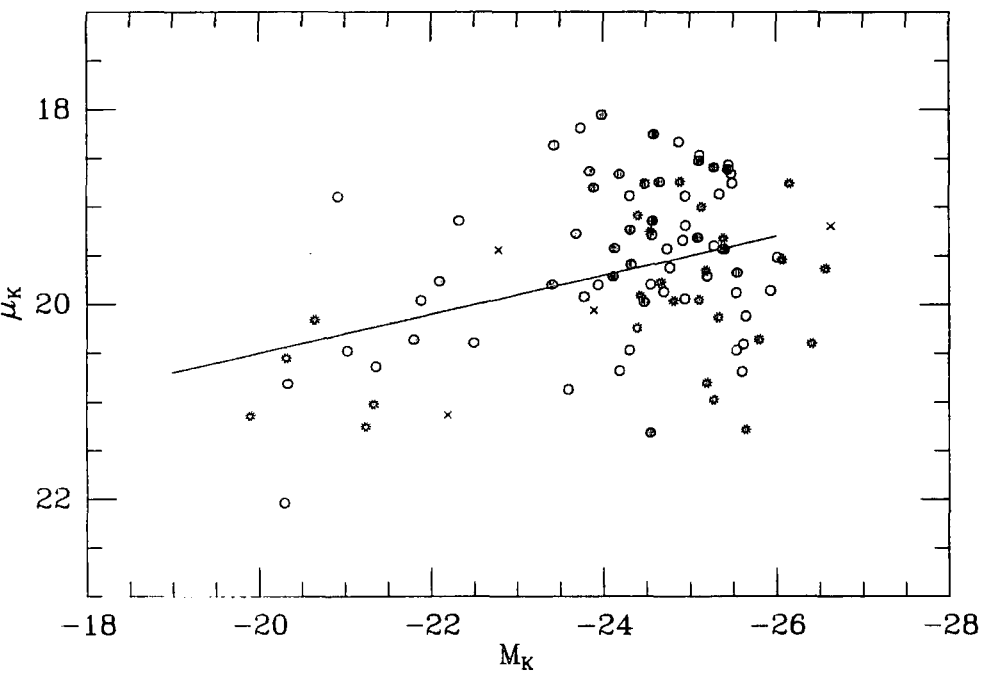

Figure 4.4

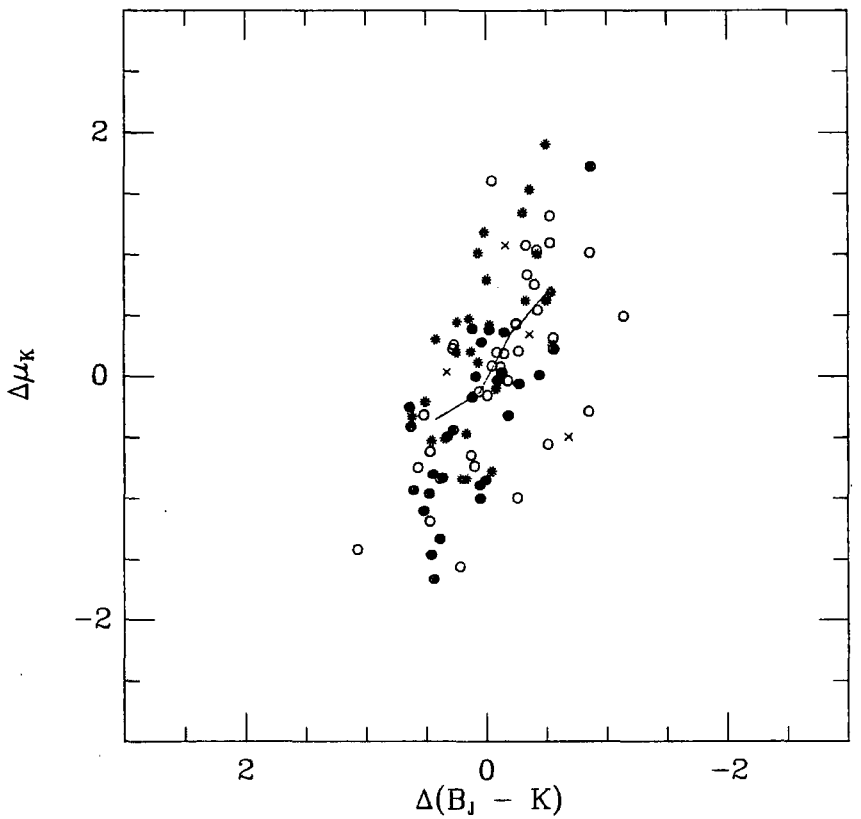

the observed residuals diagram fairly well implying that the variation in this parameter amongst the spirals is probably responsible for the scatter in their optical–ir colours at a given absolute magnitude.

4.1.6 Discussion

Observations of line indices and broad band optical colours, predominantly for E-SO galaxies, indicate that the $C-L$ trend is the result of a metallicity–mass relation, with massive systems being more metal rich. Hence the slope of the C–L relation for E-SO galaxies is primarily determined by a change in integrated metallicity with galaxian mass.

Support for metallicity as a driving factor in the C–L relations comes from considerations of the slopes of the E-SO C–L relations seen independently in $B_J - K$ and $J - K$. The ratio of these slopes should, in this case, be equal to the slope of the metallicity vector on the $(B_J - K)$ vs $(J - K)$ colour–colour diagram. The equivalent vector determined for the M31 globular clusters (Frogel et al 1980; Sitko 1984) is:

$$\Delta(B_J - K)/\Delta(J - K) = 2.64 \pm 0.21 \qquad 4.3$$

which agrees closely with the value of 2.66 ± 0.38 for the E-SO galaxies. Even excluding the three faintest E-SOs from the sample I derive a slope of 1.96 ± 0.36 for the $(B_J - K) - (J - K)$ relation of giant E-SOs which agrees within 2σ with the slope from the globular clusters.

The apparent absence of an infrared C–L relation for 'field' E-SOs led Bothun et al (1984) to propose that the optical C–L relation for E-SO galaxies is due to a variation in the number of blue horizontal branch stars. However, if horizontal branch stars were responsible one would also expect to find a strong C–L relation at ultraviolet wavelengths, but none has been found (Bertola, Capaccioli and Oke 1982). The results from this study show an infrared C–L relation does exist and thus that metallicity is the dominant parameter in producing the C–L trend in E-SO galaxies.

Since $J-K$ colours are relatively insensitive to star formation, the $(J-K)-M_K$ relation for spirals implies a metallicity trend as well. The role of metallicity in the infrared C–L relation of spirals has also been assessed by Bothun et al (1984) who employed a synthesis model incorporating both metallicity and star formation.

One of the principal results here is that the E-SO C–L relations are much flatter than those for spiral galaxies. This strongly suggests that variations in the rate of metal production with luminosity (i.e. mass) in spirals is higher than in E-SOs. In a study of the optical colours of bulges of spiral galaxies, Griersmith (1980b) showed that metallicity in the bulges of early type spirals and E-SOs varies in the same way with luminosity. Bearing in mind the fact that, in this study, large apertures have been used and hence light from both disk and bulge populations is sampled, I conclude that, under the conventional interpretation, the different slopes of the spiral and E-SO C–L relations imply greater metallicity

variations with luminosity in disk stars than in spheroidal systems. Adopting the metallicity calibration of Aaronson et al (1978), one could infer a change by a factor $\sim$ 10 in metallicity across 5 magnitudes of luminosity in E-SOs compared to a factor 40 for spiral galaxies.

In the case of the $(B_J - K) - M_K$ relation of spirals the situation becomes more complicated. This relation can be explained by invoking three parameters:

1. metallicity,

2. star formation,

3. age.

Generally speaking, any change in $B_J - K$ colour results from processes that control the mean effective temperature of the giant branch (e.g. metallicity and contribution from the AGB stars) or those that alter the population of the upper main sequence (e.g. star formation and disk turn–off age) since $B_J - K$ ultimately measures the giant–to–dwarf ratio.

Employing stellar synthesis models in the next section I show that the metallicity variation plays an important role in determining not only the $J-K$ colours of spirals, but also their $B_J - K$ colours. Changes in the past history of star formation produce only limited changes in the $B_J - K$ colours (and a negligible effect on the $J-K$ colours) compared with their overall range of > 2 magnitudes. The scatter in $B_J - K$ at a fixed $J-K$ should thus largely be explained by variations in the current star formation rates and B/D ratios amongst the spirals. Thus it is difficult to infer accurately the form of the star formation decrease from present day colours.

The mean $B_J - K$ colours of dwarf ellipticals (at a given M_K) are bluer than E-SOs by 0.80 mag. This is in agreement with the results from Bothun and Caldwell (1984) and might be explained if either

1. Star formation is still on–going in dEs,

2. dEs have much lower metallicities than 'field' E-SOs.

On–going star formation in dEs seems unlikely from constraints on their HI content (Bothun et al 1985b). The fact that the mean $J - K$ colour of dwarfs ($< J - K >= .85$ mag.) is bluer than that for the normal luminosity E-SOs ($< J - K >= .95$ at $M_K = -25$ mag.) tends to support the second possibility mentioned above. However, there is evidence from the luminosity function of dEs (Sandage, Bingelli and Tammann 1985) that these galaxies contain a stellar population which is not present in luminous 'field' E-SOs and hence they may be from a different family than normal ellipticals.

Compared to normal spirals, dEs have redder mean $J - K$ and $B_J - K$ colours than spirals with the same luminosity. This casts doubt on the Lin and Faber (1983) theory that dEs result from low metallicity irregulars whose gas has been stripped off through tidal forces or environmental effects. Their relatively redder $B_J - K$ colours with respect to low luminosity spirals combined with

the comparably bluer $B_J - K$ colours than E-SOs implies that dEs are in a transitionary state between normal spirals and low mass E-SOs.

4.2 Comparison with Stellar Synthesis Models

4.2.1 Description of Models

The conventional technique for building stellar synthesis models is to allow the stars to evolve in the HR diagram according to a given initial mass function (IMF) and star formation rate (SFR). With libraries of stellar spectra, it is then possible to construct the composite integrated spectra of the model galaxy and produce its present day colours.

In order to construct the models, the theoretical evolutionary tracks of stars in the $\log L - \log T_e$ plane are converted into age–flux tables. The isochrones indicate the time spent by a star at a given stage of its evolution. The lifetime of a galaxy model under construction is divided up into a large number of time steps of equal duration. The flux of a given type of star is then integrated over its age to give the total flux produced by that type during its lifetime. This is then multiplied by the number of stars with the same spectral type formed in the same time step of the lifetime of the model galaxy (from the initial mass function). Summing up the integrated fluxes over different spectral types and different time steps gives the present day composite flux of the galaxy.

A synthesis model constructed for globular clusters and kindly provided by Chris King of Yale University will be used in this section to interpret the colours of E-SO and spiral galaxies. It has a distinct advantage over earlier work in that improved isochrones are available and predictions are possible in precisely the passbands used for the AARS. This is a theoretical model which follows the prescription of Aaronson et al (1978) for the integrated colours of globular clusters assuming a single burst of star formation. The new Yale isochrones and luminosity functions form the basis of these models (Green, Damarque and King 1985). They incorporate main sequence and early giant branch (GB) evolutionary stages. The models do not use the full giant branch because it goes beyond the tip observed in globular clusters. No horizontal branch (HB) stars were added because of their unknown evolutionary history. The appropriate HB isochrones are urgently needed to refine the models in this respect. Above the HB the first giant branch luminosity function is multiplied by 1.25 to mimic the AGB. The lower main sequence was extrapolated to a lower cutoff mass of $0.1\,M_\odot$. The effect of varying this cutoff mass to $0.4\,M_\odot$ is less than 0.10 mag. in $B_J - K$ and 0.02 mag. in $J - K$. Omitting the AGB stars changes the colours by a similar amount.

Single age models were constructed for ages in the range 1–20 Gyrs for three IMF slopes ($X = -1$, 1.35 and 3, where $X = s - 1$ in the notation of Tinsely 1972) and for $[Fe/H] = .3, -.3, -1.3$ and -2.3 with a helium abundance of 30%. The uncertainties in the integrated model colours are about 0.15 mag. in $B_J - K$ and 0.05 mag. in $J - K$.

The predicted $B_J - K$ and $J - K$ colours are listed in Table 4.3 (all colours

are in the Johnson system). The low metallicity models ($[Fe/H] < -.30$) cannot be calculated for ages less than 7 Gyrs because the mass tracks used to construct the isochrones do not extend beyond the base on the giant branch. Since the isochrones do not have full giant branches, the integrated colours corresponding to these small ages cannot be calculated. Extrapolation of the isochrones to a few Gyrs is possible but introduces further uncertainties to the models. The present model has been compared with the Frogel et al (1980) model and reasonable agreement is found.

Table 4.3

Stellar Synthesis Models

	$J-K$ $(X=-1.00)$				B_J-K $(X=-1.00)$			
$AGE/[Fe/H]$ (Gyr)	.3	−.3	−1.3	−2.3	.3	−.3	−1.3	−2.3
1		.76				2.59		
2	.92	.79			3.56	2.86		
3	.93	.80			3.80	3.01		
5	.96	.81			4.08	3.17		
7	.98	.81	.67	.59	4.24	3.28	2.61	2.28
10	.98	.83	.69	.60	4.33	3.38	2.76	2.41
13	.99	.84	.69	.61	4.40	3.45	2.85	2.50
16	.99	.85	.70	.62	4.46	3.52	2.90	2.56
20	1.00	.86	.71	.62	4.54	3.59	2.97	2.62
	$X=1.35$				$X=1.35$			
1		.71				2.35		
2	.87	.74			3.37	2.70		
3	.92	.77			3.66	2.89		
5	.95	.80			3.98	3.12		
7	.99	.82	.69	.61	4.18	3.26	2.64	2.33
10	.98	.84	.72	.63	4.27	3.40	2.82	2.48
13	1.00	.86	.74	.65	4.39	3.49	2.93	2.59
16	.99	.87	.75	.67	4.45	3.57	3.01	2.66
20	1.01	.89	.77	.68	4.56	3.67	3.10	2.74
	$X=3.00$				$X=3.00$			
1		.89				2.80		
2	1.14	.93			4.03	3.14		
3	1.21	.96			4.38	3.35		
5	1.19	.99			4.58	3.60		
7	1.28	1.02	.92	.84	4.90	3.78	3.18	2.86
10	1.10	1.06	.98	.86	4.77	3.94	3.40	2.99
13	1.16	1.08	1.01	.87	4.95	4.05	3.54	3.11
16	1.10	1.09	1.01	.89	4.97	4.13	3.61	3.19
20	1.16	1.10	1.07	.92	5.14	4.22	3.75	3.27

a) E-SO Galaxies

The models are compared with the E-SOs' colours on the $(B_J - K) - (J - K)$ plane (Figure 4.5). It is clear that a 13 Gyr model with a Salpeter initial mass function ($X = 1.35$) reproduces the infrared and optical–ir colours of early–type galaxies reasonably well.

The main conclusion from Figure 4.5 is that a single parameter (i.e. mean giant branch metallicity) is sufficient to explain the variation seen in the $B_J - K$ and $J - K$ colours of E-SO galaxies.

Frogel, Persson and Cohen (1980) show that constant age models with $X = 1.35$ and $X = 1$ reproduce the CO and H_2O indices of E-SOs and globular clusters fairly closely but are unable to predict the optical and optical–ir colour indices of early type galaxies. They attribute this to the existence of a cool, red population (i.e. AGB stars above the first giant branch tip) in E-SOs, not present in globulars and the models. Until the appropriate luminosity function for AGB stars is found and their evolution across the HR diagram is clearly understood, one cannot accurately model the infrared colours of E-SO galaxies.

The dwarf ellipticals are also shown on Figure 4.5. They do not produce a one parameter (metallicity) sequence with the luminous E-SOs and are more consistent with a steeper initial mass function (dwarf dominated) and appear to be extremely metal deficient. Employing models with younger ages does not produce a significantly better fit to the dwarf ellipticals.

b) Spiral Galaxies

In constructing evolutionary models for spiral galaxies one encounters a larger number of free parameters. Amongst them are **(1)** the IMF for star formation; **(2)** the star formation rate; **(3)** the age of the galaxy; **(4)** the metallicity of the interstellar medium; **(5)** the rate of stellar mass loss. The situation is further complicated by the fact that some of these parameters are correlated. This suggests that any interpretation of the spiral C–L relation will be highly model dependent (Tully et al 1982; Bothun et al 1984).

Stellar synthesis models from Table 4.3 are superposed on the AARS spirals in Figure 4.6 to disentangle the effects of age and metallicity in these galaxies. The sensitivity of $B_J - K$ colours to age variations is clear from this diagram. At a given metallicity a variation in age from 3 to 20 Gyrs changes $J - K$ colour by only 0.15 mag. whereas $B_J - K$ colour changes by as much as 0.90 mag.

For galaxies with $B_J - K > 3.5$ mag. the slope of the spirals' $(B_J - K) - (J - K)$ relation is relatively flat and the data are consistent with a metal rich model with $X = 1.35$. These galaxies are bulge dominated and their integrated light mainly consists of old population.

In the blue part of the diagram ($B_J - K < 3.5$ mag.) the constant metallicity and constant age lines are parallel, making it difficult to separate the effects of age and metallicity for these galaxies. The giant dominated models with $X = 1.35$ are distinctly different from the data in this region. However, models

Figure 4.5

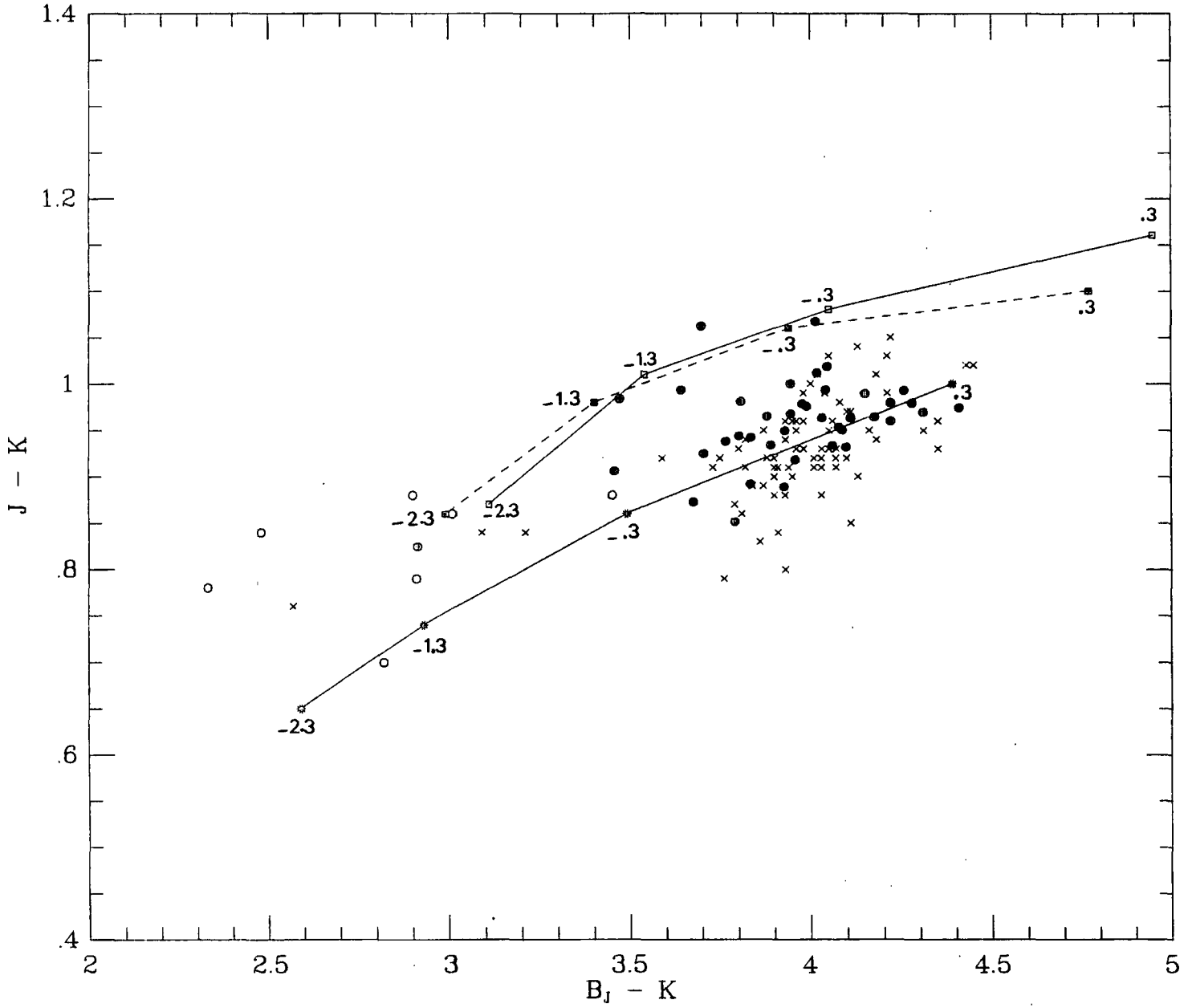

Figure 4.6

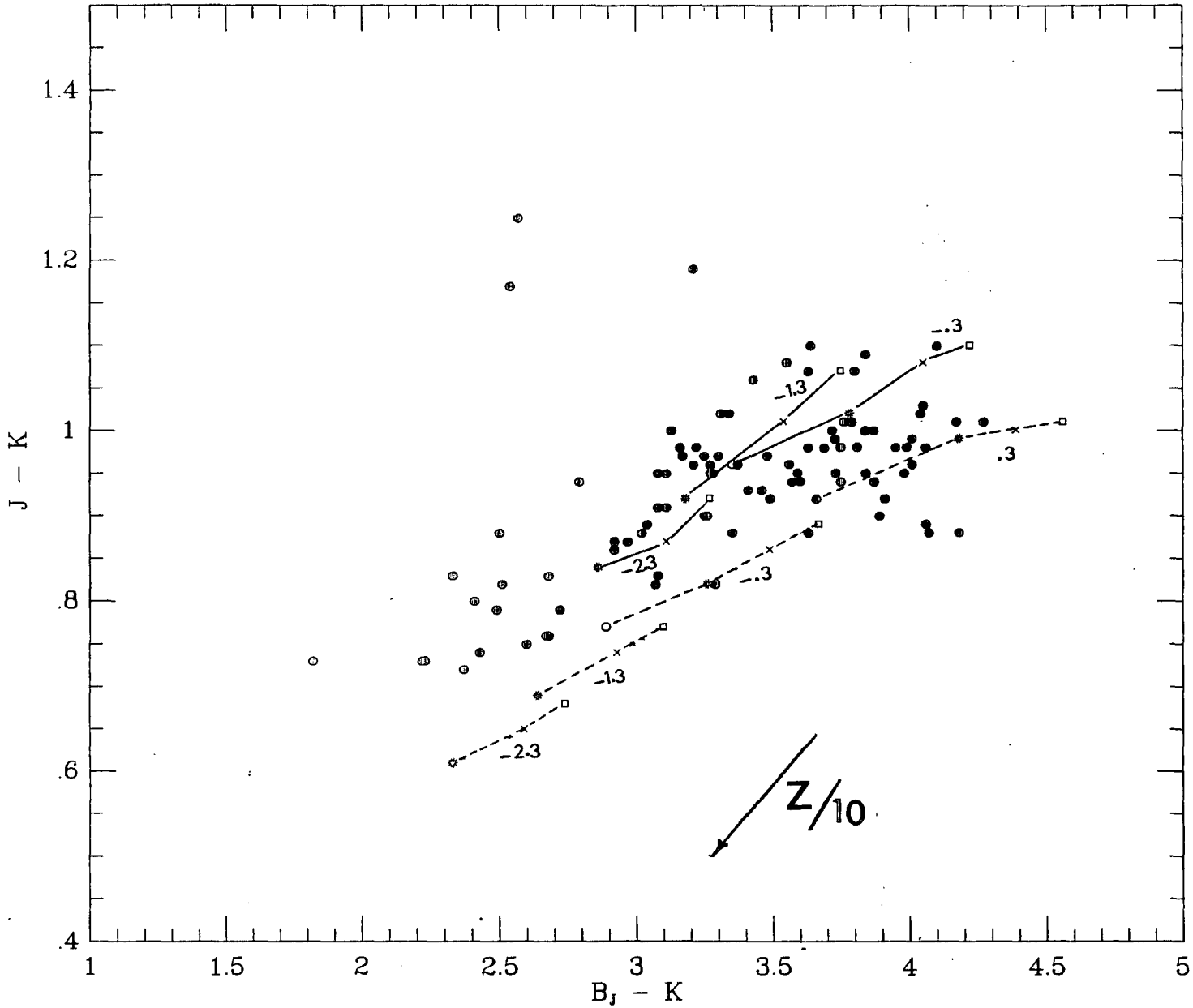

with a steeper initial mass function slope ($X = 3$) are more consistent due to a substantial contribution from dwarf stars to the optical–ir colours of blue spirals. Therefore, a trend towards a different IMF would explain the behaviour of spiral galaxies over the whole range covered by their $B_J - K$ colours.

The metallicity vector from the M31 globular clusters (Frogel et al 1980; Sitko 1984) is also drawn in Figure 4.6. Its length is found from the metallicity calibration of Aaronson et al (1978) and corresponds to a change in metallicity of a factor of 10. The slope of the blue spirals in the $(B_J - K) - (J - K)$ plane is close to that of the globulars which is caused by a metallicity variation. The $B_J - K$ colours of these galaxies change by 0.80 mag. over a range of 0.20 mag. in $J - K$. Therefore one could propose that a variation in metallicity is also responsible for the change in $B_J - K$ colours of blue spirals ($B_J - K < 3.5$ mag.) with different masses.

In summary, a single IMF cannot explain the behaviour of spirals on the $(B_J - K) - (J - K)$ plane. Red galaxies ($B_J - K > 3.5$ mag.) are more consistent with a giant dominated (shallow IMF), constant metallicity ($[Fe/H] = 0.3$) and varying age model. The contribution from the disk light to the integrated colours of these galaxies is small. Low luminosity spirals fit the model with a steeper IMF ($X = 3.00$). Since star formation alone cannot produce the trend for blue spirals on the optical–ir C–L diagram (Tully, Mould and Aaronson 1982), a variation in metallicity and/or age may also be needed to model properly the optical–ir C–L relation for these galaxies.

4.3 Intrinsic Scatter in the C–L Relations

It is important to compare the scatter in the colours at a constant luminosity with the estimated observational errors to determine if the dispersion in the C–L diagrams is intrinsic, or whether it could be reduced by obtaining more accurate observations. A knowledge of the intrinsic dispersion in the C–L diagrams is also of value in assessing the usefulness of the C–L relation as a distance indicator.

The root mean–square colour residuals at a constant luminosity have been calculated for the AARS E-SO and spiral samples and are listed in Table 4.4, together with the estimated observational errors from Chapter 2. The scatter in the $(J - K) - M_K$ and $(J - H) - M_K$ diagrams for both morphological types is of the same order as the observational errors indicating that the cosmic scatter in the infrared colours of galaxies is quite small. However, for the AARS spiral galaxies in $B_J - K$, and to a lesser extent for the E-SOs, the observed scatter exceeds that expected. For the spirals this discrepancy is more than a factor of 3, with an excess $\sigma = \left[\sigma^2_{rms}(B_J - K) - \sigma^2_{obs}(B_J - K)\right]^{1/2}$ of 0.37 mag. It might be argued that the observational errors in the B_J photometry are underestimated or that there are other systematic effects. I will discuss these possibilities further below. However, even if one attributes all of the scatter in $B_J - K$ colours of E-SOs to such effects, there remains an excess of 0.27 mag. in those of the spirals. I now consider various sources which could produce the large scatter around the spiral C–L relations.

Table 4.4

Mean colour residuals from the C–L relations.

TYPE	$\sigma_{res}(J-K)$	$\sigma_{res}(J-H)$	$\sigma_{res}(B_J-K)$	N
E-SO	±0.07	±0.06	±0.27	39
Spirals	±0.08	±0.05	±0.38	95
	$\sigma_{obs}(J-K)$	$\sigma_{obs}(J-H)$	$\sigma_{obs}(B_J-K)$	
	±0.04	±0.04	±0.10	

It is clear from the extinction vectors drawn in Figures 4.1 that Galactic absorption could have a significant effect on the dispersion in the optical–ir C–L diagram. All the three fields in this investigation are at $|b| > 48°$ but estimates of the reddening at such high Galactic latitudes are sometimes found to be significant (Couch 1982). To check this I have binned the data by field and tested the mean C–L relations for systematic effects. I find that the variation in the mean $B_J - K$ colours (corrected to a fixed M_K) from field–to–field is approximately 0.10 mag. Moreover, the mean scatter is similar in each field. Some of this offset could be due to zero–point uncertainties but these are unlikely to exceed 0.05 mag. (Peterson et al 1986). Thus whilst differential Galactic reddening might be responsible for some of the dispersion in the $(B_J - K) - M_K$ relation (say $\sim 0.05-0.10$ mag.) it seems unlikely to be a major factor in producing the excess scatter.

If the scatter were due to systematic errors in the corrections for internal reddening, then one would also expect to find some correlation of the C-L residuals with inclination, but none is seen. A similar test may also be conducted to eliminate the possibility of serious systematic errors in the corrections for residual colour gradients. Because the $(B_J - K) - M_K$ relation has a slope of 0.25, errors of 0.2 mag. in determining K_0, (c.f. Chapter 2), lead to a scatter in $B_J - K$ at fixed M_K of only 0.05 mag.

The possibility of increasing the scatter by mixing different morphological types in the spirals' C–L plane was examined by calculating the root mean–square colour residuals for individual types separately. No significant difference was found between the root mean–square values of different types of spirals around their combined $(B_J - K) - M_K$ relation.

It is likely that the various possibilities considered above co–add to give the observed result (e.g. for the E-SOs). For this reason more accurate measurements would certainly be worthwhile. However, it seems very likely that there is additional intrinsic scatter in the spiral relations due to variations in colour over and above the C–L relation. Much of this variation might be understood in terms of changes in the star formation rate at a fixed metallicity and also variations in B/D ratios amongst the spirals (see Chapter 5 for more details).

The fact that the intrinsic scatter in the *infrared* C–L relation is negligible, suggests that the variation in metallicity at a constant luminosity amongst the

galaxies is small and cannot be considered as a second parameter in their optical–ir C–L relation. Moreover, if there were a correlation between individual galaxy $B_J - J$ and $J - K$ colour residuals (I use $B_J - J$ colours instead of $B_J - K$ to avoid a false correlation with $J - K$), one would expect an external parameter related to the infrared colours to control the intrinsic scatter in the optical and optical–ir C–L relations. No such relation is found for the E-SOs or spirals in this sample. Taking the slope of the $(J - K)$–metallicity relation from Aaronson et al (1978) and an estimated observational error of 0.04 mag. in $J - K$ colours, it can be predicted that the variation in metallicity (at a given M_K) amongst the galaxies must be more than a factor of two to be observable in $J - K$ colours.

Griersmith (1980b) finds a relatively large cosmic scatter in the $(B-V)-M_V$ and $(U - V) - M_V$ relations for bulges of early type spirals. He considered variations in bulge–to–disk ratios as a dominant second parameter, but did not find any correlation between bulge–to–disk ratios and colours of galaxies in his sample. The infrared study of spirals in this section and the results from Griersmith et al (1982) exclude any possibility of metallicity being a dominant parameter. The presence of blue horizontal branch stars (McClure, Cowley and Crampton 1980) or the existence of a population of young stars with an age of $\sim$ 1 Gyr (O'Connell 1983) in the bulges of some spirals, not present in the others, could cause the variation in their optical colours at a constant luminosity.

Although this increased scatter may be a limiting factor in the use of the spirals optical–ir C–L relation for determining the distances of individual 'field' galaxies, a potentially important application remains in the determination of relative distance moduli for clusters of galaxies. Here improved statistics due to large samples offset the scatter. The integrity of this approach rests upon the assumed environmental independence of the C–L relations, which will be addressed in the following chapter.

4.4 Conclusions

In this chapter the infrared and optical–ir colours for the AARS galaxies are analysed in conjunction with further published data for 'field' E-SOs. The C–L relations have been studied for two broadly defined morphological types and reveal the following:

1. There is a statistically good evidence for a C–L relation for E-SOs in optical–ir and infrared colours. The slopes seen in these relations support the contention that metallicity is the driving factor in determining galaxy colours at all wavelengths studied. The mean metallicity of old giants varies by a factor $\sim$ 10 across the luminosity range of the sample. The present data do not support a simple picture of the type proposed by Bothun et al (1984) that varying amounts of blue horizontal branch stars produce the optical portion of the optical–ir C–L relation of E-SOs.

2. The slope of the spiral C–L relations is considerably steeper than that seen for the E-SOs suggesting a much more effective correlation between enrichment and luminosity. The variation in the mean metallicity of the old disk population is larger (by a factor of 4) than that of the spheroidal systems.

3. A trend is apparent between the residuals around the infrared surface brightness $\mu_K - M_K$ and $(B_J - K) - M_K$ relations of the AARS spirals. Variation in B/D ratios amongst the spirals is shown to be responsible for the trend. Correcting the colours of spirals for this surface brightness effect reduces the root mean–square scatter in their optical–ir C–L relation from 0.40 mag. to 0.31 mag.

4. A comparison with the stellar synthesis models reveals that a single parameter (metallicity) is sufficient to explain the variation in the infrared and optical–ir colours of E-SO galaxies.

   However, a change in the slope of the IMF is needed for the spirals to produce their $B_J - K$ colours over their observed range. Red spirals ($B_J - K > 3.5$ mag.) are more consistent with a giant dominated, constant metallicity and varying age model. However, a variation in both metallicity and age is necessary to satisfactorily model the spirals with $B_J - K < 3.5$ mag. Since age and metallicity for these galaxies produce similar trends on the $(B_J - K) - (J - K)$ plane it is not straightforward to disentangle these effects by using infrared and optical–ir colour indices alone.

5. The intrinsic scatter in the infrared C–L relations appear to be small. This implies a negligible variation in metallicity at a fixed absolute magnitude amongst the galaxies. In the optical–ir however, a significant intrinsic scatter is found around the C–L relations for spirals and to a lesser extent for E-SOs. Variations in B/D ratios and residual star formation amongst the spirals are considered to be the likeliest explanations for this effect.

CHAPTER V

The Colour–Luminosity Relation as a Distance Indicator

5.1 E-SO C–L Relation as a Distance Indicator

5.1.1 Introduction

The potential of the E-SO C–L relation as a distance indicator relies to a large extent on its universality. Visvanathan and Sandage (1977) have argued that the optical C–L relations are the same for early–type galaxies in clusters of different richness and Bautz–Morgan type. However, Aaronson et al (1981) found that the relative distance moduli between the Virgo and Coma clusters, derived from the $U-V$ and $V-K$ colours of their E-SO galaxies, differ by almost 1 magnitude. They attributed this to differences in the infrared energy distributions between the two clusters and proposed that a population of cool old stars exists in the Virgo E-SOs which is not present in the Coma galaxies. This implies that optical–ir C–L relations do not have a universal absolute zero–point and that E-SO galaxies have had different evolutionary histories depending perhaps on their environment.

In the following section I examine the Aaronson et al (1981) sample of E-SO galaxies. Using results from the last chapter I then investigate the usefulness of the infrared C–L relation of E-SOs for determining extragalactic distances.

5.1.2 Universality of the E-SO Infrared C–L Relations

Figure 3 of Aaronson et al (1981) shows that the deviation of the Coma cluster E-SOs from the mean line on the UVK plane becomes more pronounced at $V - K < 2.90$ mag. where there are no Virgo galaxies. The six SO galaxies in the Coma cluster, in this part of the diagram, are all identified from Rood and Baum's (1967) sample with available optical photometry from Sandage (1972). If these galaxies were anomalous in some way, they could conceivably bias the C–L relation in the Coma cluster and produce the difference found by Aaronson et al.

For example, if one removes these six galaxies from the Coma sample and re–calculate the relative distances between the two clusters, the difference between the relative distances from $U - V$ and $V - K$ colours reduces from 0.90 mag. to 0.50 mag. Although the two moduli come into closer agreement, the difference is still significant.

Next I examine the possibility that uncertainty in the diameters of the Coma E-SO galaxies could produce Aaronson et al's result. These diameters were uncertain and came from a variety of sources. To check this I used a uniform set of Coma diameters provided by Dr. N. Metcalfe (private communication). These were measured from PDS scans of Palomar Schmidt plates. However, no substantial difference in the result was found.

If the zero–point difference between the optical–ir C–L relations of the Virgo and Coma clusters is due to a cool stellar population, as proposed by Aaronson et al, it should present itself more strongly in the infrared C–L relations. To study this point I now consider the $(J - K) - K$ diagrams.

Galaxies which are members of these clusters are taken directly from Tables 1 and 2 of Aaronson et al (1981). Only those objects with available JHK magnitudes from Persson et al (1979) are used. This reduces the number of galaxies in Virgo from 31 to 29 and in Coma from 22 to 20. All the colours and magnitudes are reduced to the AARS system. The $(J - K) - K$ diagrams for the Virgo and Coma clusters are presented in Figure 5.1. Both colours and magnitudes are taken as independent variables and their corresponding regressions are listed in Table 5.1. One galaxy in Coma (RB 37) has a $J - K$ colour which is 3σ deviant from the mean line and is excluded from the solution.

Figure 5.1

$(J-K)-K$ for the Virgo (•) and Coma (○) cluster E-SOs with their corresponding least-square regressions. The faint deviant galaxy in the Coma cluster (RB 37) is not included in the fit.

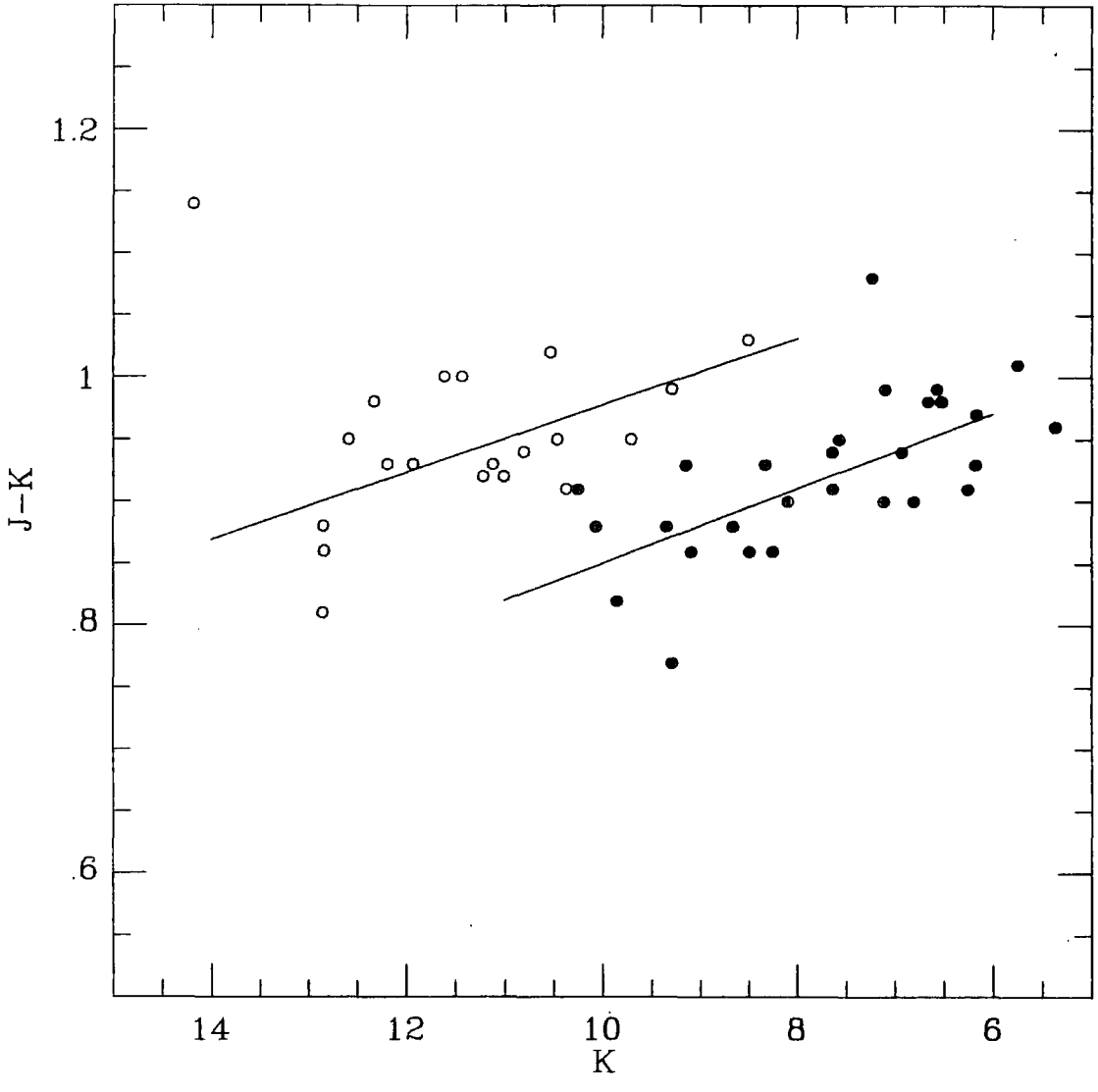

Table 5.1

Colour–Luminosity Relations for the Virgo and Coma Clusters

$$(J-K) = A + B(K-11)$$

Cluster	A	$-B$	r	$r.m.s.$	N
Virgo	0.82 ±.02	0.030 ±.007	−0.66	0.05	29
Coma	0.95 ±.01	0.027 ±.009	−0.61	0.04	19

$$K = A + B(J-K)$$

Cluster	A	$-B$	r	$r.m.s.$	N
Virgo	20.87 ±.31	14.27 ±3.16	−0.66	0.99	29
Coma	24.13 ±.35	13.68 ±4.36	−0.61	0.97	19

The slopes of the $(J-K)-K$ relations in Virgo, Coma and the AARS (Table 4.1) are very similar. The 'field' E-SO galaxies from the literature however, define a flatter slope (-0.014 ± 0.003) than both the AARS and cluster samples when a linear Hubble flow is assumed. This was investigated by re–analysing the literature sample, incorporating the Aaronson et al (1986) model for the Local group motion, but no significant change was found. Of course, the slopes of the AARS and cluster C–L relations are not affected by these Local group motions. The difference between the slopes is therefore more likely to be due to photometric errors in the literature galaxies.

Using the $(J-K)-K$ relation of Virgo and the $J-K$ colours of galaxies in Coma I find a relative distance modulus of $3.81 \pm .23$ mag. between the two clusters, compared to a value of $4.17 \pm .08$ mag. derived from the ratio of their redshifts assuming no infall velocity for the Local group towards Virgo. Taking the currently popular infall velocity of 240 Km/sec (Yahil 1986; see also Davis and Peebles 1983) gives a value of $3.71 \pm .08$ mag. which can be reconciled with the results from $(J-K)-K$ relations at the 1σ level. Therefore, one is led to the conclusion that there is little evidence, as yet, for any environmental dependence in the infrared C–L relations and the Aaronson et al (1981) result remains a puzzle. Infrared observations of more galaxies in the Coma cluster and other rich clusters are currently in progress to settle this important question.

It was shown in the last chapter that the intrinsic scatter in the infrared C–L relations for all morphological types is negligible. This is a simple demonstration of the fact that a colour such as $J-K$ is largely unaffected by residual amounts of star formation, internal reddening, population differences and colour gradients- all problems plaguing the optical indicators. These points combined with the apparent universality of the $(J-K)-K$ relation discussed above, support the use of infrared colours as potential distance indicators. However, the large slope found for the $(J-K)-K$ relation (taking $J-K$ as the independent variable) tends to limit its usefulness in this context. For example, if one measures $J-K$ colours with an accuracy of 0.04 mag., distance moduli can only be determined to $\pm$0.00 mag. This is, however, of the same order as the accuracy in the well–used optical C–L relations (e.g. $(U-V)-M_V$). It is therefore worthwhile to consider the application of high precision $J-K$ photometry to distance scale work in clusters.

5.2 The Spiral C–L Relation as a Distance Indicator

5.2.1 Introduction

It has been realised for sometime that the slope of the magnitude/HI velocity width relation (Tully–Fisher relation; hereafter TF) is wavelength dependent, increasing from optical to infrared wavelengths (Bottinelli et al 1980; Tully et al 1982). This in turn implies that a relation must exist between optical–ir colours (e.g. $B-H$) and the mass (luminosity) of spiral galaxies, with more massive galaxies being redder (Wyse 1982; Visvanathan 1983). The $(B-H)-M_H$ relation can therefore provide a new technique for estimating distances to spiral galaxies. However, before any attempt to use this relation as a distance indicator, the questions concerning its type–dependence, universality and cosmic scatter must be properly answered.

In an analysis of spiral galaxies, Roberts (1978) has shown that the TF relation in optical wavebands is type–dependent. His conclusion was challenged by de Vaucouleurs et al (1982) who suggested that this is merely a regression effect (due to the use of the regression of $< \log V >$ on $< M >$ and the presence of large errors in M) and by Aaronson, Huchra and Mould (1979) who considered the magnitude limited nature of his sample as the main cause. Robert's result received support from Rubin et al (1980), who suggested that the slope of the TF relation in the blue for each morphological type is almost equal to the slope found in the infrared and that the smaller slope found previously in the blue was due to a type–dependence of the TF relation and not a wavelength–dependence. Furthermore, any type–dependence of the luminosity function (optical or infrared) could be reflected as a type–dependence of the slope of the TF relation. Aaronson and Mould (1983) have suggested recently that the blue TF relation is slightly type–dependent; however, they claim no type–dependence in the infrared. This can be understood if M/L_H is constant amongst the spirals and the infrared light is dominated by old giants. The type–dependence of the blue TF relation, if any, would transfer to a type–dependence of the slope of the $(B-H)-M_H$ relation.

In a study of optical–ir colours of a sample of spiral galaxies in seven nearby cluters Bothun et al (1985a) showed that the zero–point of $(B-H)-M_H$ relation varies amongst the clusters and hence is not universal. This result however, relies on the implicit assumption that the $(B-H)-M_H$ relation is not type–dependent. Since the galaxies in Bothun et al (1985a) sample have no accurate type classification one cannot test the validity of this assumption. Moreover, it appears from their data that the zero–point of the $(B-H)-M_H$ relation is dependent upon cluster redshift, possibly because of a bias in their sample. Therefore, prior to any study of the universality of optical-ir C-L relation one should examine its type–dependence.

The potential of the $(B-H)-M_H$ relation as a distance indicator depends also upon its intrinsic scatter. It was found in the last chapter that the cosmic scatter in the optical–ir C–L relation of spirals is significant and a second parameter was proposed. Regarding the scatter in the $(B-H)-M_H$ plane, Bothun et al (1985a) claimed that it would not be possible to find distances from this relation with an accuracy better than 0.70 mag.

In the rest of this chapter I primarily analyse the precision of the optical–ir C–L relation as a distance indicator. In the next section I present a large sample of nearby spiral galaxies with available optical and infrared magnitudes reduced to the AARS system. This is a complementary sample to the AARS in terms of morphological types. The type–dependence of the optical–ir C–L relation is then studied in section 5.2.3, where the need for a second parameter is discussed. Taking into account the type–dependence of the C–L relation I then investigate its universality in section 5.2.4. Finally I estimate the accuracy of distances derived from the C–L relation by comparing them with those using the infrared TF relation in section 5.2.5.

5.2.2 Sample Selection and Data Reduction

In order to study the morphological type–dependence of the optical–ir C–L relation, a sample of spiral galaxies from the literature has been compiled. The catalogue of 21 cm velocities (Fisher and Tully 1981) was searched for galaxies in common with the infrared catalogue of Aaronson et al (1982a). A total number of 198 intermediate to late–type spirals was selected with total blue magnitudes, redshifts and morphological types from the HI catalogue and the infrared $H_{-0.5}$ magnitudes taken from Aaronson et al (1982a).

To form the optical–ir colours one needs to find both magnitudes over the same aperture. The type–dependent growth curves from the RC2 were used to convert B_{TOT} to B at $\log(A/D_0) = -0.5$. The corrections were found to vary from 0.8 mag. for Sa-Sab to 1.25 mag. for Sdm and later–type spirals. The $B-H$ colours at $\log(A/D_0) = -0.5$ are reduced to $\log(A/D_0) = 0.0$ using the colour gradient from chapter 2. To convert the $B-H$ colours to B_J-H, which is the AARS scale, the $B-V$ colours were taken from the RC2. A relation was then established between $B-H$ and B_J-H colours and was employed to find B_J-H for those galaxies with no $B-V$ colours. The accuracy of the reduced B_J-H colours of literature spirals is estimated to be about 0.20 mag. The infrared magnitudes of these galaxies were also reduced to $\log(A/D_0) = 0.00$ using the RC2 growth curve and the reduced magnitudes then corrected for optical–ir colour gradients.

The compiled sample of spirals is listed in Table 5.2. Column 1 gives the name of the galaxy. Columns 2 and 3 present the H magnitudes and B_J-H colours at $\log(A/D_0) = 0.00$. Columns 4, 5 and 6 list the redshifts, log of the B–band isophotal diameters (at 25 mag./arcsec.^{2}) in units of 0.1 arcmin. and morphological types respectively. The group assignments are given in column 7. The group memberships for all the galaxies are taken directly from Aaronson et al (1982a).

The spirals listed in Table 5.2 are all HI rich and hence the sample is deficient in objects with large B/D ratios (e.g. early–type spirals). Combined with the AARS, a sufficiently large number of galaxies in each morphological type bin will become available to make a rigorous analysis of the dependence of the $(B_J-H)-M_H$ relation on B/D ratio and type.

Table 5.2

Compiled list of nearby spiral galaxies reduced to the AARS system.

Name	H_0	$B_J - H$	V	$\log(D_{25})$	Type	Group
N24	9.07	2.25	595	1.61	Sc	N24/N45
N45	8.79	2.31	511	1.87	Sdm	N24/N45
N100	10.29	2.14	1035	1.61	Scd	
N134	6.98	3.31	1572	1.79	Sbc	N134
N150	8.62	2.88	1601	1.56	Sb	N134
N247	6.87	1.96	190	2.20	Sd	Sculptor
U711	11.61	1.31	2088	1.44	Scd	
N493	10.14	2.32	2436	1.48	Scd	
N578	8.91	2.33	1622	1.64	Sc	
N613	7.30	3.35	1449	1.74	Sbc	
N701	9.38	3.16	1869	1.33	Sc	
N772	7.49	3.32	2605	1.81	Sb	
N779	8.21	2.93	1435	1.50	Sb	
N784	10.13	1.04	362	1.66	Sd	
N803	9.70	2.82	2214	1.45	Sc	
N891	6.34	3.03	712	2.01	Sb	N1023
N908	7.65	2.79	1466	1.67	Sc	
N918	9.33	3.06	1625	1.50	Sc	
N925	7.92	2.25	710	1.95	Sd	N1023
N949	9.22	2.83	774	1.41	Sb	N1023
N959	10.18	2.31	767	1.31	Sm	N1023
U2082	10.13	1.22	834	1.63	Sc	
N1003	9.27	1.95	794	1.66	Scd	N1023
N1035	9.57	2.52	1232	1.25	Sc	
N1055	7.48	3.34	1030	1.78	Sb	
N1090	9.34	2.64	2786	1.50	Sbc	
N1169	7.99	3.40	2564	1.66	Sb	
N1171	9.45	2.43	2906	1.45	Sc	
N1255	9.24	2.21	1600	1.57	Sbc	Eridanus
N1253	9.28	2.70	1696	1.62	Scd	
N1292	9.77	2.35	1261	1.43	Sc	Eridanus
N1300	8.20	2.62	1502	1.77	Sbc	Eridanus
N1326	7.66	3.57	1221	1.57	Sa	Fornax
N1325	8.99	2.78	1503	1.56	Sbc	Eridanus
N1337	9.24	2.26	1199	1.71	Scd	
N1365	6.70	3.18	1492	1.93	Sb	Fornax
N1385	8.75	2.66	1390	1.44	Scd	Eridanus
N1406	8.79	2.66	931	1.45	Sbc	Fornax
N1421	9.03	1.64	2021	1.43	Sbc	
N1425	8.38	2.99	1376	1.66	Sb	Fornax
N1448	7.65	2.66	1000	1.76	Scd	
N1507	9.97	2.12	810	1.42	Sm	
N1560	8.49	2.20	164	1.86	Sd	M81?
U3137	10.80	2.07	1193	1.46	Sb	
N1744	9.12	2.30	562	1.79	Sd	

N1784	8.54	3.43	2182	1.59	Sc	
N1792	7.66	2.81	1003	1.54	Sbc	
N1964	7.63	3.01	1480	1.72	Sb	
N2090	7.94	3.29	707	1.59	Sc	
N2280	7.95	2.76	1651	1.73	Scd	
U3580	9.92	1.69	1356	1.57	Sa	
U3691	10.65	1.28	2102	1.36	Scd	
N2357	9.73	2.49	2201	1.43	Sc	
N2336	8.01	2.58	2386	1.79	Sbc	N2336
N2403	5.72	2.67	261	2.21	Scd	M81
U4238	11.03	1.63	1714	1.34	Sd	
N2541	9.57	2.22	596	1.77	Scd	N2841
N2591	9.71	2.06	1509	1.37	Sc	
N2613	7.07	2.49	1411	1.80	Sb	
U4514	11.53	1.69	759	1.31	Sc	N2841
U4559	10.11	3.11	2027	1.33	Sab	
N2683	6.46	3.26	373	1.85	Sb	
N2701	10.27	2.30	2391	1.30	Sc	
N2770	9.83	1.47	1908	1.47	Sc	
N2835	8.30	2.14	620	1.78	Sc	
N2841	6.40	3.36	686	1.84	Sb	N2841
N2903	5.96	3.33	451	2.04	Sbc	
N3026	11.12	1.75	1431	1.29	Im	
N3027	10.20	2.02	1211	1.61	Sd	
N3079	7.45	2.62	1200	1.73	Sc	N3079/U5459
U5459	9.88	2.45	1184	1.52	Sc	N3079/U5459
N3153	10.82	2.14	2672	1.29	Scd	
N3198	8.03	2.43	686	1.84	Sc	N3184
N3225	10.81	2.07	2227	1.30	Sc	
N3264	11.22	2.02	1023	1.45	Sm	
N3319	9.67	1.83	754	1.77	Scd	N3184
N3359	8.58	2.21	1131	1.78	Sc	
N3365	10.30	1.62	810	1.52	Scd	N3521
N3432	9.34	1.69	600	1.65	Sm	N3184
N3443	11.64	2.13	1028	1.34	Sd	Leo
N3501	9.60	2.73	1040	1.41	Sc	Leo
N3510	10.73	1.86	664	1.43	Sm	
N3521	5.91	3.43	628	1.91	Sbc	N3521
N3549	9.43	2.45	2944	1.42	Sc	
N3600	10.21	1.43	740	1.49	Sa	
N3621	6.58	2.75	470	1.96	Sd	
N3623	6.26	3.38	692	1.89	Sa	Leo Triple
N3627	6.20	3.19	623	1.87	Sb	Leo Triple
N3628	6.47	2.65	734	2.03	Sb	Leo Triple
N3666	9.16	2.42	947	1.51	Sc	Leo
N3675	7.24	3.47	805	1.71	Sb	Ursa Major
N3705	8.05	3.12	891	1.62	Sab	Leo
N3717	7.53	3.33	1477	1.63	Sb	
N3726	8.20	2.65	914	1.75	Sc	Ursa Major
N3733	10.44	1.52	1278	1.60	Sc	Ursa Major

N3735	8.58	2.68	2853	1.47	Sc	
N3755	10.54	2.21	1575	1.44	Sc	
N3756	9.07	2.88	1382	1.58	Sbc	Ursa Major
N3782	10.99	1.96	793	1.19	Scd	Ursa Major
N3813	9.39	2.78	1474	1.29	Sb	Ursa Major
U6667	11.45	1.51	1051	1.38	Sc	Ursa Major
N3877	8.02	2.66	954	1.60	Sc	Ursa Major
N3893	8.11	2.75	1043	1.59	Sc	Ursa Major
N3917	9.31	2.14	1056	1.57	Scd	Ursa Major
U6818	12.04	1.92	857	1.25	Scd	Ursa Major
N3936	9.56	2.19	1789	1.46	Sb	
N3949	8.86	2.43	868	1.42	Sbc	Ursa Major
N3953	7.22	3.42	1139	1.76	Scd	Ursa Major
N3972	9.89	1.93	947	1.49	Sbc	Ursa Major
N3976	8.69	3.24	2381	1.49	Sb	
U6923	11.21	2.47	1172	1.25	Im	Ursa Major
N3992	7.38	3.10	1142	1.83	Sbc	Ursa Major
N4010	9.75	2.11	968	1.47	Scd	Ursa Major
N4013	8.05	3.34	883	1.57	Sb	Ursa Major
N4062	8.62	2.98	764	1.55	Sc	Coma I
N4094	9.56	2.34	1232	1.53	Sc	
N4096	8.18	2.38	644	1.69	Sc	Ursa Major
N4100	8.27	2.81	1153	1.62	Sbc	Ursa Major
N4116	9.79	2.62	1177	1.53	Sdm	Virgo South
N4127	9.92	2.69	2006	1.32	Sbc	
N4142	11.35	2.22	1257	1.31	Sd	Ursa Major
N4144	9.59	1.52	331	1.63	Scd	
N4145	8.89	2.57	1048	1.73	Sd	Ursa Major
N4157	7.85	2.80	854	1.69	Sb	Ursa Major
N4178	9.28	2.32	285	1.61	Sdm	Virgo
N4183	9.94	1.95	987	1.55	Scd	Ursa Major
N4206	9.74	2.05	616	1.57	Sbc	Virgo
N4217	8.15	3.16	1098	1.63	Sb	Ursa Major
N4236	8.22	1.18	163	2.17	Sdm	M81
N4244	8.02	1.46	276	2.06	Scd	CVnI
N4258	5.51	2.97	521	2.18	Sbc	CVnI
N4359	10.60	1.90	1256	1.42	Sc	Coma I
N4414	7.15	3.64	723	1.51	Sc	Coma I
N4455	10.80	1.82	611	1.34	Sd	
N4498	10.03	2.22	1448	1.45	Scd	Virgo
N4501	6.64	3.45	2217	1.78	Sb	Virgo
U7699	10.81	1.43	539	1.46	Scd	
N4532	9.58	2.74	1909	1.37	Im	Virgo
N4535	7.77	2.82	1873	1.80	Sc	Virgo
N4545	10.13	2.32	2860	1.39	Sc	
N4559	7.61	2.51	810	1.94	Scd	Coma I
N4565	6.20	3.06	1213	2.06	Sb	Coma I
U7774	11.71	1.60	574	1.40	Sd	
N4592	9.69	1.78	954	1.54	Sdm	Virgo South
N4651	7.97	3.21	748	1.54	Sc	Virgo

N4654	8.06	2.93	978	1.63	Scd	Virgo
U7941	11.67	1.31	2445	1.50	Sdm	
N4713	9.71	2.36	560	1.41	Scd	Virgo South
N4725	6.56	3.37	1199	2.01	Sab	Coma I
N4758	10.72	2.25	1196	1.37	Sb	Virgo
N4808	9.23	3.00	668	1.35	Scd	Virgo South
N4826	5.60	3.64	394	1.92	Sab	CVnI
U8146	11.72	1.13	805	1.41	Sc	
N4939	8.45	2.49	2973	1.70	Sbc	
U8246	12.13	1.35	855	1.36	Scd	N5033
N5023	10.08	1.11	484	1.66	Sc	M51
N5033	6.82	3.41	931	1.96	Sc	N5033
N5055	5.70	3.44	575	2.04	Sbc	M51
N5161	8.51	2.86	2196	1.65	Sc	
N5170	7.70	2.82	1347	1.76	Sc	
N5204	9.44	2.19	346	1.63	Sm	M101
N5205	9.72	2.99	1940	1.48	Sc	
N5290	8.74	3.17	2673	1.44	Sb	N5371
N5300	9.70	2.56	1123	1.55	Sc	N5364
N5320	9.60	2.79	2709	1.48	Sc	N5371
N5348	10.93	1.88	1411	1.41	Sbc	N5364
N5486	11.55	2.33	1559	1.19	Sm	
N5496	10.43	1.43	1488	1.49	Sd	N5566
N5523	9.68	2.61	1099	1.53	Scd	
N5529	8.64	2.81	2971	1.62	Sc	
N5585	9.33	2.01	466	1.70	Sd	M101
N5630	11.02	2.05	2777	1.28	Sm	
N5690	9.12	2.69	1729	1.43	Sc	N5566
N5740	9.07	3.22	1558	1.43	Sb	N5566
N5792	7.72	3.83	1914	1.74	Sb	N5566
N5861	9.01	2.74	1821	1.44	Sc	
N5879	8.69	2.96	962	1.54	Sbc	N5866
U9764	11.77	2.47	2448	1.37	Sdm	
N5894	9.15	2.96	2679	1.36	Sm	
N5907	6.90	2.97	854	1.94	Sc	N5866
U9858	9.77	2.45	2774	1.48	Sbc	
N5951	10.44	1.94	1860	1.41	Sc	
U9977	10.74	1.98	1944	1.43	Sc	N6070
N6015	8.42	2.82	1048	1.65	Scd	
U10288	9.70	2.63	2099	1.56	Sc	N6070
N6118	8.71	2.91	1629	1.61	Scd	
N6255	11.18	1.45	1124	1.47	Scd	
N6339	10.39	2.24	2336	1.46	Sc	
N6368	9.14	2.72	2920	1.49	Sb	
N6395	10.77	1.33	1415	1.32	Scd	
U11093	9.50	2.62	2122	1.40	Scd	
N6689	9.74	2.00	750	1.49	Sd	
N6764	9.91	2.22	2691	1.37	Sb	
N6925	8.10	3.37	2847	1.52	Sbc	
U11651	10.12	2.60	1804	1.44	Sdm	

U11707	11.26	2.27	1187	1.52	Sdm	
N7184	8.01	3.18	2727	1.64	Sc	
N7307	10.52	1.41	2077	1.47	Sc	Grus
N7314	8.55	2.65	1499	1.59	Sbc	
N7320	10.52	2.35	1066	1.29	Sd	N7320/7331
N7331	5.84	3.80	1099	1.95	Sbc	N7320/7331
N7361	10.28	1.94	1306	1.42	Sc	
N7456	9.56	1.61	1205	1.65	Scd	Grus
N7462	9.63	1.98	1061	1.42	Sc	Grus
N7497	9.19	2.95	1945	1.59	Scd	
N7531	8.47	3.25	1568	1.45	Sbc	Grus
N7721	9.06	2.76	2148	1.45	Sc	
N7793	7.03	2.64	236	1.93	Sdm	Sculptor

5.2.3 Type–Dependence of the Optical–ir C–L Relations

In this section I combine the AARS and literature spirals from Table 5.2 to improve the distribution of galaxies over morphological types and to investigate the type–dependence of optical–ir C–L relation. Since only the infrared H magnitudes are available for the literature sample, the attention is restricted to $(B_J - H) - M_H$ relation.

Galaxies which are assigned to nearby groups and clusters in Table 5.2 have been removed from the literature sample. Absolute magnitudes of the remaining 'field' galaxies were calculated using their relative distances with respect to Virgo given in Aaronson et al (1982a) which are based on the infall model (case 3.1) from Aaronson et al (1982b). A distance modulus of 31.70 mag. is assumed for the Virgo cluster (Sandage and Tammann 1976). Applying the above criteria reduces the number of literature spirals to 87.

The galaxies are divided into four morphological classes: Sa-Sab, Sb-Sbc, Sc-Scd and Sd-Sdm. The $(B_J - H) - M_H$ relation for the combined AARS/literature sample is presented in Figure 5.2a and the linear regressions as a function of morphological type are given in Table 5.3. The early–type spirals (Sa-Sab) have a noticeably redder zero–point compared to later–types. This is most likely caused by a substantial contribution of their bulge light to their optical–ir colours. Assuming a linear Hubble flow instead of an infall model does not change this conclusion. It is also found that using the literature sample alone does not affect the results in Table 5.3. I now investigate the possibility of a second parameter being responsible for the scatter in the zero–point of the optical–ir C–L relation across the spirals sequence.

A relation was found in the last chapter between the infrared surface brightness (μ_K) and absolute magnitudes of the AARS spirals. It was also shown that the residuals about the $(B_J - K) - M_K$ and $\mu_K - M_K$ relations were correlated and that a variation in B/D ratios was thought to be responsible for this and for the scatter in the optical–ir colours of spirals at a given absolute magnitude. Since B/D ratio is also correlated with morphological type (Sandage 1961; Whitmore 1984) the analysis in chapter 4 may, in addition, be relevant to the type–dependence of the C–L relations and to the present discussion.

Employing the isophotal diameters and H magnitudes of the literature spirals (Table 5.2) I now calculate their infrared surface brightness (μ_H) and plot the $\mu_H - M_H$ diagram for the combined samples of the AARS and literature spirals in Figure 5.3. A least–squares solution gives

$$\mu_H = (0.39 \pm .03)\,(M_H + 23) + (20.55 \pm .06) \quad r.m.s. = .75 \; r = .65 \; N = 182 \quad (5.1)$$

The μ_H residuals around this relation and the $B_J - H$ colour residuals around the composite $(B_J - H) - M_H$ diagram are plotted in Figure 5.4a. The trend in the $\Delta\,(B_J - H) - \Delta\,\mu_H$ plane due to variation in B/D ratio is indicated by a solid line and suggests, again, that the correlation between the residuals (or strictly speaking, the scatter in optical–ir colours of spirals) is due to a variation in their B/D ratios. The residuals relation based on the AARS/literature spirals

is

$$\Delta\,(B_J - H) = (-0.35 \pm .04)\,\Delta\,(\mu_H) + (0.01 \pm .03)\ \ r.m.s. = .36\, r = -.59\, N = 182 \tag{5.2}$$

which agrees closely with that derived in chapter 4 from the AARS galaxies alone. Equation 5.2 can now be used to correct the $B_J - H$ colours for this surface brightness (B/D) effect. The corrected $(B_J - H)_c - M_H$ diagram is plotted in Figure 5.2b and the regression line for each morphological type is calculated and listed in Table 5.3. It is clear from Figures 5.2 and Table 5.3 that not only is the r.m.s. scatter significantly reduced but the type–dependence in the C–L zero point is largely removed.

Table 5.3

$(B_J - H) - M_H$ relation for different types of spirals

$$B_J - H = A + B(M_H + 23)$$

TYPE	A	$-B$	$r.m.s.$	r	N
Sa-Sab	$2.88 \pm .09$	$0.36 \pm .06$	0.42	−0.74	31
Sb-Sbc	$2.76 \pm .08$	$0.20 \pm .05$	0.43	−0.52	57
Sc-Scd	$2.57 \pm .05$	$0.33 \pm .03$	0.42	−0.80	78
Sd-Sdm	$2.59 \pm .13$	$0.31 \pm .06$	0.36	−0.83	16
Total	$2.65 \pm .03$	$0.31 \pm .02$	0.45	−0.75	182

$$(B_J - H)_c = A + B(M_H + 23)$$

Sa-Sab	$2.66 \pm .06$	$0.36 \pm .04$	0.28	−0.86	31
Sb-Sbc	$2.65 \pm .06$	$0.26 \pm .04$	0.35	−0.67	57
Sc-Scd	$2.64 \pm .04$	$0.35 \pm .02$	0.34	−0.86	78
Sd-Sdm	$2.70 \pm .14$	$0.28 \pm .06$	0.43	−0.76	16
Total	$2.64 \pm .03$	$0.31 \pm .02$	0.36	−0.82	182

The reduction in scatter and the type–independence of the spirals' $(B_J - H) - M_H$ relation in Figure 5.2b now support its application as a distance indicator. The integrity of this approach, however, rests on the universality of this relation which will be addressed in the following section.

Figure 5.2a

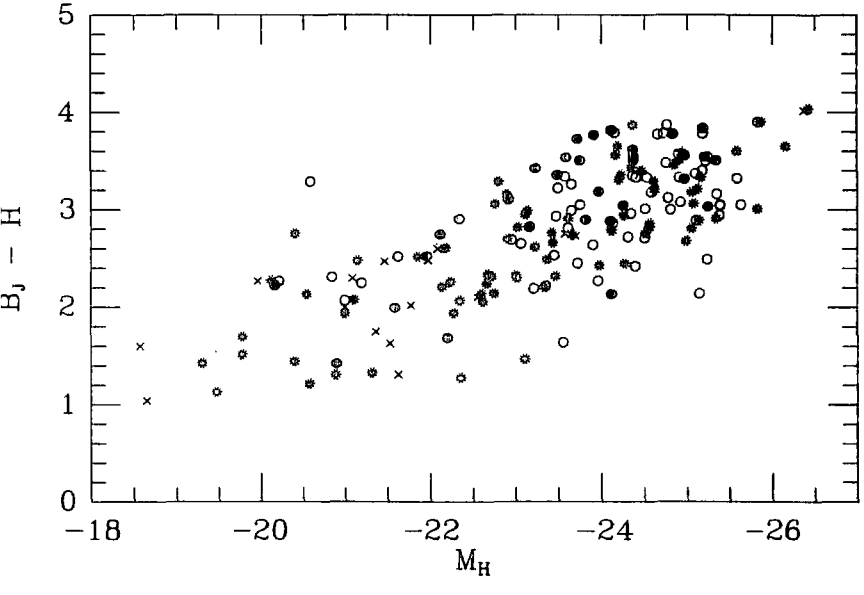

Figure 5.2b

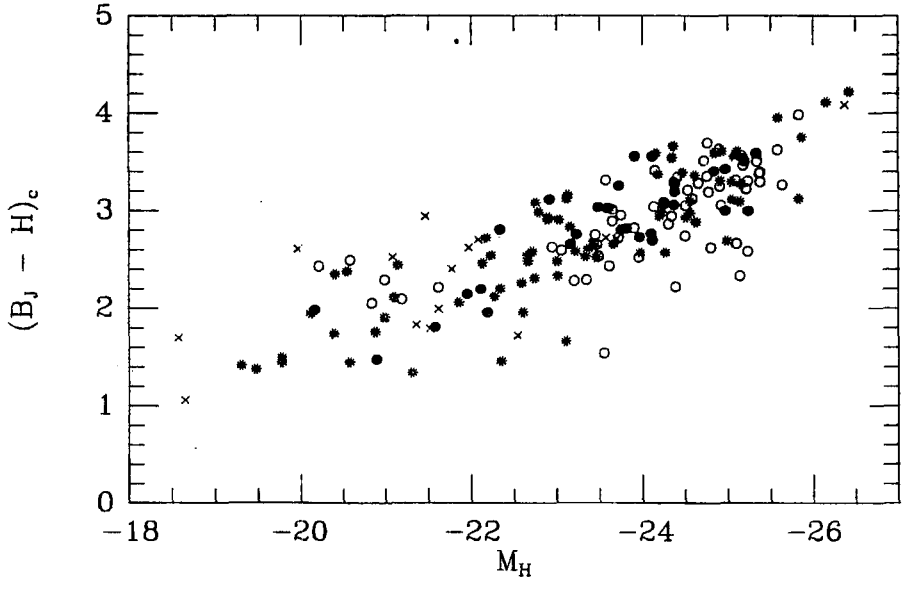

Figure 5.3

Infrared surface brightness–absolute magnitude diagram for the AARS/literature spirals (symbols as in Figure 5.2a).

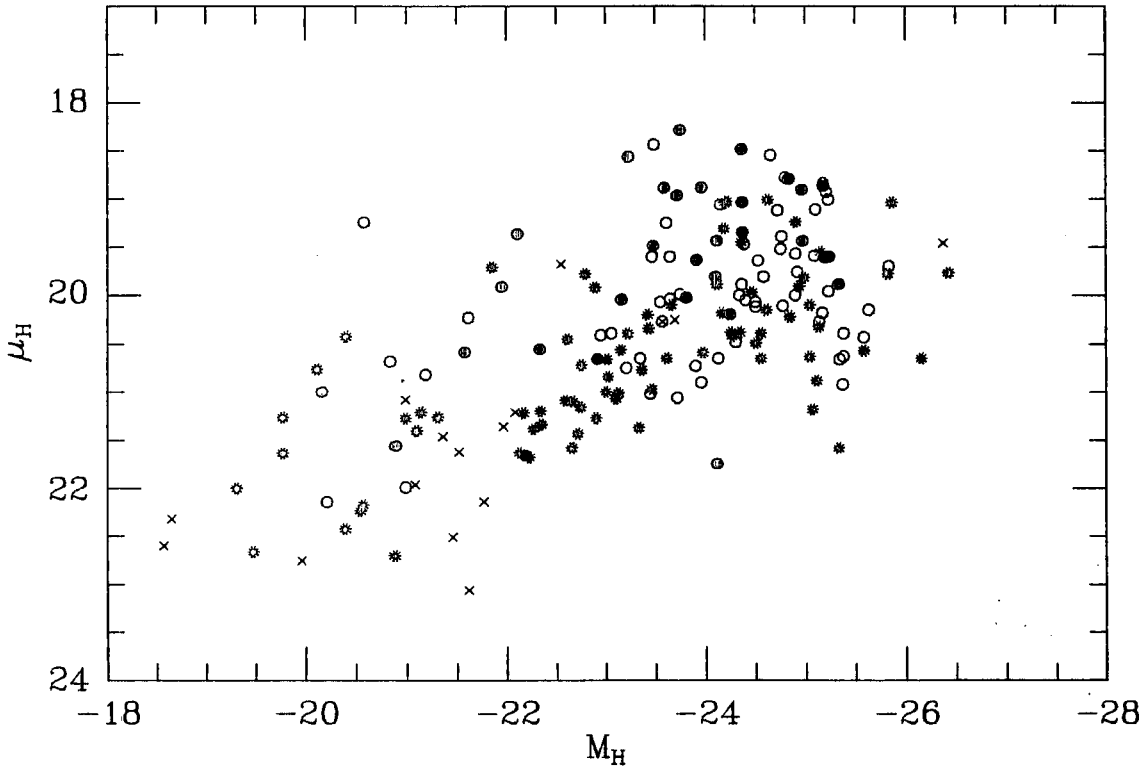

5.2.4 Universality of the Spiral Optical–ir C–L Relation

A tight correlation exists between 21 cm line width (ΔV) and the $B-H$ colours of spiral galaxies (Tully et al 1982). This relation is particularly useful for a study of environmental effects since both parameters are independent of distance (although the $B-H$ colours depend on distance through the K–corrections; the optical–ir K–corrections are considered to be well known- see chapter 3). The $(B-H)-\Delta V$ relation has been studied by Bothun et al (1985a) for a sample of 166 spirals in 7 nearby clusters and important differences were found in the zero–points between different clusters. It is not clear whether these differences arise from variations in the 21 cm line width (M/L variations) or from variations in $B-H$ colours at a fixed luminosity. Considering the environmental independence of infrared TF relation (Aaronson and Mould 1983) the implication is that there are type–dependences in the $(B-H)-M_H$ C–L relations.

Unfortunately, accurate morphological type classifications for Bothun et al's cluster sample are not available to examine this conjecture. In view of the success in the last section in removing the type–dependence of optical–ir C–L relations by correcting for surface brightness effects, I now investigate if this could reduce the scatter in the C–L zero–points within the cluster sample. I check first whether the same surface brightness–colour residual relation is present in this sample.

The $B-H$ colours for the cluster galaxies are taken from Bothun et al (1985c). The infrared H magnitudes, distance moduli, and optical isophotal diameters, however, have been taken from Aaronson et al (1986), since these data include corrections to a CCD based isophotal diameter system. The overlap between these two samples reduces the number of galaxies to 100. The infrared magnitudes at $\log(A/D_0) = -0.5$ are transformed to the AARS system by applying a mean correction of 0.75 mag. derived from the mean RC2 growth curve regardless of morphological type.

The surface brightness–colour residual diagram for the cluster sample is presented in Figure 5.4b and shows a similar trend to that for the AARS/literature galaxies. Using all the 7 clusters I find

$$\Delta\,(B_J-H) \sim -0.29\,\Delta\,\mu_H \quad r.m.s. = .29\ r = -.47\ N = 100 \qquad (5.3)$$

I now examine the scatter in the mean $B-H$ colour at fixed luminosity for each of Bothun et al's clusters with and without the surface brightness correction. The various relations required between M_H, $B-H$ and μ_H are taken from the total sample and the results are summarised in Table 5.4. The r.m.s. dispersion in the mean colour zero–points for the seven clusters before correction is 0.13 mag. compared with 0.09 mag. after. This indicates the degree to which environmental effects may still be present since the dispersion across the spiral sequence, as shown in Table 5.3, is smaller ($\sim$ 0.05 mag.) than that seen from cluster–to–cluster. Using the slope of the composite $(B_J-H)-M_H$ relation listed in Table 5.3 I estimate an r.m.s. error of the order of 0.28 mag. in the distance moduli derived from this improved optical–ir C–L relation.

Figure 5.4a

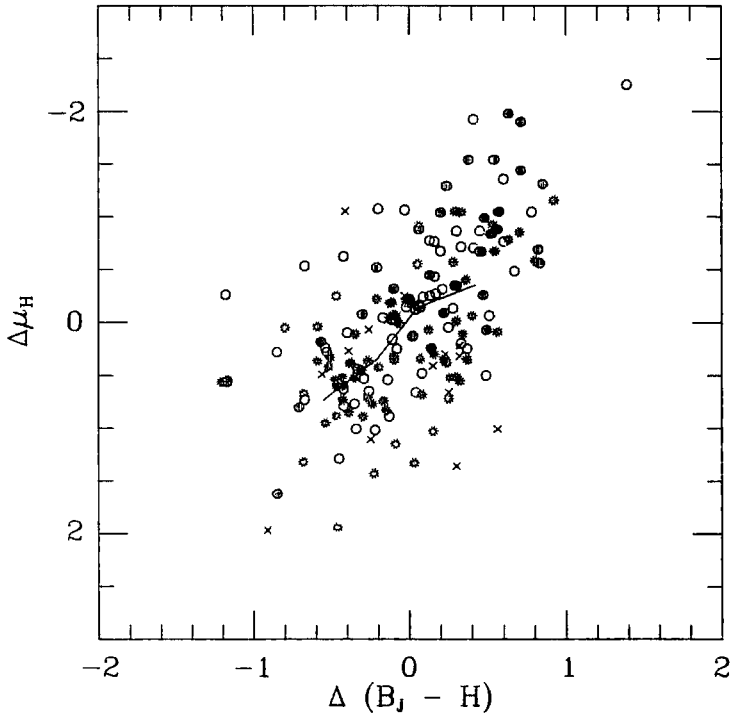

Figure 5.4b

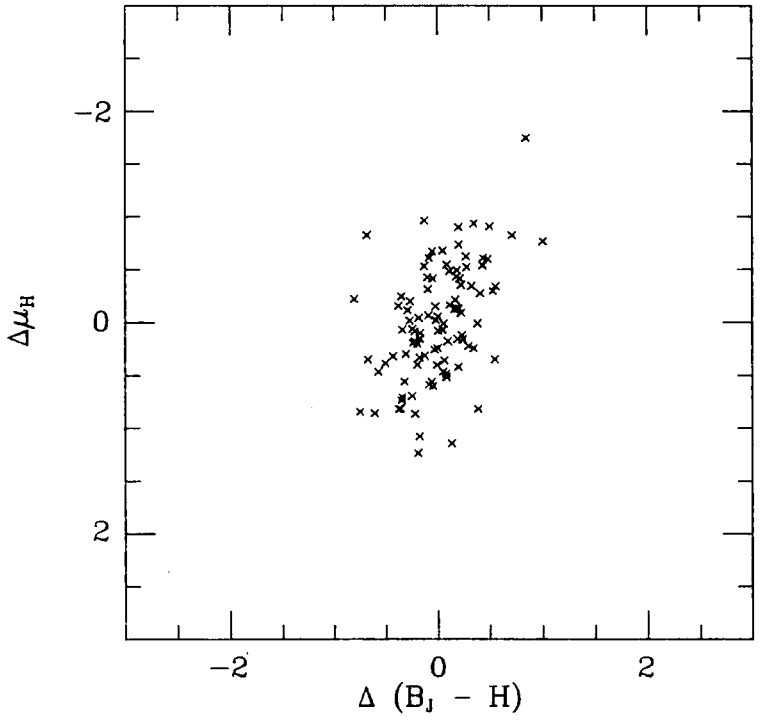

Table 5.4

Colour residuals for Bothun et al's cluster sample.

Cluster	$\Delta(B-H)$	$\Delta(B-H)_c$
A1367	0.01	0.00
A400	−0.16	−0.11
Cancer	0.00	−0.03
Coma	−0.20	−0.14
Hercules	−0.11	−0.05
Pegasus	0.15	0.11
Pisces	0.07	0.06
r.m.s.	0.13	0.09

Notes:

First column indicates deviance in $B-H$ from that defined by a mean solution for all clusters using Aaronson et al's (1986) distances. The second column incorporates a surface brightness correction.

The main conclusion from Table 5.4, then, is that there are still some environmental differences in the zero–points of $(B_J-H)-H$ relation despite the correction for surface brightness effects, but the improved relation is a promising additional method for determining cluster distances, independent of the TF relation. In the following section I test the method by comparing it with distances estimated from the infrared TF relation.

5.2.5 The Accuracy of $(B_J - H) - M_H$ Relation as a Distance Indicator

In this section I first calibrate the optical–ir C–L relation (corrected for surface brightness variation) and employ it to find distances to the groups and associations indicated in Table 5.2. The accuracy of these distances will then be tested by comparing them with those from infrared TF relation as listed in Aaronson and Mould (1983).

The $(B_J - H) - H$ C–L relations for the Virgo and Ursa Major clusters are presented in Table 5.5 since these two are the richest clusters with available optical and infrared data. The Virgo cluster data are taken from Mould, Aaronson and Huchra (1980) with optical magnitudes, subsequently reduced to the AARS system, from Longo and de Vaucouleurs (1983). The Ursa Major data are taken directly from Table 5.2. I also list the $(B_J - H) - M_H$ relation for the Local group galaxies as given in Tully et al (1982), again after correction to the AARS system. All the relations are corrected for surface brightness variations. The regressions are calculated by taking both colours and magnitudes as independent variables.

Table 5.5

Optical–ir C–L relations for the Local group and the nearby clusters.

$$H_0 = A + B(B_J - H)_c$$

Sample	A	$-B$	*r.m.s.*	r	N
Local Group		2.56 ±.25	0.53	−0.96	12
Virgo	14.45 ±.89	2.24 ±.32	0.52	−0.88	16
Ursa Major	14.78 ±.93	2.22 ±.36	0.86	−0.79	25

$$(B_J - H)_c = A + B(H_0 - 9)$$

Sample	A	B	*r.m.s.*	r	N
Local Group		0.36 ±.04	0.21	−0.96	12
Virgo	2.51 ±.07	0.35 ±.05	0.21	−0.88	16
Ursa Major	2.57 ±.06	0.28 ±.05	0.28	−0.79	25

The slopes of the optical–ir C–L relations for the Virgo, Ursa Major and Local group galaxies are in close agreement (see also Bothun et al 1985a). The

mean of the Virgo and Ursa Major slopes is therefore taken as representative for all clusters, viz:

$$(M_H)_0 = a - (2.23 \pm .30)\,(B_J - H) \qquad 5.4$$

The above C–L relation is calibrated by using Sandage and Tammann's (1976) distances to the galaxies NGC224 and NGC598. This procedure resembles that of Aaronson and Mould (1983) for calibrating the infrared TF relation. The distance moduli to the calibrating galaxies, their absolute magnitudes at $\log(A/D_0) = 0.0$ and $(B_J - H)_c$ colours corrected for surface brightness are listed in Table 5.6 and the mean zero–point calculated from them is taken as the value of 'a' in equation 5.4.

Table 5.6

Calibration of the $(B_J - H) - M_H$ relation

$$M_H = a - (2.23 \pm .30)\,(B_J - H)_c$$

Name	$m - M$	$(M_H)_0$	$(B_J - H)_c$	a
N224	24.38	−23.97	3.39	−16.41
N598	24.82	−21.17	2.21	−16.24
Mean				−16.33

Note: Distance moduli are taken from Sandage and Tammann (1976) after reducing to a modulus of 3.29 mag. for the Hyades cluster.

I now employ the $(B_J - H)_c$ colours (corrected for surface brightness) of the galaxies listed in Table 5.2 and use equation 5.4 to find distances to the groups and associations indicated in this table. The distance moduli from the optical–ir C–L and infrared TF relations (Aaronson and Mould 1983) are presented in Table 5.7 and compared in Figure 5.5. The mean of the absolute difference between distances from the C–L and TF relations for the 26 groups in Table 5.7 is |0.28| mag., which is similar in size to the C–L zero–point shifts discussed in the last section. Considering the uncertainty in the colours and scatter intrinsic to the TF method this is a very encouraging result and suggests that the combination of the TF and the improved optical–ir C–L relation will be a powerful way to examine systematic problems in the 'far-field' distance scale.

Table 5.7

Distances to nearby groups and clusters.

Name	$(m-M)_{C-L}$	σ	N	$(m-M)_{TF}$	σ	N
N134	31.15	.21	2	31.00	.07	2
Sculptor	28.31	.30	2	27.64	.19	3
N1023	30.41	.26	5	29.98	.24	5
Eridanus	31.10	.17	5	31.12	.14	8
Fornax	31.03	.25	4	30.88	.23	7
N2841	30.97	.49	3	30.96	.30	3
N3079/5459	30.80	.84	2	31.27	.08	2
N3184	30.21	.34	3	30.65	.18	3
N3521	29.96	.39	2	30.94	.54	3
Leo Triplet	29.34	.19	3	29.84	.25	3
Leo	31.60	.46	4	31.32	.23	5
Ursa Major	31.06	.17	25	31.15	.08	24
Coma I	30.68	.23	6	30.42	.32	6
Virgo South	31.06	.40	4	30.88	.22	7
Virgo	31.09	.21	9	31.08	.11	16
M81	27.98	.04	2	27.88	.14	5
CVnI	28.68	.23	3	28.45	.31	3
N5033	31.59	.31	2	31.24	.26	3
M51	29.41	.12	2	29.69	.28	2
M101	30.32	.03	2	29.01	.33	3
N5371	32.43	.21	2	32.29	.17	3
N5364	32.00	.03	2	31.10	.40	2
N5566	31.81	.48	4	31.71	.15	9
N5866	30.74	.40	2	30.48	.23	2
N6070	32.42	.17	2	32.32	.01	3
Grus	30.66	.30	4	31.20	.27	8
N7320/7331	31.20	.38	2	30.55	.52	2

Figure 5.5

Distance moduli for nearby groups derived from the $(B_J - H) - M_H$ (corrected for surface brightness) and TF relations. Error bars correspond to the $r.m.s.$ scatter around the mean distances.

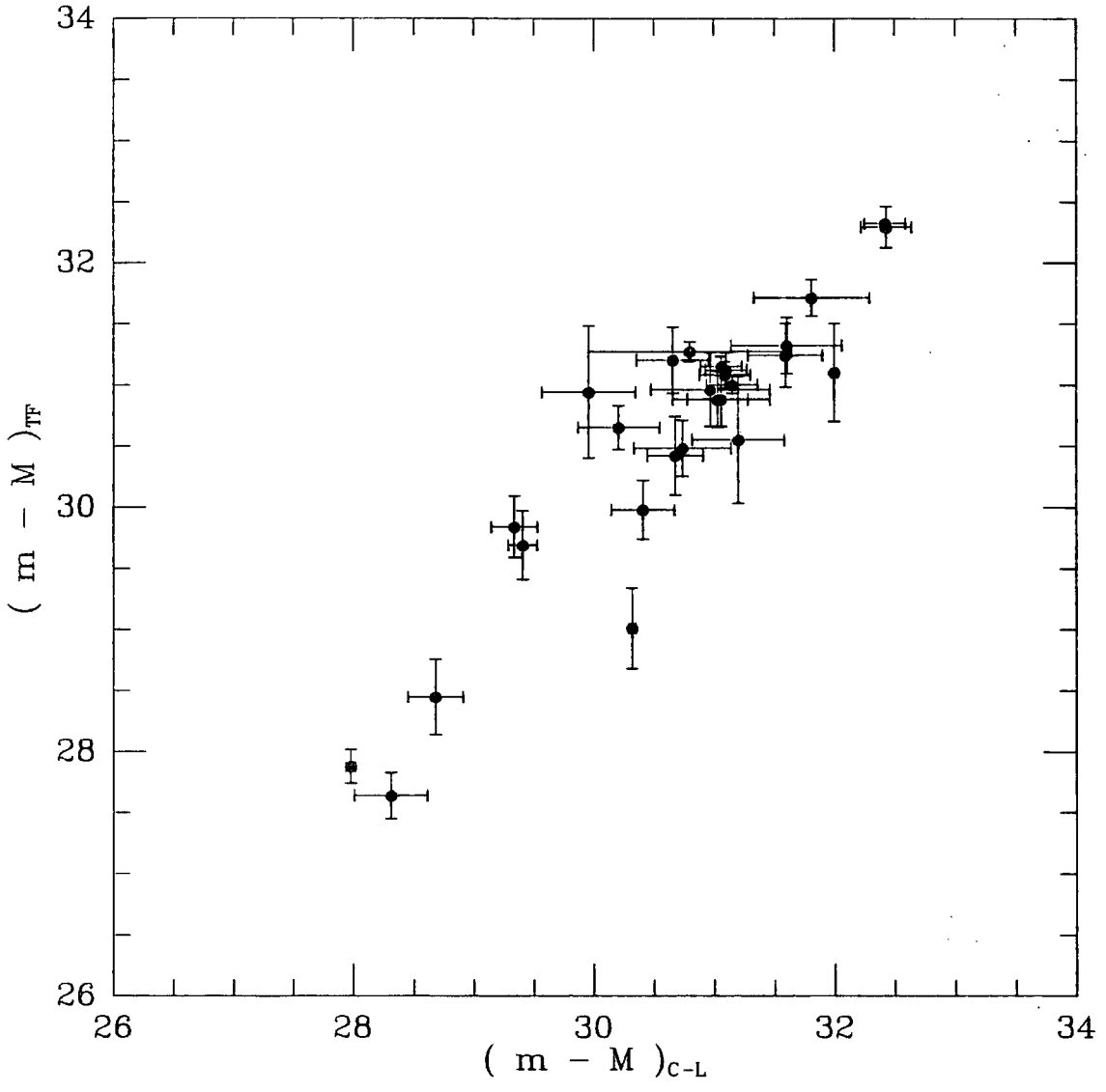

5.3 Summary and Conclusions

Galaxies with available optical and infrared data from the literature have been combined with the AARS to investigate the potential of C–L relations for distance scale determination. In the first part of this chapter the universality of the E-SO infrared C–L relation has been studied. This is followed by a detailed analysis of the type–dependence of the spiral optical–ir C–L relation. The main conclusions are summarised below:

1. The AARS infrared C–L relation for E-SO galaxies agrees well with that seen in both the Virgo and Coma cluster galaxies and is consistent with recent estimates of the motion of the Local group. No evidence has been found at infrared wavelengths for an anomalous population of cool stars in the Virgo cluster galaxies. The tight E-SO $(J-K)-K$ relations appear to be promising as distance indicators in cluster samples, though the flat slope implies 2% photometry is needed over a wide luminosity range to achieve a distance modulus precision of ± 0.10 mag.

2. A correlation between the residuals around the $\mu_H - M_H$ and $(B_J - H) - M_H$ relations of the AARS/literature spirals has been used to correct colours for bulge contamination. It has been found that this reduces the scatter and considerably improves the morphological type–independence of the zero–point of the spiral optical–ir C–L relation.

3. A sample of spirals in nearby clusters has been used to check the universality of the optical–ir C–L relation. The scatter in C–L zero–points between different clusters improves when the surface brightness correction is applied but there is still evidence for environmental dependence in this relation. The method can be used to check independently the TF distances to nearby groups. No evidence has been found for systematic deviations or a scatter larger than that found in the C–L zero–points themselves.

CHAPTER VI

INFRARED LUMINOSITY FUNCTION OF FIELD GALAXIES

6.1 Introduction

A knowledge of the galaxy luminosity function is essential for many extragalactic studies. For example, the general luminosity function of 'field' galaxies is needed to predict their redshift distribution in different apparent magnitude intervals and to construct the galaxy number–magnitude count models at large redshifts (Ellis 1982; Shanks et al 1984). Likewise, the spatial covariance function for galaxies can be obtained from the projected angular covariance function only if one specifies their redshift distribution, which can be derived for magnitude–limited samples from the luminosity function (Peebles and Hauser 1974). Finally, the analytic form of the luminosity function is required to estimate the mean luminosity density of the Universe (Shapiro 1971; Bean 1983).

A review of nine methods for determining the luminosity function of 'field' galaxies prior to 1976 has been published by Felten (1977). They were found to be in reasonably good agreement once allowance was made for differences in Hubble's constant, photometric systems and Galactic absorption laws.

It is well known that deep number–magnitude counts in optical wavebands are sensitive to evolutionary corrections and redshift effects (Peterson et al 1979; Shanks et al 1984). The evolution correction is also important if we are to derive a believable value for the deceleration parameter, q_0, from the classical Hubble diagram using brightest cluster members (Gunn and Oke 1975). Recent studies (Lilly and Longair 1982) have used infrared passbands for this purpose because the brightest cluster members are more luminous in the infrared (due to a smaller K–correction). The evolutionary correction in luminosity at infrared wavelengths involves post–main sequence evolution, which is small and might be better understood than that at ultraviolet and optical wavelengths. Therefore, infrared (2.2 μm) number–magnitude counts should provide an independent evolutionary test to the optical counts. This will become practical when infrared detector arrays are commissioned. Moreover, the redshift corrections in the infrared are better understood by virtue of the shifting the optical spectrum and are also largely independent of morphological types (see chapter 3).

In order to predict the number–magnitude counts at 2.2 μm, one must first construct the appropriate infrared luminosity function. In this chapter I undertake a detailed study of the first infrared luminosity function for 'field' galaxies.

This is of interest for its own sake of course; in as much as a comparison with the optical luminosity functions will reveal any systematic differences between galaxies at the two wavelengths.

The main goal of this chapter is to attempt to answer the following three questions:

1. Is the slope of the infrared luminosity function the same as that for the optical but shifted by the mean optical–ir colour?

2. Is there any difference between the infrared luminosity functions of different types of galaxies?

3. What are the prospects for galaxy counting at 2 μm with 2–D panoramic detectors?

In the next section I present a review of the most widely used analytical forms for luminosity functions. In section 6.3 the completeness of the AARS infrared survey is discussed. The infrared luminosity function and comparisons with its optical counterpart will be presented in section 6.4. Section 6.5 gives a detailed analysis of the errors in the luminosity function parameters. A new statistical method for deriving infrared luminosity function from a complete optically selected sample is developed in section 6.6 and is applied to the AARS infrared survey in section 6.7. There follows a discussion of the results in section 6.8 where the adopted 'field' luminosity function parameters are also presented. In section 6.9 a comparison between the luminosity functions for different types of galaxies is carried out. The infrared number–magnitude counts are presented in section 6.10. Finally, the conclusions are summarised in section 6.11.

6.2 Background to the Luminosity Function of Field Galaxies

6.2.1 Definition and Historical Review

The need for an analytical form for the luminosity function was realised in the early years of extragalactic research. This effort was initiated by Zwicky (1957) who defined the integral luminosity function as the number of galaxies brighter than an absolute magnitude M and suggested that $N(< M) = K\ (10^{0.2M} - 1)$; where K is a constant.

Using a compiled sample of about 600 'field' galaxies Kiang (1961) constructed the absolute magnitude distribution and applied an Eddington–type correction (Schechter 1976) to this distribution to compensate for errors in the M determination. He then fitted to his histogram a cubic at the bright end and a Zwicky form ($\Phi \sim 10^{0.2M}$) at the faint end. The advantages and disadvantages of Kiang's procedure are discussed in detail by Felten (1977).

Abell (1962; 1976) proposed a new analytic form for the cluster galaxy luminosity function. He represented the logarithm of the integrated luminosity function by two intersecting straight lines; the magnitude (M^*) at which the two lines intersect characterises the point at which a change in the slope of the luminosity function occurs. The Abell luminosity function can be represented by

$$\begin{aligned} \log N(< M) &= K_1 + S_1 M \qquad (M < M^*) \\ \log N(< M) &= K_2 + S_2 M \qquad (M > M^*) \end{aligned} \tag{6.1}$$

where the constant slopes have the preliminary values of $S_1 = 0.75$ and $S_2 = 0.25$ (Abell 1976). If all clusters have the same shape for their luminosity function, then M^* may be a useful 'standard candle' for determining the relative distances of clusters (Bautz and Abell 1973).

Schechter (1976) has proposed an analytical form for the differential luminosity function which has received much attention in recent years. Defining the differential luminosity function $\Phi(L)\,d(L)$ to be the number of galaxies per unit volume in the luminosity interval L to $L + dL$, he proposed

$$\Phi_S(L)\,dL = \phi^*\,(\frac{L}{L^*})^{\alpha}\,e^{-(\frac{L}{L*})}\,d(\frac{L}{L*}) \tag{6.2}$$

where ϕ^*, L^* and α are parameters to be determined from the data. The parameter ϕ^* is a normalisation parameter and L^* is the 'characteristic luminosity' at which the luminosity function exhibits a rapid change in the slope in the $(\log \Phi, \log L)$ plane. The dimensionless parameter α gives the slope of the luminosity function in the $(\log \Phi, \log L)$ plane when $L < L^*$. In terms of absolute magnitudes equation 6.2 becomes

$$\Phi_S(M)\,dM = \phi^*\,(0.4 \ln 10)(\frac{L}{L^*})^{(\alpha+1)}\,e^{-(\frac{L}{L*})}\,dM \tag{6.3}$$

where $L/L^* = dex(0.4(M^* - M))$ with M^* being equivalent to L^* and representing the 'characteristic absolute magnitude'.

Equation 6.3 differs from the previous analytical expressions discussed above in that the luminosity appears in two exponential terms and also that there is no discontinuous break in the luminosity function at its characteristic magnitude. The expression gives a good approximation to both 'field' (Kirshner et al 1978) and cluster (Schechter 1976; Dressler 1978) luminosity functions. However, in the case of the cluster luminosity functions, the fit is worse when cDs are included. cD galaxies appear to have higher luminosities than expected from comparison with the bright end of the 'field' luminosity function.

I now summarise two independent and widely used methods (e.g. Bean 1983) for fitting analytic forms to observed luminosity functions.

6.2.2 Luminosity Function Fitting Methods

The methods which will be explained in the next sections were exploited by Bean (1983) to study the optical luminosity function of all five fields of the AARS. A comparison between the results was also carried out to investigate the sensitivity of the luminosity function parameters to non–homogeneities in the galaxian distribution.

a. Traditional Least Squares Method

This method fits the analytic form of the luminosity function to the binned data. The luminosity distribution of a randomly chosen sample is defined as

$$dN_P(M) = \Phi(M)\, V(M)\, dM \qquad 6.4$$

where $dN_P(M)$ is the predicted number of galaxies per absolute magnitude bin, $\Phi(M)$ is the differential luminosity function and $V(M)$ is the maximum volume corresponding to a given absolute magnitude bin. The volume is given by

$$V(M) = \frac{1}{3} \sum_{i=1}^{K} \Omega_i\, {d_i}^3 \qquad 6.5$$

where K is the number of separate fields in a given sample, Ω_i the solid angle of each field and d_i is the maximum distance which a galaxy in the bin M, $M + dM$ can be seen at the magnitude limit (m_{lim}) of the sample. Using first order curvature terms and K–corrections, $d_i(Mpc)$ is calculated as:

$$M_i = (m_{lim})_i - 5 \log d_i - 25 - (K + 1.086(1 - q_0)) \frac{H_0 d_i}{c} \qquad 6.6$$

Since equation 6.6 is non–linear, an iterative procedure should be used to calculate d_i.

Due to the finite width of the absolute magnitude bins, the volume varies slightly across each bin. The second derivative of the volume with respect to absolute magnitude is therefore used to correct the predicted $N(M)$ distribution as follows (Schechter 1976)

$$dN_P(M) = \Phi(M)\, V(M)\, dM + \frac{d^2}{dM^2} [\, \Phi(M)\, V(M)\,] \frac{dM^2}{24} \qquad 6.7$$

In the case of the AARS, this correction will also depend on q_0 and the K–term. For simplicity however, I calculate this second order correction in the Eucledian case since the mathematics concerned is more tractable and in any case the additional effect is small.

Assuming the Schechter form for $\Phi(M)\,d(M)$ (eq. 6.3) and the observed number of galaxies in a given absolute magnitude bin, dN_O, one could now form

$$\chi^2 = \sum_{i=1}^{n} \frac{(dN_{Oi} - dN_{Pi})^2}{\sigma_i^2} \qquad 6.8$$

where σ_i^2 is the variance for each bin and the summation is over absolute magnitude intervals. Assuming a Poisson distribution, one can replace σ_i^2 by dN_{Oi}. The best fitting M^*, α and ϕ^* can be estimated by minimising χ^2.

This method has the advantage of being straightforward. It yields a luminosity function ($\Phi(M)\,d(M)$) that can be plotted and inspected. However, it assumes a homogeneous distribution for galaxies and the results are therefore sensitive to clustering in the galaxian distribution. For example, most low luminosity galaxies in a magnitude limited sample come from a nearby small volume which may or may not be representative. In the next section a technique will be presented which is largely independent of inhomogeneities in the sample provided the luminosity function is the same everywhere. A comparison between the results from the two methods will test the sensitivity of the luminosity function parameters to clustering.

b. Cluster–Free Maximum Likelihood Method

This method is a variant of Sandage et al's (1979) procedure which was used to analyse the distribution of galaxies in the revised Shapley–Ames catalogue. In the following discussion I present a detailed derivation of the method and then apply it to the AARS in the next section.

Let $P(M \mid Z)$ be the probability of finding a galaxy with redshift $(Z, Z+dZ)$ and absolute magnitude $(M, M+dM)$. The number of galaxies in a given $dM\,dZ$ bin is hence

$$\varphi(M \mid Z)\,P(M \mid Z)\,dM\,Z^2\,dZ\,d\Omega \qquad 6.9$$

where $d\Omega$ is the solid angle of the field and $\varphi(M \mid Z)$ is the selection function defined as

$$\varphi(M \mid Z) = \begin{cases} 1 & \text{if } M + 25 + 5\log(\frac{cZ}{H_0}) + (K + 1.086(1-q_0))Z \leq m_{lim} \\ 0 & \text{if } M + 25 + 5\log(\frac{cZ}{H_0}) + (K + 1.086(1-q_0))Z > m_{lim} \end{cases}$$

Integrating equation 6.9 over redshift gives the number of galaxies in a given M bin

$$dN(M) = \int_{Z=0}^{\infty} P(M \mid Z)\,\varphi(M \mid Z)\,dM\,Z^2\,dZ\,d\Omega \qquad 6.10$$

Now, if one assumes that $P(M \mid Z)$ is separable (i.e. the luminosity function is the same everywhere), then

$$P(M \mid Z) = \Phi(M)\,D(Z) \qquad 6.11$$

or

$$dN(M) = \Phi(M)\, dM \int_{Z=0}^{\infty} D(Z)\, \varphi(M \mid Z)\, Z^2\, dZ\, d\Omega \qquad 6.12$$

Now, let Z_{max} be the maximum redshift at which a galaxy of luminosity M can be observed at the magnitude limit of the sample. Therefore,

$$\int_0^{\infty} D(Z)\, \varphi(M \mid Z)\, Z^2\, dZ\, d\Omega = \int_0^{Z_{max}} D(Z)\, \varphi(M \mid Z)\, Z^2\, dZ\, d\Omega \qquad 6.12'$$

Combining equations 6.12 and 6.12′, the number of galaxies brighter than an absolute magnitude M, $N(< M)$, is estimated as

$$N(\leq M) = \int_{-\infty}^{M} \Phi(M)\, dM \int_0^{Z_{max}} D(Z)\, \varphi(M \mid Z)\, Z^2\, dZ\, d\Omega \qquad 6.13$$

Finally using equations 6.12, 6.12′ and 6.13, one could find the probability (P) of observing a galaxy with absolute magnitude M at redshift Z

$$P \equiv \frac{dN(M)}{N(\leq M)} = \frac{\Phi(M)\, dM}{\int_{-\infty}^{M(Z)} \Phi(M)\, dM} \qquad 6.14$$

It is clear that equation 6.14 does not contain any density–dependent term. However, note that it is also independent of the normalisation of the luminosity function (ϕ^*) which must be calculated from other methods (e.g. from galaxy counts).

Employing the probability defined by equation 6.14, a likelihood function is constructed as

$$L = \prod_{i=1}^{N} P_i \qquad 6.15$$

or

$$\ln L = \sum_{i=1}^{N} \ln P_i \qquad 6.16$$

where N is the total number of galaxies brighter than the magnitude limit of the sample. Substituting equation 6.14 into 6.16 gives

$$\ln L = \sum_i \left[\ln \Phi(M_i)\, dM_i - \ln\left(\int_{-\infty}^{M(Z_i)} \Phi(M)\, dM \right) \right] \qquad 6.17$$

This equation can be simplified by assuming a Schechter form (equation 6.3) for the luminosity function. Therefore,

$$I \equiv \ln \Phi(M_i) = \ln \left[\phi^* (0.4 \ln 10) \left(\frac{L_i}{L^*}\right)^{(\alpha+1)} e^{-\frac{L_i}{L^*}} \right] = (\alpha + 1)\, \ln\left(\frac{L_i}{L^*}\right) - \frac{L_i}{L^*} + C \qquad 6.18$$

Which can be re–written as

$$I \equiv \ln \Phi(M_i) = (\alpha + 1) \ln \ell_i - \ell_i + C \qquad 6.19$$

where $\ell_i = \frac{L_i}{L^\circ} = dex(0.4(M^* - M_i))$ and $C = \ln(0.4\phi^* \ln 10)$ is a constant.

Now, the second term in equation 6.17 becomes

$$II \equiv \int_{-\infty}^{M(Z_i)} \Phi(M)\, dM =$$

$$= \int_{-\infty}^{M(Z_i)} \phi^* \,(0.4 \ln 10) \left[10^{0.4(M^\circ - M)}\right]^{(\alpha+1)} e^{-\left[10^{0.4(M^\circ - M)}\right]}\, dM \qquad 6.20$$

Taking $X = dex(0.4(M^* - M))$ gives $dX = -0.4 \ln(10)\, X\, dM$ and equation 6.20 is transformed to

$$II \equiv \int X^\alpha\, e^{-X}\, dX = \Gamma\,(\alpha + 1, X) + C' \qquad 6.21$$

where Γ is the incomplete gamma function and C' is a constant. Finally, substituting equations 6.19 and 6.21 into 6.17 gives the likelihood function, $\ln L$, as

$$\ln L = \sum_i (\alpha + 1)\, \ln \ell_i - \sum_i \ell_i - \sum_i \ln\, \Gamma\left(\alpha + 1, 10^{0.4(M^* - M(Z_i))}\right) \qquad 6.22$$

where $\ell_i = dex(0.4(M^* - M_i))$. The likelihood function $\ln(L)$ in equation 6.22 is now maximised to determine the luminosity function parameters M^* and α. As was shown earlier, this fitting technique is independent of clustering in the galaxian distribution provided the luminosity function is the same in the field and clusters. This method is called the ***cluster–free fitting method*** and the luminosity functions derived from it are refered to as ***cluster–free*** luminosity functions.

6.3 Completeness of the AARS

In order to construct a 'field' luminosity function one requires a large sample of galaxies with available redshifts, complete to an apparent magnitude limit. This complicates the task of finding the infrared luminosity function from the present sample since the AARS is selected in optical wavebands and is not likely to be complete in the infrared. Objects with strong infrared emission may be too red to be included in the optically selected survey. This point is demonstrated in Figure 6.1; at faint K only the bluest objects are detectable in B_J. Redshift introduces a second order effect. The range of rest–frame $B_J - K$ colours is about 1 magnitude whereas over $0 < Z < 0.1$ early–type galaxies are K–corrected in colour by up to 0.4 mag. Therefore, distant galaxies (with large luminosities) are systematically missed at a rate depending on their K–correction and hence their intrinsic $B_J - K$ colour. The first objective in this section must be to define the infrared completeness limit of the AARS. Since the optical–ir colour distributions amongst the AARS fields are different, a step–function might be a reasonable form for the selection function indicating that some of the data will not be used.

The infrared K–magnitude limits for different AARS fields are estimated from Figure 6.1 by noting the magnitude at which the observed colour distribution becomes incomplete. This is clearly somewhat subjective and I therefore

Figure 6.1

$K - (Bj - K)$ diagram for galaxies in the different AARS fields and all the fields together. Vertical lines show the estimated apparent magnitude limits at which the sample might be complete.

Observationally inaccesible portion of the diagram, corresponding to $B_J = (B_J)_{lim}$, is also shown.

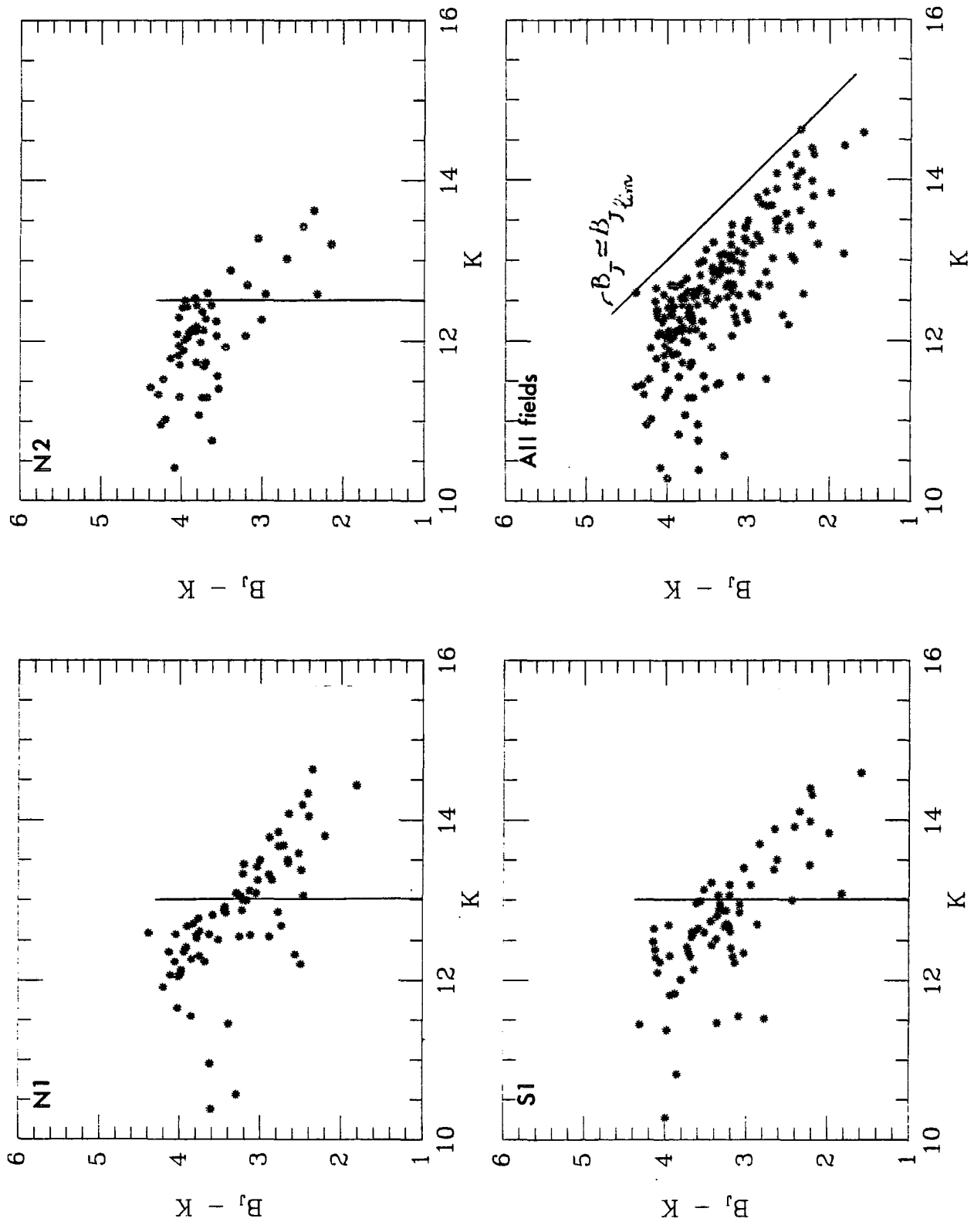

check these completeness limits (Table 6.1) via a V/V_{max} test (Schmidt 1968). For each galaxy in the sample equations 6.5 and 6.6 are used to calculate the relativistic volume, V, covered by the galaxy at its observed redshift and the maximum volume, V_{max}, encompassed by the galaxy at the magnitude limit of the field. The volumes are calculated assuming K–corrections from chapter 3. If the field is complete to its magnitude limit and the galaxies are homogeneously distributed, one expects

$$< V/V_{max} >= 0.50 \pm \frac{1}{11\sqrt{N}} \qquad 6.23$$

The $< V/V_{max} >$ values corresponding to different K magnitude limits of the AARS fields are calculated and for each field, the variation in $< V/V_{max} >$ ratios with its respective K magnitude limit is shown in Figure 6.2. Strictly speaking, if galaxies in a field are homogeneously distributed, then the apparent magnitude limit corresponding to $< V/V_{max} >= 0.50$ can be taken as the completeness limit of that field. This procedure does, however, assume that any variation in the $< V/V_{max} >$ values as a function of magnitude limit is due to incompleteness of the sample and not inhomogeneities.

Considering Figure 6.2 and the AARS infrared magnitude limits as indicated on Figure 6.1, it becomes clear that a value of $< V/V_{max} >= 0.5 \pm .10$ roughly corresponds to the estimated magnitude limits. This confirms that the adopted magnitude limits from Figure 6.1 are fairly reasonable. The estimated K magnitude limits, the $< V/V_{max} >$ ratios corresponding to these magnitudes and the number of galaxies brighter than K_{lim} in each field are presented in Table 6.1a. The last line of this table gives the total number of galaxies brighter than the magnitude limits in the original optical survey which also have infrared measurements. A total of 55 galaxies would have to be excluded from the original sample in order to construct a complete infrared survey.

A more useful check on the sensitivity of these V/V_{max}–deduced magnitudes to inhomogeneities in the case of the AARS is done by comparing the B_J limits derived from the V/V_{max} method with those known from the AARS selection criteria (e.g. apparent magnitude distributions). For this purpose I use the isophotal B_J magnitudes, since these were the ones used to select the sample. Following the procedure described above I employ the V/V_{max} method to find the isophotal B_J magnitude limits as listed on the last line of Table 6.1c. The completeness limits as estimated from the original AARS selection criteria (Bean 1983) and the number of galaxies brighter than these limits for each field are presented respectively on the first and second lines of this table. With the exception of the N2 field discussed in more detail below, the limiting B_J magnitudes determined from the V/V_{max} method are in excellent agreement with those set in the original AARS catalogue. This implies that on scales of interest the inhomogeneities do not seriously perturb the magnitude limits derived by the V/V_{max} method.

The N2 field appears to be complicated by two factors. Firstly, the ten faintest optically–selected galaxies were not observed at K due to a shortage of telescope time. Excluding these galaxies from the original optical survey (based on the isophotal magnitudes) reduces the expected isophotal $(B_J)_{lim}$ to 16.95

Figure 6.2

$< V/V_{max} >$ versus K magnitude limits for the $N1$, $N2$ and $S1$ fields.

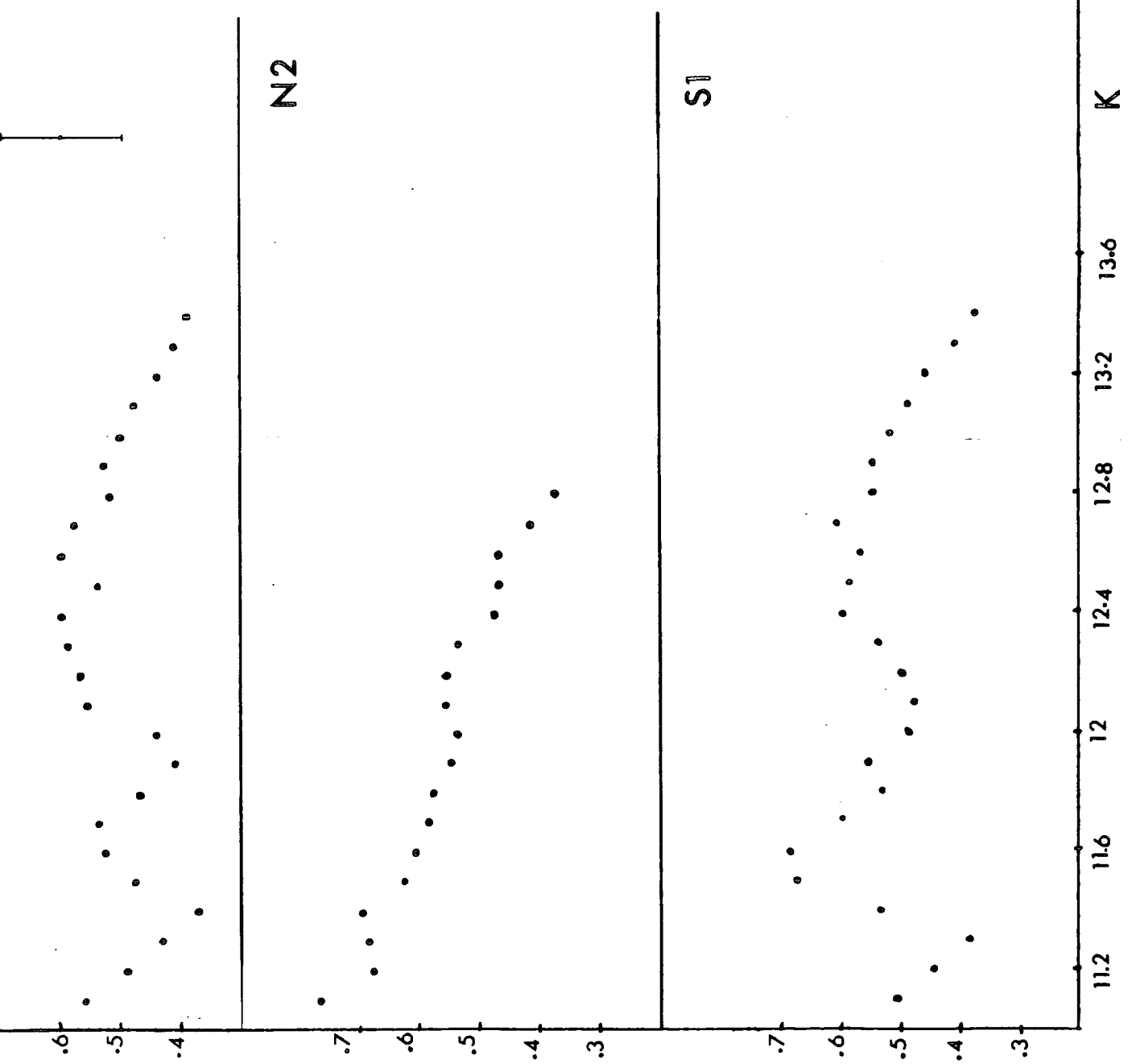

mag. Secondly, inspection of the $N(Z)$ distribution reveals the presence of a prominent cluster in this field at $Z = 0.04$ which may bias the V/V_{max} ratios to smaller values before the true K_{lim} has been reached.

In order to examine the sensitivity of the adopted magnitude limit of the N2 field to inhomogeneities in its redshift distribution, I replace the cluster in this field by one galaxy with a redshift and magnitude corresponding to the mean values of the cluster galaxies. Employing the V/V_{max} test I re–estimate the magnitude limit of this field and find that it changes by less than 0.10 mag. Nevertheless, I appreciate this entire procedure could be in error by as much as 0.2 magnitude.

To investigate the sensitivity of the final luminosity function results to uncertainties in the adopted infrared magnitude limits of individual fields, a series of numerical experiments have been carried out. I fixed the completeness limits of two fields and changed the limit of the third field in 0.05 mag. steps around the selected K_{lim}. In each case the Schechter luminosity function parameters were calculated and were found to be relatively insensitive to small changes in K–magnitude limit around its adopted value (M^* changes by less than 0.07 mag. and α by 0.07 over a range of 0.25 mag. in the magnitude limit). Therefore, uncertainties of the order of $0.15 - 0.20$ mag. in the adopted magnitude limits in Table 6.1 should not alter the conclusions in this chapter.

As was mentioned in the last section, one of the principal goals in this chapter is to investigate the difference between the optical and infrared luminosity function parameters. Therefore the AARS optical survey, based on the B_J aperture magnitudes, must also be analysed in the same way as the infrared sample. The B_J aperture–magnitude limits for different fields of the AARS, their corresponding $< V/V_{max} >$ values and the total number of galaxies brighter than the magnitude limits are hence calculated and listed in Table 6.1b. The optical and infrared magnitude limits presented in Table 6.1 will be used as the completeness limits of the AARS fields in the subsequent studies.

Table 6.1

Estimated infrared and optical magnitude limits of the AARS

Table 6.1a

	$S1$	$N1$	$N2$
INFRARED MAGNITUDES			
K_{lim}	13.00	13.00	12.50
$< V/V_{max} >$	0.52 $\pm.10$	0.50 $\pm.10$	0.50 $\pm.10$
$N(< K_{lim})$	49	40	44
$N(< B_{J_{lim}})$ (ir sub-sample)	65	67	56

Table 6.1b

APERTURE MAGNITUDES			
$B_{J_{lim}}$	16.90	17.00	16.35
$< V/V_{max} >$	0.48 $\pm.10$	0.50 $\pm.10$	0.50 $\pm.10$
$N(< B_{J_{lim}})$	66	66	47

Table 6.1c

ISOPHOTAL MAGNITUDES			
$B_{J_{lim}}$ (True)	17.05	17.36	17.12
$N(< B_J)$	74	70	70
$B_{J_{lim}}$ (Estimated)	17.08	17.38	16.52

6.4 The Infrared Luminosity Function of Field Galaxies

Knowing the completeness limits of the AARS fields one can now construct the infrared differential luminosity function $\Phi(M_K)\,dM_K$ using both the traditional and cluster–free methods discussed earlier. Equations 6.5 and 6.6 have been used to calculate V_{max}, the maximum volume covered by a given galaxy when shifted to the magnitude limit of the sample. The contribution of that galaxy to the total luminosity function at a given luminosity, L, is then $1/V_{max}$. The sum of the $1/V_{max}$ values (for all the galaxies in the complete survey) in absolute magnitude bins gives the differential luminosity function in units of number of galaxies per unit volume per luminosity interval.

The differential 'field' luminosity function for the infrared survey is presented in Figure 6.3a. Bin sizes are 0.25 magnitudes and error bars correspond to the square root of the number of galaxies in each absolute magnitude bin. The traditional method is applied to the binned data over an absolute magnitude range of $-26.50 < M_K < -23.00$. At the faint end I replace the three faintest bins by a single bin of size 0.75 mag. so that all the bins contain more than four galaxies. It has been found that a reasonable change in the absolute magnitude range does not have a significant effect on the results from this method. The estimated infrared luminosity function parameters from the traditional method are listed in Table 6.2 and their corresponding fit is plotted on Figure 6.3a.

The cluster–free fitting method has the distinct advantage that it does not require data binning. However, first a comparison is performed between the results from the two methods over the same absolute magnitude range (see Table 6.2). When the luminosity range is adjusted it is found that the results are insensitive to changes in the faint end limit of the luminosity function but strongly depend on the limit at the bright end. For example, changing the absolute magnitude range to $-26.25 < M_K < -23.00$ increases M_K^* and α by 0.4 mag. and 0.3 respectively. This is because the cluster–free fitting method gives more weight to galaxies at the bright end of the luminosity function (see equation 6.14).

The cluster–free and traditional method luminosity functions are compared in Figure 6.3a. A χ^2 test gives $\chi^2_\nu = \chi^2/\nu = 0.90$ with $\nu = 9$ degrees of freedom. The cluster–free luminosity function is normalised by minimising the scatter around it. The absolute magnitude distribution (not corrected for the volume) for the complete infrared survey is presented in Figure 6.3b. The predicted distribution (solid line) is normalised to the observed total number of galaxies in the complete survey.

I now exploit the blue (B_J) aperture magnitudes to construct the AARS optical luminosity function for those fields observed at the UKIRT. The reader is refered to Bean (1983) for a more detailed discussion of the optical data. The purpose in analysing the optical survey is twofold; firstly, a direct comparison between the results from the optical and infrared luminosity functions can be made using the *same* samples. Secondly, the optical survey is more appropriate for investigating the accuracy of different fitting methods because of its straightforward selection function. The traditional and cluster–free fitting methods are applied to the optical data over an absolute magnitude range of $-23.00 < M_{B_J} < -18.50$ and their estimated luminosity function parameters are listed in Table 6.2.

Figure 6.3b

Infrared absolute magnitude distribution for the complete AARS sample. Solid line shows the predicted luminosity distribution corresponding to the traditional method luminosity function parameters (see Table 6.2).

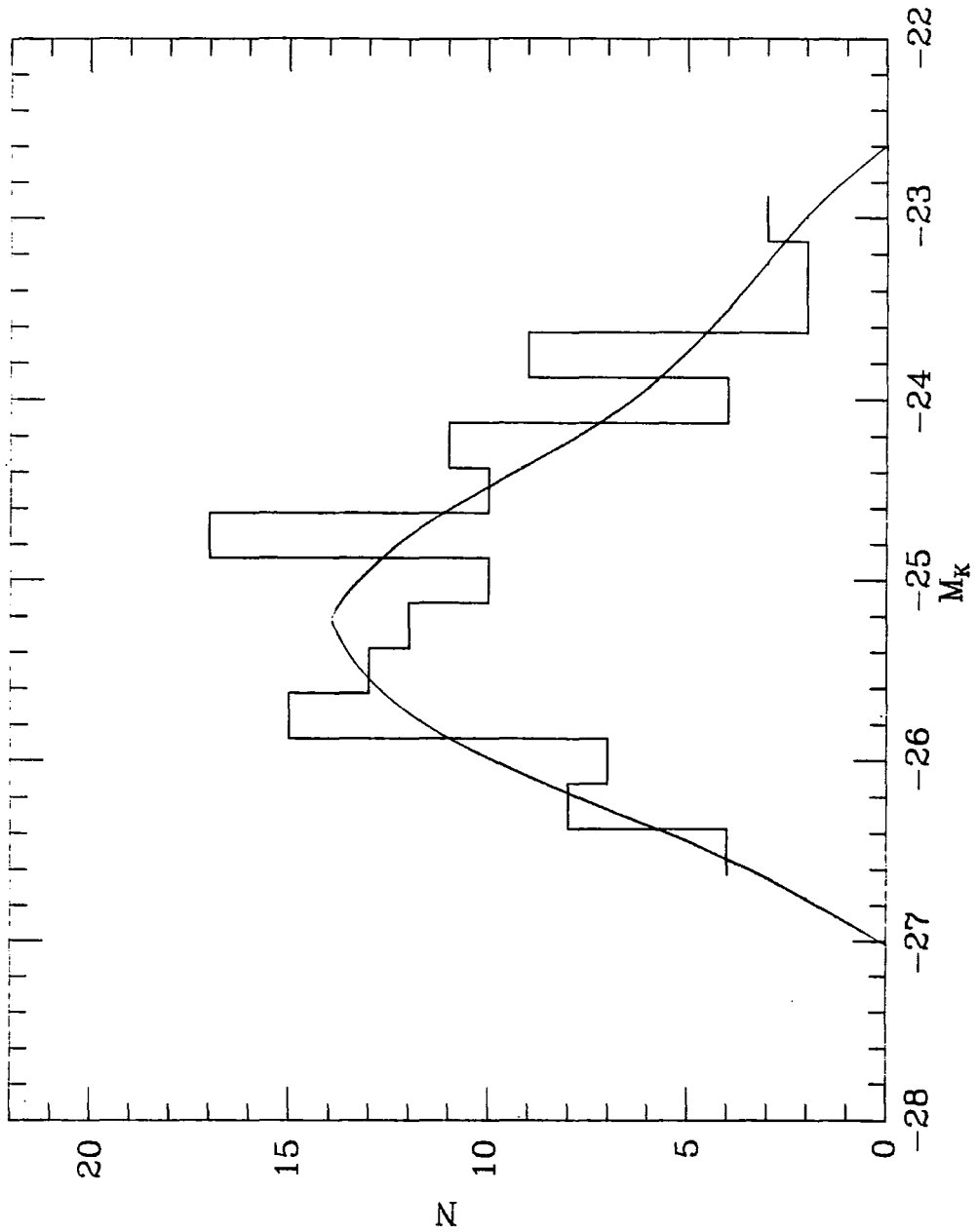

Figure 6.3a

Infrared differential luminosity function. Error bars correspond to the square root of the number of galaxies in each absolute magnitude bin. The lines indicate a Schechter function fit to the data using traditional (—-) and cluster-free (— — —) fitting methods. $H_0 = 50$ Km/sec/Mpc has been assumed.

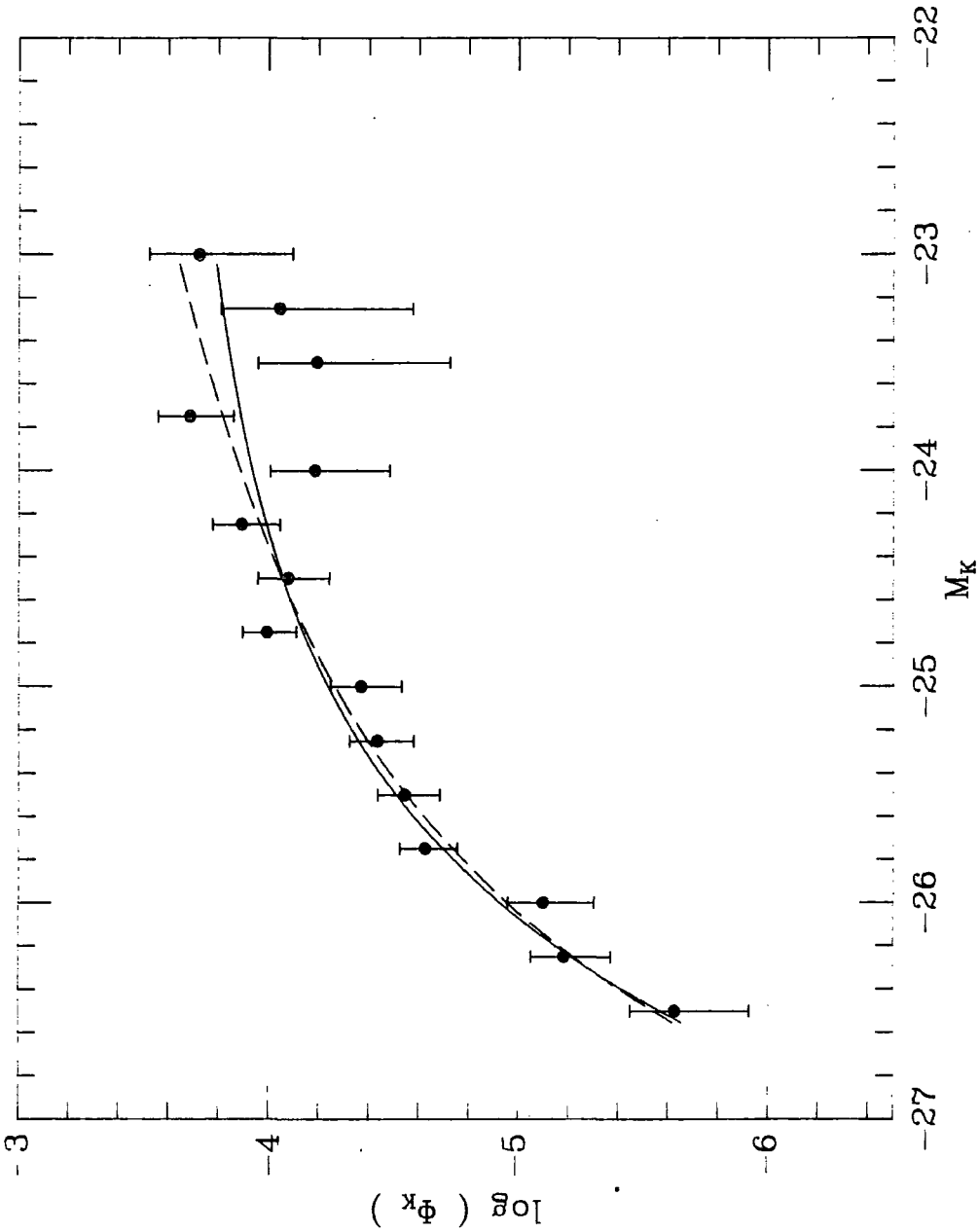

Note that the optical and infrared luminosity function parameters as calculated in this section and listed in Table 6.2 are based on a sample of 'field' galaxies with objects of all morphological types. I defer a comparison between the luminosity functions at the two wavelengths until section 6.8. Also, it is well known that the luminosity function parameters are strongly correlated and hence an accurate comparison between the results from the two fitting methods (see Table 6.2 and Figure 6.3a) is not straightforward. A more rigorous comparison will be carried out after investigating the uncertainties in the estimated luminosity function parameters in the next section.

6.5 Error Estimations in the Luminosity Function Parameters

The errors associated with the luminosity function parameters will be analysed in this section. First I present the standard error contours for the correlated parameters M^* and α. I then describe a statistical technique for calculating uncertainties in fitting procedures. A Monte Carlo simulation is carried out in section 6.5.3 to examine the accuracy of the two luminosity function fitting methods and to study the effects of sampling and inhomogeneities in the final results.

6.5.1 Error Contours

The conventional procedure for estimating errors in correlated parameters is to construct the appropriate error contours in the parameter space and calculate the 'confidence level' that the two values lie in these regions. The 'confidence level' is defined here as a quantitatively predictable fraction of all experiment repetitions. If $\chi^2_\nu(\gamma)$ are the values of a χ^2 distribution with ν degrees of freedom and significance γ, their respective 'confidence level' corresponds to the contour that encloses the true value in $1-\gamma$ of all experiments.

Consider equations 6.8 and 6.22 for a given set of Schechter parameters and let χ^2_{min} and $\ln(L_{max})$ be their optimised estimates. One could then define (Lampton et al 1976)

$$\begin{aligned} \chi^2 &= \chi^2_{min} + \chi^2_\nu(\gamma) && Traditional \\ \ln L &= \ln L_{max} - \frac{1}{2}\chi^2_\nu(\gamma) && Cluster-Free \end{aligned} \qquad 6.24$$

where ν is the number of parameters in the fit. The $\chi^2_2(0.32) = 2.3$ and $\chi^2_3(0.32) = 3.5$ values are taken as the 1σ confidence intervals. For different estimates of the fit parameters, the fractions of the ν–dimensional parameter–space such that $\chi^2 - \chi^2_{min} < \chi^2_\nu(\gamma)$ and $\ln(L_{max}) - \ln(L) < \chi^2_\nu(\gamma)/2$ form contours on the parameter–space which will contain the true values of the parameters in $1-\gamma$ of all similar experiments.

The 1σ error contours for both the traditional and cluster–free luminosity functions are drawn on the (M^*, α) plane around their best estimates (Figure 6.4). The 1σ error estimates (68% confidence interval) are listed in Table 6.2 for both the infrared and optical luminosity functions.

Figure 6.4

1σ error contours (68% confidence limits) around the best luminosity function parameter estimates for both traditional (— — —) and cluster-free (—·) fitting methods as applied to the infrared complete sub-sample.

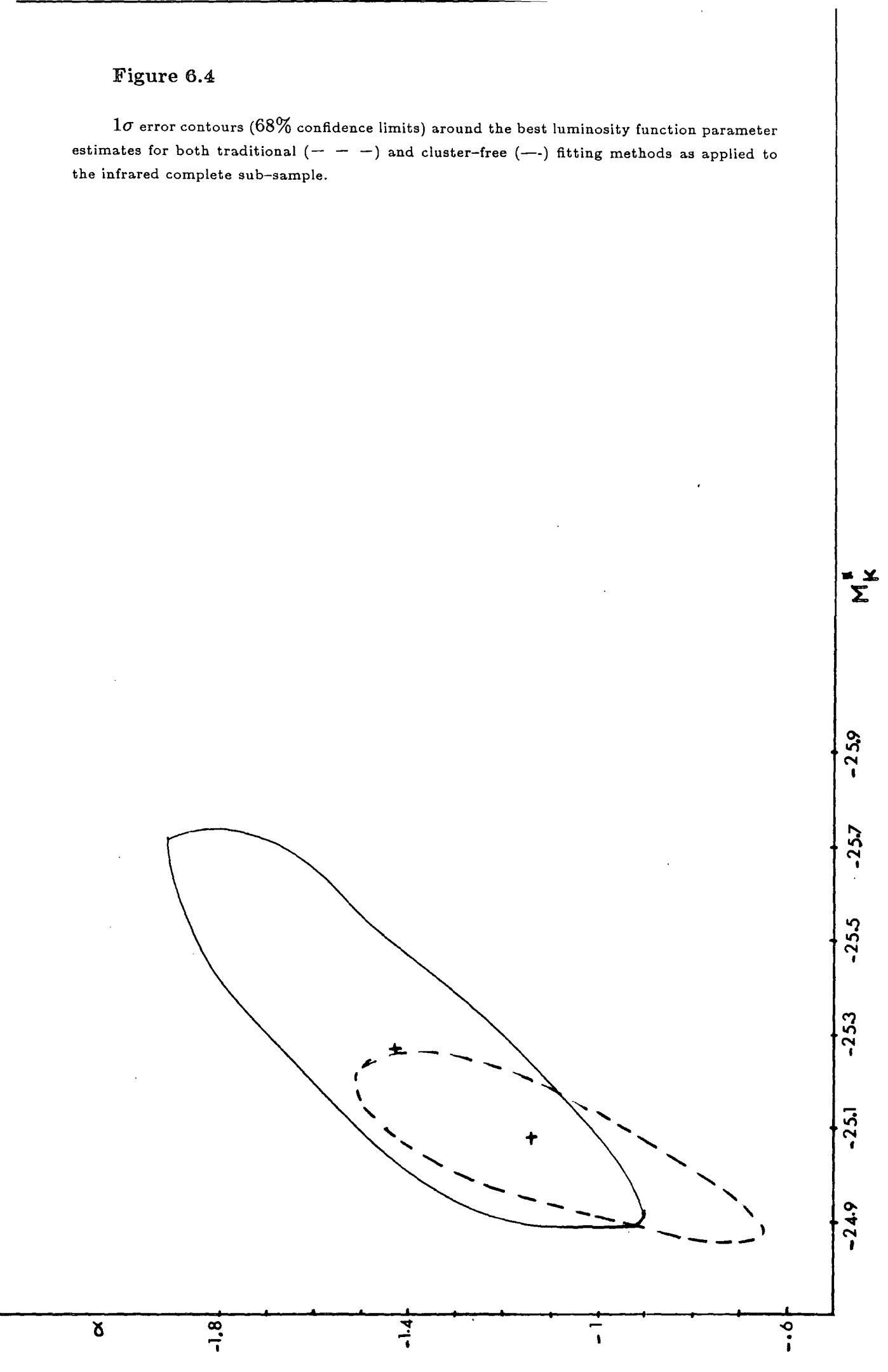

The degree of correlation between α and M^* is clear from the slope of the error contours in Figure 6.4. The Schechter luminosity function parameters derived from the traditional method appear to have smaller errors than those from the cluster–free fitting procedure. A likely explanation is that the latter weights galaxies according to their luminosities and hence bright (i.e. less numerous) galaxies are given more weight. The two methods will be compared more rigorously in the following sections by applying them to simulated catalogues to calculate the uncertainties associated with each method. Prior to this study, however, it will be useful to check the results in this section by appealing to a different method. This is the subject of the next section where an independent statistical technique will be explained and then employed to estimate the confidence intervals in the luminosity function parameters.

6.5.2 Jackknife Method for Estimating Errors

In the following discussion I present a powerful statistical technique which provides direct numerical approximations for the standard error and can give reasonably reliable confidence limits. The technique is the standard 'Jackknife' method (Quenouille 1956) which is a linear approximation to a more widely used 'Bootstrap re–sampling method' (Efron 1979) and is applicable to cases with correlated parameters. The Jackknife is a non–parametric method for estimating the bias and variance of a statistic of interest. Compared to the χ^2 method (Lampton et al 1976) it has the advantage that it does not assume a normal distribution for errors.

Let $X_1, X_2, \ldots, X_n$ be a sample of independent and identically distributed random variables. Let $\hat{\theta}$ be an estimation of the parameter θ based on the sample of size n and $\hat{\theta}_{-i}$ be the corresponding estimator with X_i omitted. In the standard Jackknife method the bias is calculated as

$$\hat{B} = (n-1)(\hat{\theta}_{\cdot} - \hat{\theta}) \qquad 6.25$$

where $\hat{\theta}_{\cdot} = \sum_{i=1}^{n} \hat{\theta}_{-i}/n$. The bias corrected θ is then

$$\tilde{\theta} = \hat{\theta} - (n-1)(\hat{\theta}_{\cdot} - \hat{\theta}) \qquad 6.26$$

Equation 6.26 has the property that it removes the order $1/n$ term from a bias, $E(\hat{\theta})$, of the form

$$E(\hat{\theta}) = \Theta + \frac{a_1(\theta)}{n} + O(\frac{1}{n^2}) \qquad 6.27$$

An extension of this technique to reduce biases of higher order is given in Miller (1974).

The Jackknife estimate for variance is (Efron 1979)

$$\hat{S}^2 = \frac{1}{n(n-1)} \sum_{i=1}^{n} \tilde{U}_i^2 \qquad 6.28$$

where $\tilde{U}_i = (n-1)(\hat{\theta}_{\cdot} - \hat{\theta}_{(-i)})$. Equation 6.28 can be simplified to give

$$\hat{S}^2 = \frac{n-1}{n} \sum_{i=1}^{n} (\hat{\theta}_{\cdot} - \hat{\theta}_{(-i)})^2 \qquad 6.29$$

It is now clear that the statistic

$$T \equiv \frac{\sqrt{\tilde{\theta} - \theta}}{S} = \frac{\sqrt{n(\tilde{\theta} - \theta)}}{\left[(n-1)\sum_{i=1}^{n}\left(\tilde{\theta}_{\cdot} - \tilde{\theta}_{(-i)}\right)^2\right]^{1/2}} \qquad 6.30$$

has an approximate t–distribution with $n-1$ degrees of freedom (Tukey 1958). Therefore, one could define $\pm t_{\beta}^{n-1}\,\hat{S}$ as the $1-2\beta$ confidence interval for θ, where t_{β}^{n-1} are the β upper percentile points of a t–distribution with $n-1$ degrees of freedom. It can be shown that for 68% confidence limits; $\beta = 0.16$ and $t_{\beta}^{n-1} = 0.992$ for $n > 100$ points.

This technique is used to estimate the standard deviation and bias in the luminosity function parameters. The method is not applicable for cases where data is distributed into bins. Therefore, it can only be used to estimate errors in parameters derived from the cluster–free fitting method. This method is applied to the complete AARS sample by excluding one galaxy at a time and optimising the Schechter luminosity function parameters using the rest of galaxies. The best fitting estimates of M^* and α are then stored in a matrix and the bias and standard deviations are calculated, using their 'true' values given in Table 6.2.

The 68% confidence limits from the Jackknife method are also presented in Table 6.2. The bias in the optical luminosity function parameters, calculated from 6.25, is found to be $|dM_{B_J}| = 0.50$ mag. and $|d\alpha| = 0.03$. The reliability of this technique and its error estimate will now be examined using simulated catalogues.

Table 6.2

Infrared and optical luminosity function parameters
and their associated errors.

Method	M_K^*	χ^2 method	Jackknife	α	χ^2 method	Jackknife	ϕ^* $\times 10^3$	$1\sigma^\dagger$ $\times 10^3$
Traditional	-25.03	.15	–	-1.12	.23	–	0.66	.12
Cluster–free	-25.26	.27	.23	-1.43	.25	.19	–	–
	$M_{B_J}^{*\ddagger}$	χ^2 method	Jackknife	α	χ^2 method	Jackknife	ϕ^* $\times 10^3$	$1\sigma^\dagger$ $\times 10^3$
Traditional	-21.42	.10	–	-1.09	.17	–	0.90	.21
Cluster–free	-21.36	.17	.18	-1.20	.19	.18	–	–

Note:

$^\dagger 1\sigma$ errors in ϕ^* from the simulation results.
ϕ^*s are in $n/(Mpc)^3$.
$^\ddagger M_{B_J}$ represents the blue aperture magnitude.

Traditional method: $(M_K^*)_{\alpha=-1} = -24.97$ $(M_{B_J}^*)_{\alpha=-1} = -21.37$
Cluster–free method: $(M_K^*)_{\alpha=-1} = -24.83$ $(M_{B_J}^*)_{\alpha=-1} = -21.16$

6.5.3 Monte Carlo Experiments

In order to investigate the accuracy of the different fitting methods and to test the reliability of the errors estimated in the last sections some Monte Carlo simulations have been performed.

For this purpose two sets of simulated catalogues are constructed as follows. First a *uniform* distribution of points is generated in redshift space. The optical luminosity function, given in Table 6.2, is then employed and a total number of 1000 points are drawn from it. For any point (galaxy) with a given absolute magnitude taken randomly from this sample I calculate the corresponding apparent magnitude, using the simulated redshift distribution. Three separate fields are constructed to form the first of the two pseudo–catalogues, catalogue A, and the apparent magnitude limits of the fields are taken to be equal to the observed completeness limits of the AARS fields. The number of points (galaxies) in each of the simulated fields is constrained to correspond to the observed number of galaxies brighter than the magnitude limits of the AARS fields.

The second pseudo–catalogue, catalogue B, is constructed as for catalogue A with the only difference being that its *redshift distribution follows the observed AARS redshift distribution* with non–uniformities and clusters of the same scale. For both pseudo–catalogues two different simulations are performed with the results listed in Table 6.3 and explained below:

Simulation set 1– Galaxies in the simulated catalogue were drawn from the *traditional* luminosity function. The *traditional* method was then applied on the simulated catalogue and the luminosity function parameters were found. A total of 200 simulations were carried out and the mean and standard deviation in M^*, α and ϕ^* were calculated.

Simulation set 2– Galaxies in the simulated catalogue were drawn from the *cluster–free* luminosity function. The *cluster–free* fitting method was then applied on the simulated catalogue and the luminosity function parameters were found. After 200 simulations the mean and standard deviations in M^* and α were calculated.

In both sets of simulations the resulting luminosity function parameters form a Gaussian distribution. It is clear from Table 6.3 that simulation set 1 has a smaller standard deviation. This supports the suggestion in section 6.5.1 that *the luminosity function parameters from the traditional method have smaller apparent errors than the cluster–free fitting procedure.* The estimated errors in this section also agree fairly closely with those from the 1σ error contours and the Jackknife estimates as determined earlier (Table 6.2).

Considering catalogue A (the uniform case), results from Table 6.3 suggest that the differences between the input luminosity function parameters and the final simulated results are smaller than their standard deviations implying that both the luminosity function fitting methods (when applied to a uniform sample) are unbiased. For example, considering the cluster–free method, a difference of only $|dM^*| = 0.13$ and $|d\alpha| = 0.06$ is found between the best fitting and the mean simulated values. This is however, considerably smaller than the Jackknife

bias of $|dM^*| = 0.50$ although the bias estimates in α are close together.

The Monte Carlo simulation results on catalogue B (the non-homogeneous case) reveal that the maximum likelihood method reproduces the correct input parameters for a non–uniform distribution in contrast to the traditional method which produces a flatter α.

The study of the simulated catalogues reveals that although in a uniformly distributed sample the traditional method produces luminosity function parameters with smaller errors, for the degree of clustering observed in the AARS, the maximum likelihood cluster–free fitting method is the correct one to use. The analysis in this section offers two possibilities for the discrepancy between the luminosity function parameters derived from the traditional and cluster–free methods (Table 6.2) and the difference in the errors associated with them (Fig. 6.4). Firstly, the sensitivity of the traditional method to non–uniformities in the galaxian distribution, as present in the AARS, will affect the luminosity function parameters derived from this method. Secondly, the fact that the maximum likelihood fitting technique gives different weights to galaxies of different luminosities affects the error estimates in the luminosity function parameters from this method. Results from the Monte Carlo simulations, listed in Table 6.3, are in agreement with an independent set of simulations carried out by Bean (1983). The Monte Carlo simulation results in this section also appear to support the 1σ errors as quoted in section 6.5.1. These values may therefore be taken as reasonable estimates of the uncertainty in the luminosity function parameters.

Table 6.3

Monte Carlo simulation results.

		input parameters		*simulation results*		
	Method	$M^*_{B_J}$	α	$< M^*_{B_J} >$	$< \alpha >$	$< \phi^* > \times 10^3$
Catalogue A (uniform case)						
Simulation 1	Traditional	−21.42	−1.09	−21.44 ±.16	−1.01 ±.17	0.72 ±.14
Simulation 2	Cluster–free	−21.36	−1.20	−21.49 ±.19	−1.26 ±.22	–
Catalogue B (non-uniform case)						
Simulation 1	Traditional	−21.42	−1.09	−21.50 ±.16	−1.36 ±.13	0.63 ±.14
Simulation 2	Cluster–free	−21.36	−1.20	−21.34 ±.17	−1.12 ±.19	–

6.6 The Infrared Luminosity Function from an Optically Selected Sample

A complete infrared sample was constructed in section 6.3 by excluding 30% of galaxies from the original optically selected survey. This substantially reduces the size of the sample and here I explore the possibility of developing a method for deriving the AARS infrared luminosity function using all the galaxies in the sample observed at UKIRT.

One could approach this problem by estimating a completeness function (in terms of $K(2.2\ \mu m)$, optical–ir colours and redshifts e.g. $\psi\ (K, B-K, Z)$) for the entire sample and to establish the infrared luminosity function by allowing for the effects of this completeness function. A similar procedure has been employed by Sandage et al (1979). Using an analytical form for their completeness function they correct the Shapley–Ames catalogue for incompleteness and construct the 'field' luminosity function. There are, however, two basic problems in applying Sandage et al's method to the AARS infrared sample. Firstly, one has to assume a shape (which is rather arbitrary) for the completeness function and the final answer may well depend strongly on the adopted function. Secondly, their method, when applied to the AARS, makes no use of the completeness of the data in the optical waveband.

To tackle this problem a new technique is constructed in this section. In the following discussion I present the method for two cases:

a. The galaxies are distributed homogeneously,

b. The non–homogeneous case.

The method will then be applied on the AARS and the results from the two cases will be compared in the next section.

a. The homogeneous case

Consider the distribution of observed quantities M_K, M_B and μ (distance modulus) as $n(M_K, M_B, \mu)$. The link between the observed distribution $n(M_K, M_B, \mu)$ and the bivariate luminosity function $\Phi(M_K, M_B)$ in unit solid angle is

$$n(M_K, M_B, \mu)\, dM_B\, dM_K\, d\mu = \Phi(M_K, M_B)\, 10^{0.6\mu}\, \Theta(B_{lim} - B)\, dM_B\, dM_K\, d\mu \qquad 6.31$$

where

$n(M_K, M_B, \mu)$ = number of galaxies in the interval $dM_K\ dM_B$, in the distance modulus bin μ to $\mu + d\mu$.

$\Phi(M_K, M_B)$ = number of galaxies in the interval $dM_K\ dM_B$ per unit volume

$\mu = B - M_B$ distance modulus

$\Theta(B_{lim} - B)$ = selection function

$$\Theta(x) = \begin{cases} 1 & \text{if } x \geq 0 \\ 0 & \text{if } x < 0 \end{cases}$$

Integrating equation 6.31 over μ gives the number of galaxies in each $dM_K\ dM_B$ bin, down to the apparent magnitude limit (B_{lim}) of the sample, $n(M_K, M_B)$. Therefore,

$$n(M_K, M_B)\, dM_K\, dM_B = \int_{-\infty}^{\mu_{lim}=B_{lim}-M_B} n(M_K, M_B, \mu)\, d\mu\, dM_K\, dM_B \qquad 6.32$$

Substituting 6.31 into this relation gives

$$n(M_K, M_B)\, dM_K\, dM_B = \Phi(M_K, M_B)\, 10^{0.6(B_{lim}-M_B)}\, dM_K\, dM_B \qquad 6.33$$

or

$$\Phi(M_K, M_B)\, dM_K\, dM_B = n(M_K, M_B)\, 10^{-0.6(B_{lim}-M_B)}\, dM_K\, dM_B \qquad 6.34$$

By integrating equation 6.34 over dM_B one gets

$$\Phi(M_K)\, dM_K = \int_{-\infty}^{\infty} \Phi(M_K, M_B)\, dM_K\, dM_B = \int_{-\infty}^{\infty} n(M_K, M_B)\, 10^{-0.6(B_{lim}-M_B)}\, dM_K\, dM_B \qquad 6.35$$

It is known that for unit solid angle the volume corresponding to a given M_B at the magnitude limit of the sample B_{lim}, is

$$V(B_{lim}, M_B) \propto 10^{0.6(B_{lim}-M_B)} \qquad 6.36$$

Therefore, equation 6.35 can be re–written as

$$\Phi(M_K)\, dM_K = \int_{-\infty}^{\infty} \frac{n(M_K, M_B)}{V(B_{lim}, M_B)}\, dM_K\, dM_B \qquad 6.37$$

Let N_J be the number of galaxies in a given $dM_B\, dM_K$ bin, then

$$n(M_K, M_B)\, dM_K\, dM_B = \sum_{i=1}^{N_J} \delta(M_B - M_B^i, M_K - M_K^i) \qquad 6.38$$

where

$$\delta(M_B - M_B^i, M_K - M_K^i) = \begin{cases} 1 & \text{if } M_B - M_B^i \approx M_K - M_K^i \\ 0 & \text{if } M_B - M_B^i \not\approx M_K - M_K^i \end{cases} \qquad 6.39$$

Equation 6.38 gives the total number of galaxies in each $dM_K\, dM_B$ bin. Therefore,

$$\int_{-\infty}^{\infty} n(M_K, M_B)\, dM_B = \textit{Total number of galaxies in a given } M_K \textit{ bin} \qquad 6.40$$

and the infrared luminosity function (eq. 6.37), $\Phi(M_K)\, dM_K$, becomes

$$\Phi(M_K)\, dM_K = \frac{n(M_K)\, dM_K}{V(B_{lim}, M_B)} \qquad 6.41$$

The above calculations are best illustrated on a plot of M_K versus M_B (Figure 6.5). If for a given galaxy with optical and infrared absolute magnitudes M_B^i and M_K^i, $|M_B - M_B^i|$ and $|M_K - M_K^i|$ values become less than the bin widths dM_B and dM_K respectively, that galaxy lies in the $dM_K\, dM_B$ bin (see also 6.39). Therefore, equation 6.37 can be reduced to

$$\Phi(M_K)\, dM_K = \sum_{i=1}^{N_{M_K}} \frac{1}{V(B_{lim}, M_B^i(Z))} \qquad 6.42$$

where N_{M_K} is the number of galaxies in each M_K bin. Equation 6.42 gives the differential infrared luminosity function derived directly from an optically selected sample. When applied to the AARS, relativistic volumes must be calculated from the optical magnitudes (section 6.2.2) together with the appropriate K–corrections from chapter 3.

To visualise the method consider again Figure 6.5. The line with unit slope, corresponding to a $B_J - K = 0$ colour, is also plotted. The horizontal separation of individual galaxies from this line indicates their observed $B_J - K$ colours. Since the sample is complete in B_J, all the galaxies (down to the optical magnitude limit of the sample) in a given M_{B_J} bin have been observed. The optical luminosity function, $\Phi(M_{B_J})\, dM_{B_J}$, derived at a given $< M_{B_J}\ M_K >$ mesh point therefore corresponds to its infrared counterpart, $\Phi(M_K)\, dM_K$, through the mean $< B_J - K >$ colours of galaxies at that point. The infrared luminosity function is hence found by calculating the contribution of individual galaxies at different $dM_{B_J}\, dM_K$ squares and summing them up over the M_{B_J} bins. Repeating this procedure for each M_K bin gives the final infrared luminosity function from the B_J selected sample.

In order to apply this method to the AARS I first find the M_K distribution for all the galaxies in the complete optical survey. The optical data must then be employed together with the appropriate K–corrections to calculate the relativistic volume enclosed by a galaxy and hence the contribution from that galaxy to the general luminosity function. The sum of these contributions in each M_K bin gives the infrared luminosity function according to equation 6.42. This procedure is very insensitive to uncertainties caused by the K–term. The redshift–correction in the optical magnitudes does not shift the galaxies across the M_K bins (it only moves galaxies in Figure 6.5 horizontally) and therefore will not affect the number of galaxies per unit volume in these bins. Furthermore, the infrared K–correction is too small to move most galaxies across the M_K bins.

Figure 6.5

M_{B_J} versus M_K for all the AARS galaxies (E-SO *; Spiral o). Solid line indicates the locus of galaxies with $B_J - K = 0$.

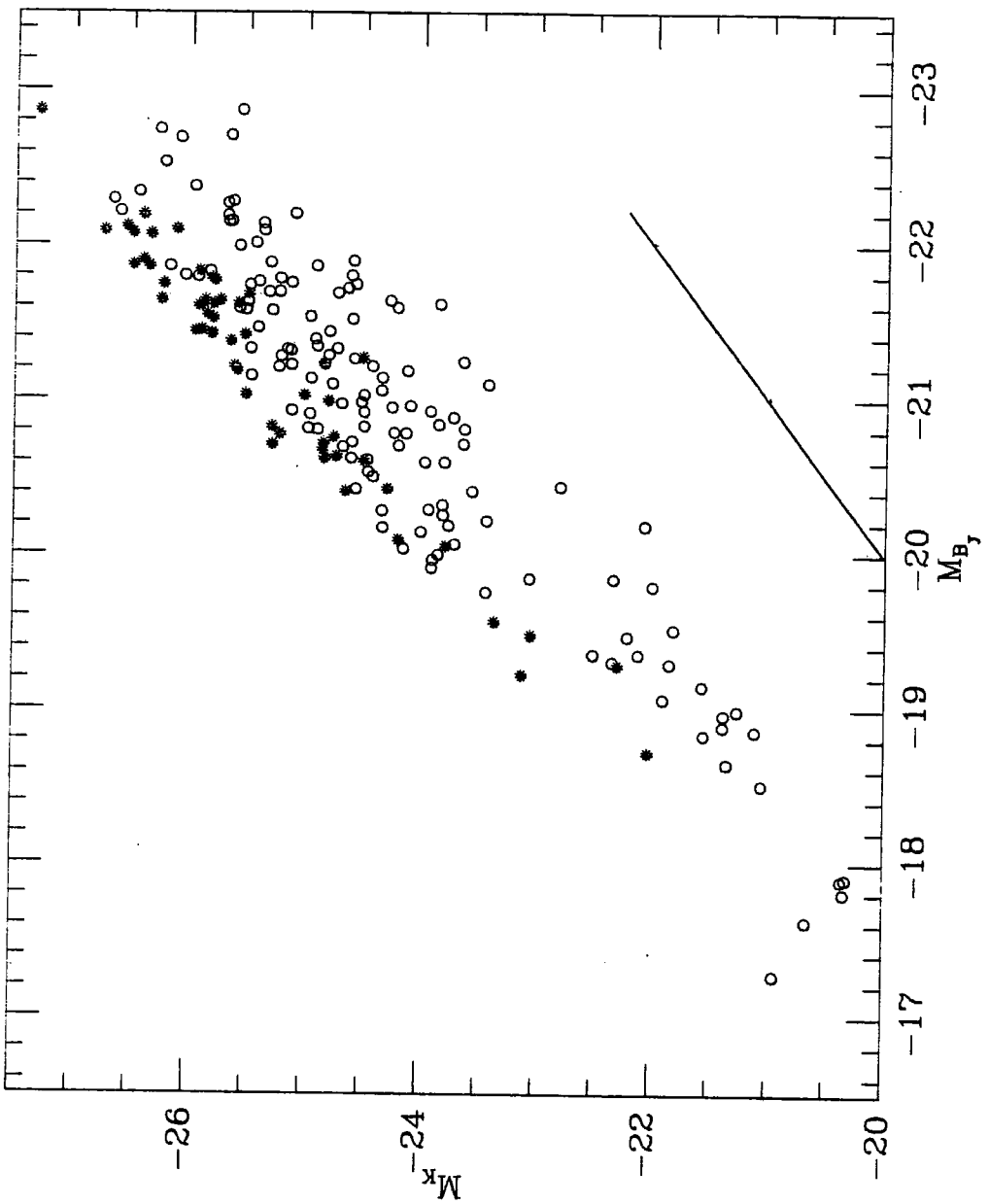

b. The sample is non–homogeneous

It is also possible to extract from the optically selected sample the infrared luminosity function without the assumption of homogeneity. The distribution of galaxies in such a sample can be written as

$$n(M_K, M_B, \mu) dM_K dM_B d\mu = \Phi(M_K, M_B)\, \rho(\mu)\, 10^{0.6\mu}\, \Theta(B_{lim} - B)\, dM_K\, dM_B\, d\mu \qquad 6.43$$

This is a generalisation of equation 6.31 with $\rho(\mu)$ being the number density of galaxies at distance modulus μ. Integrating this equation over μ gives

$$n(M_K, M_B)\, dM_K\, dM_B = \int_{-\infty}^{\mu_{lim}=B_{lim}-M_B} \Phi(M_K, M_B) \rho(\mu) 10^{0.6\mu}\, d\mu\, dM_K\, dM_B \qquad 6.44$$

Taking $D(\mu) = \rho(\mu)\, dex(0.6\mu)$, equation 6.44 transforms to

$$\Phi(M_K, M_B)\, dM_K\, dM_B = \frac{n(M_K, M_B)\, dM_K\, dM_B}{\int_{-\infty}^{\mu_{lim}=B_{lim}-M_B} D(\mu)\, d\mu} \qquad 6.45$$

Now, integrating equation 6.45 over dM_B gives the infrared luminosity function as

$$\Phi(M_K)\, dM_K = \int_{-\infty}^{\infty} \frac{n(M_K, M_B)\, dM_K\, dM_B}{\int_{-\infty}^{\mu_{lim}=B_{lim}-M_B} D(\mu)\, d\mu} \qquad 6.46$$

To calculate the infrared luminosity function from equation 6.46 it is necessary to find the shape of $D(\mu)$. For this purpose I use the optical survey to find the parametric form of $D(\mu)$ as follows:

$$n(M_B, \mu)\, dM_B\, d\mu = \Phi(M_B)\, D(\mu)\, \Theta(B_{lim} - B)\, dM_B\, d\mu \qquad 6.47$$

where $n(M_B, \mu)$ is the number of galaxies in an M_B bin with a distance modulus in the range μ to $\mu + d\mu$. Integrating equation 6.47 over μ gives

$$\int_{-\infty}^{\mu_{lim}=B_{lim}-M_B} \frac{n(M_B, \mu)}{\Phi(M_B)}\, d\mu\, dM_B = \int_{-\infty}^{\mu_{lim}=B_{lim}-M_B} D(\mu)\, d\mu\, dM_B \qquad 6.48$$

Therefore,

$$\int_{-\infty}^{\mu_{lim}=B_{lim}-M_B} D(\mu)\, d\mu = \frac{n(M_B)}{\Phi(M_B)} \qquad 6.49$$

where $n(M_B)dM_B$ is the number of galaxies in a given M_B bin and $\Phi(M_B)\, dM_B$ is its corresponding luminosity function. Substituting equation 6.49 into 6.46 gives the infrared luminosity function as

$$\Phi(M_K)\, dM_K = \sum_{i=1}^{N_{M_K}} \frac{1}{V_i} \qquad 6.50$$

where $1/V_i = \Phi(M_B^i)/n(M_B^i)$ is the ratio of the blue luminosity function to the number of galaxies in a given (M_B^i) bin. This method does not give the normalisation of the luminosity function.

In order to apply this technique to the observed data the ratios $\Phi(M_B^i)/n(M_B^i)$ are calculated for each M_B bin and assigned to all the galaxies (in the optically complete sample) in that bin. The M_K distribution is then used together with these estimates to calculate the sum of $(\Phi(M_B)/n(M_B))_i$ values in each M_K bin, which is equivalent to the infrared luminosity function according to equation 6.50.

This procedure has the disadvantage that it will be affected by the scatter in the mean $\Phi(M_B^i)/n(M_B^i)$ ratios assigned to all the galaxies in a given M_B^i bin. The estimated mean contribution of galaxies in that bin to the general infrared luminosity function will then become uncertain. For this reason I use the inhomogeneity–corrected infrared luminosity function, derived in the next section, only to investigate the sensitivity of the shape of the luminosity function to clustering in the galaxian distribution and will not attempt to carry out an independent analytical fit to it.

6.7 Results from the Complete Optical Survey

A statistical method was developed in the last section to find the infrared luminosity function from a complete optically selected sample. Here I apply this technique to the AARS to establish the infrared luminosity function from all the galaxies in the original optical survey. Employing all the available data I also investigate the effects of inhomogeneities and clustering on the shape of the infrared luminosity function of the AARS.

The infrared luminosity function is presented in Figure 6.6. Error bars correspond to the square root of the number of galaxies in each M_K bin. The traditional fitting method (section 6.2.2) is then applied over a range of $-26.5 < M_K < -22.0$ to derive the infrared luminosity function parameters which best fit the data. The parameters are found to be $M_K^* = -25.19 \pm .15$ mag. and $\alpha = -0.90 \pm .10$ and the resulting luminosity function is shown by solid line in Figure 6.6.

The luminosity function presented in Figure 6.6 is then compared with that corrected for inhomogeneities (Figure 6.7). The latter luminosity function is normalised to produce the same number of galaxies per unit volume at $M_K = -25$ mag. There is clearly a difference between the two luminosity functions which is more pronounced at the bright end. Moreover, the analytical function drawn on Figure 6.6 does not give a satisfactory fit to the cluster–free luminosity function (when normalised accordingly). This implies that the presence of inhomogeneities in the AARS seriously affect the shape of the luminosity function derived from it and therefore a correction for this effect is essential.

The next section gives a summary of the results in terms of the infrared luminosity function parameters for subsequent use in the rest of the studies in this chapter.

Figure 6.6

Infrared luminosity function from all the galaxies in the original optically selected survey. Error bars correspond to the square root of the number of galaxies in a given M_K bin. Solid line indicates the fit to the data (see the text for details).

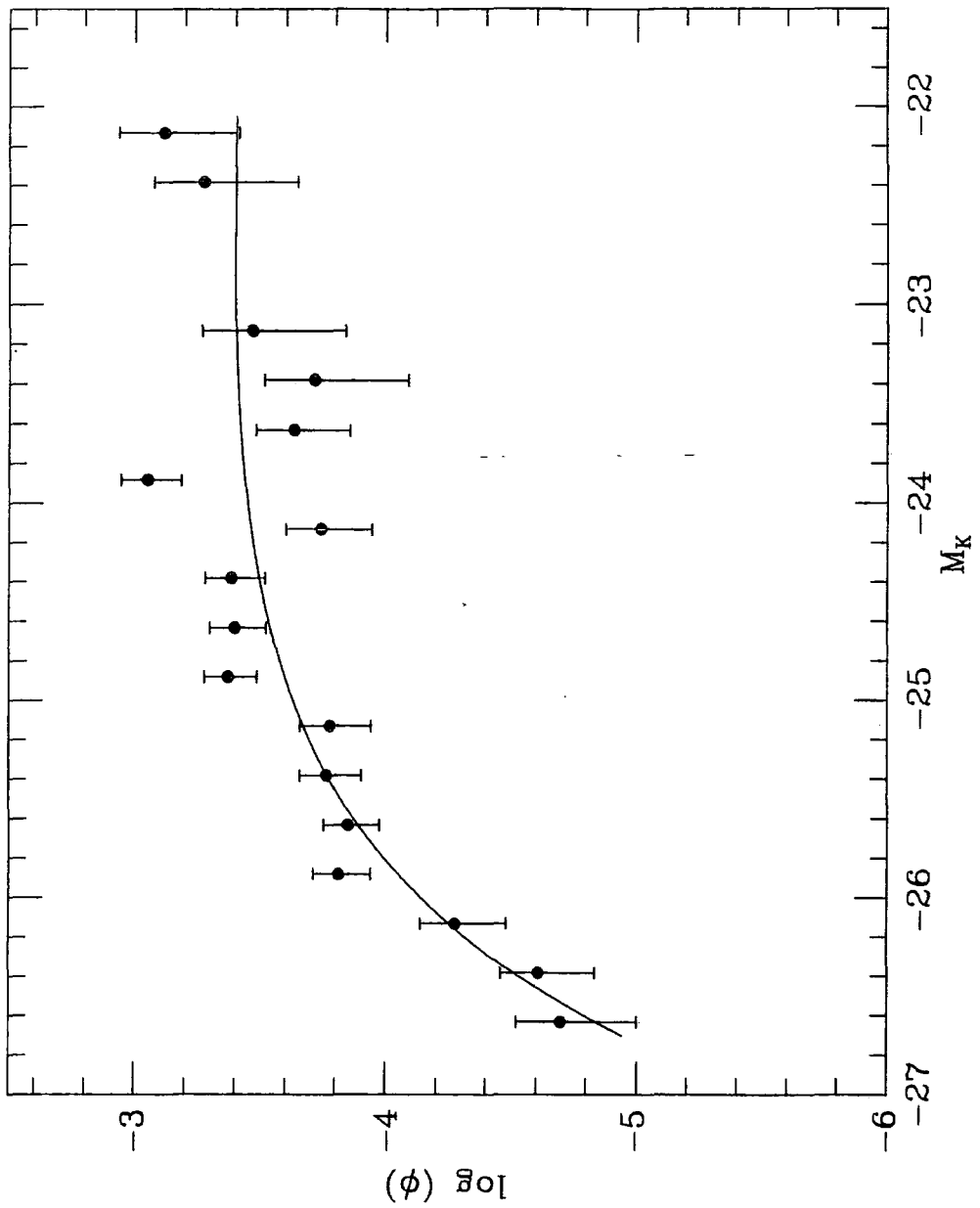

Figure 6.7

The luminosity function in Figure 6.6 (⊙) is compared with that corrected for inhomogeneities (■).

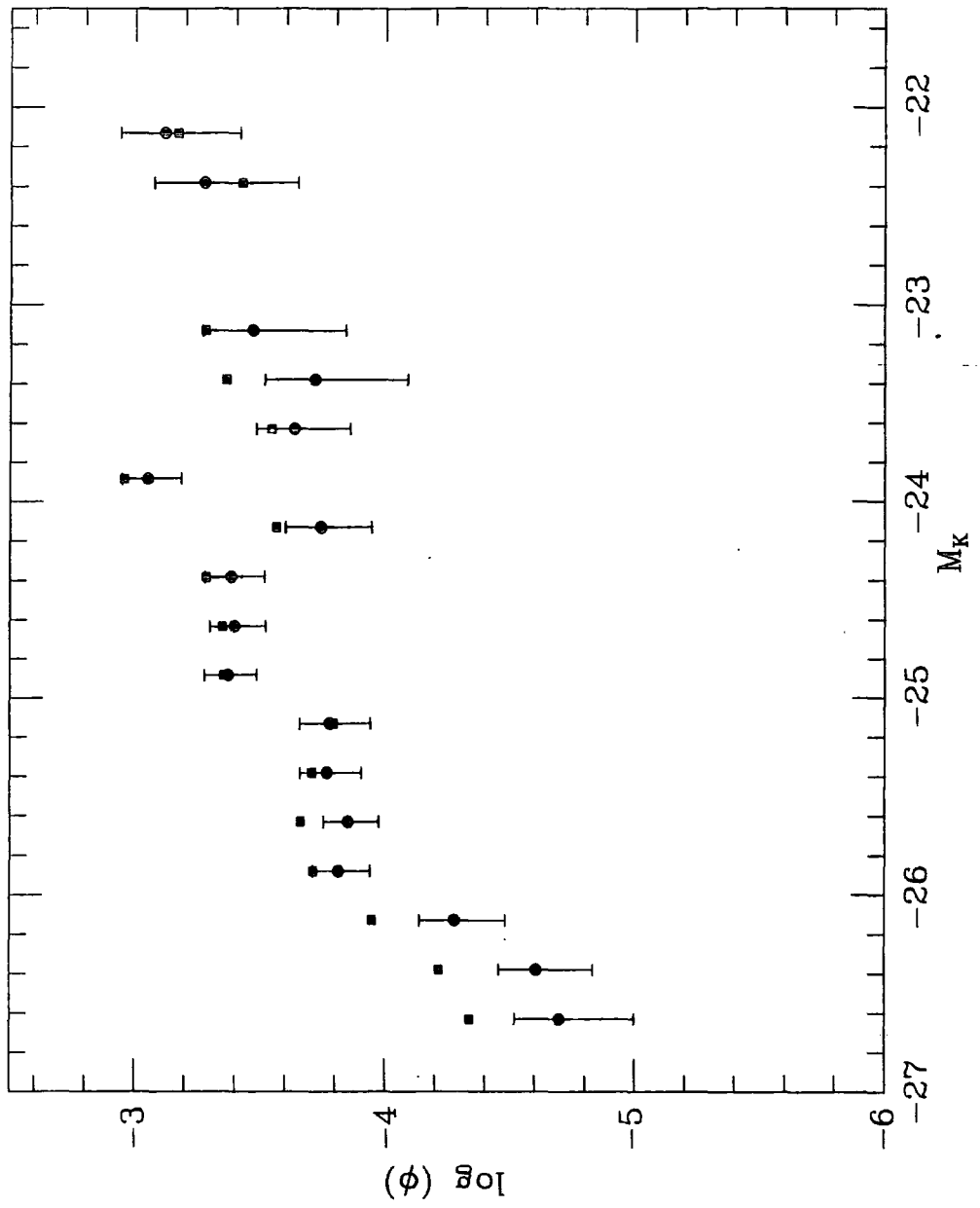

6.8 Discussion

Results from the Monte Carlo simulations, performed in section 6.5.3, indicate that both the traditional and cluster–free methods, when applied to a homogeneous distribution, reproduce the input M^* and α values fairly well. Considering a non–homogeneous sample, as strongly clustered as the AARS, it was found that the traditional fitting method does not reproduce the input parameters whereas the maximum likelihood method does. The simulations also confirmed that the luminosity function parameters from the traditional method have a misleading smaller standard deviation than the cluster–free method.

A direct comparison between the AARS infrared luminosity function parameters from the two methods is difficult due to a correlation between M^* and α. To overcome this problem one could fix α to -1 and calculate the corresponding M^* values from each method. This can then be considered as the only free–parameter in the luminosity function.

The slopes of the error contours in Figure 6.4 are used to derive the relation between M^* at a given α (M^*_α) and at $\alpha = -1$ ($M^*_{\alpha=-1}$). It is clear that these slopes for the traditional and cluster–free methods are not the same, implying that their corresponding relations will also be different. The following relations are derived for each method:

$$\begin{aligned} M^*_{\alpha=-1} &= M^*_\alpha + (|\alpha| - 1) \qquad cluster - free \\ M^*_{\alpha=-1} &= M^*_\alpha + 0.5(|\alpha| - 1) \qquad traditional \end{aligned} \tag{6.51}$$

The M^* values at $\alpha = -1$ are calculated from the above relations and listed in the footnote to Table 6.2. Applying equations 6.51 to the simulation results indicate that $M^*_{\alpha=-1}$ values from the maximum likelihood fitting method change from -21.23 ± 0.19 for a uniform distribution to -21.21 ± 0.17 for a non–uniform sample. Considering the traditional method however, the $M^*_{\alpha=-1}$ values become -21.44 ± 0.16 and -21.32 ± 0.16 for a uniform and non–uniform distribution respectively.

It is important to estimate the degree of clustering in the AARS and its significance for the luminosity function parameters presented in Table 6.2. It was shown in Figure 6.7 (using all the AARS galaxies in the complete optical survey) that the shape of the AARS infrared luminosity function is sensitive to the inhomogeneities in this sample. Excluding the most clustered field (N2) from the AARS optical sample and using the remaining 132 galaxies, the luminosity function parameters were re–calculated (I only use the optical survey for this purpose because it is more stable to this test). Employing the traditional method I find $M^*_{B_J} = -21.72$ mag. and $\alpha = -1.23$ whereas the cluster–free method gives $M^*_{B_J} = -21.46$ mag. and $\alpha = -1.20$. A comparison between these results and the estimates in Table 6.2 (based on all the fields) reveals that the traditional method estimates for $M^*_{B_J}$ and α change by 0.30 mag. and 0.14 respectively. However, considering the cluster–free method, $M^*_{B_J}$ changes by 0.10 mag. and α remains the same. This test confirms again that the cluster–free fitting method is relatively insensitive to non–uniformities in the galaxian distribution.

Using the statistical methods developed in section 6.6 it was shown that the bright end of the AARS infrared luminosity function, when employing all the

galaxies in the optically complete sample, is sensitive to non–uniformities in the galaxian distribution. The results from the traditional method fit to the entire sample (section 6.7) are therefore affected by these non–uniformities and are uncertain. At the other hand, applying the maximum likelihood fitting technique to the infrared luminosity function derived from the entire optically selected sample (Fig. 6.7), weights galaxies according to their luminosities and therefore galaxies with too blue or too red optical–ir colours will be given different weights. This problem is most serious at the bright end of the infrared luminosity function and may bias the parameters derived from the cluster–free fitting method.

Regarding the above discussion and the degree of clustering in the AARS, the cluster–free luminosity function (from Table 6.2) is therefore adopted as the best estimate despite its larger standard errors. The final infrared and optical (based on aperture magnitudes) luminosity function parameters and their associated 1σ errors are therefore

$$M_K^* = -25.26 \pm .27 \qquad \alpha = -1.43 \pm .25$$
$$M_{B_J}^* = -21.36 \pm .17 \qquad \alpha = -1.20 \pm .22$$

These values will be used to predict the number–magnitude counts in the subsequent studies in this chapter.

A direct comparison between the optical and infrared luminosity function parameters is not straightforward at this stage. The difference in the M^* values (reduced to $\alpha = -1$) between the two wavelengths is 3.67 mag. which roughly corresponds to the mean $B_J - K$ colour of the AARS galaxies. However, an accurate comparison is hampered because of the morphological type dependence of the optical–ir colours. Therefore, prior to any such comparison one should first disentangle the morphological type and wavelength dependence of the AARS luminosity function parameters. This point is the subject of the next section.

6.9 Morphological Type Dependence of the Infrared Luminosity Function

Any type–dependence of the luminosity function of galaxies would be of great interest in galaxy formation theories. For example, comparing the luminosity distributions for different types of spirals provides information regarding spiral structure as a function of total luminosity. It also provides further details about the correlation between luminosity class (Van den Bergh 1960) and absolute magnitudes for spirals (Sandage and Tammann 1974).

The data presented in this thesis can be employed to examine whether the morphological type–dependence of the optical luminosity function (Sandage, Binggeli and Tammann 1985) disappears in the infrared wavebands. This might be expected following the discussion in chapter 3 where it was shown that at infrared wavelengths the stellar populations of galaxies along the Hubble sequence are similar. After studying this type–dependence, a direct comparison between the optical and infrared 'field' luminosity functions becomes possible.

Unfortunately, the number of AARS galaxies in each morphological type bin is rather small for establishing the luminosity function for each class of galaxies. Therefore, I adopt an indirect approach and study analytic fits to the absolute magnitude distributions (not corrected for volume) for different morphological types (c.f. Ellis 1982).

The AARS galaxies brighter than the magnitude limits in the optical and infrared surveys are employed and their M_{B_J} and M_K distributions as a function of morphological type are plotted in Figure 6.8. The sample is divided into two broad morphological type bins; E-SOs and spirals. Solid lines show the predicted distributions which are calculated from a Schechter luminosity function; taking $\alpha = -1$ and estimating the M^* value which best fits the observed distribution. The predicted distributions are normalised to produce the observed total number of galaxies in the complete sample. The estimated values for M^* (at $\alpha = -1$) and their associated errors are indicated on Figure 6.8.

Firstly, the estimated M^* values for E-SOs are brighter than spirals by 0.50 mag. and 0.70 mag. in the optical and infrared wavebands respectively. Therefore, it appears that the infrared luminosity function is also type–dependent. Secondly, comparing the optical and infrared luminosity distributions for individual types separately I find that for E-SOs; $(M^*_{B_J} - M^*_K) = 3.8$ mag. and for spirals; $(M^*_{B_J} - M^*_K) = 3.6$ mag. These values are in excellent agreement with the mean $< B_J - K >$ colours of E-SO and spiral galaxies as listed in Table 4.1 (after allowing for the colour–luminosity relation). This implies that the infrared luminosity function is essentially identical to that in optical waveband, shifted by the mean optical–ir colour.

It is known that a substantial fraction of the infrared light of spirals comes from their bulges. Therefore, one can conclude that the elliptical galaxies and bulges of spirals have had different formation or evolutionary histories (see also King and Ellis 1983; Sandage, Binggeli and Tammann 1985). Alternatively, the difference in the M^*_K values between E-SOs and spirals can be attributed to different mass distributions (assuming constant mass–to–infrared luminosity ratio for galaxies of all types). In this case, fainter M^*_K for spirals is due to a

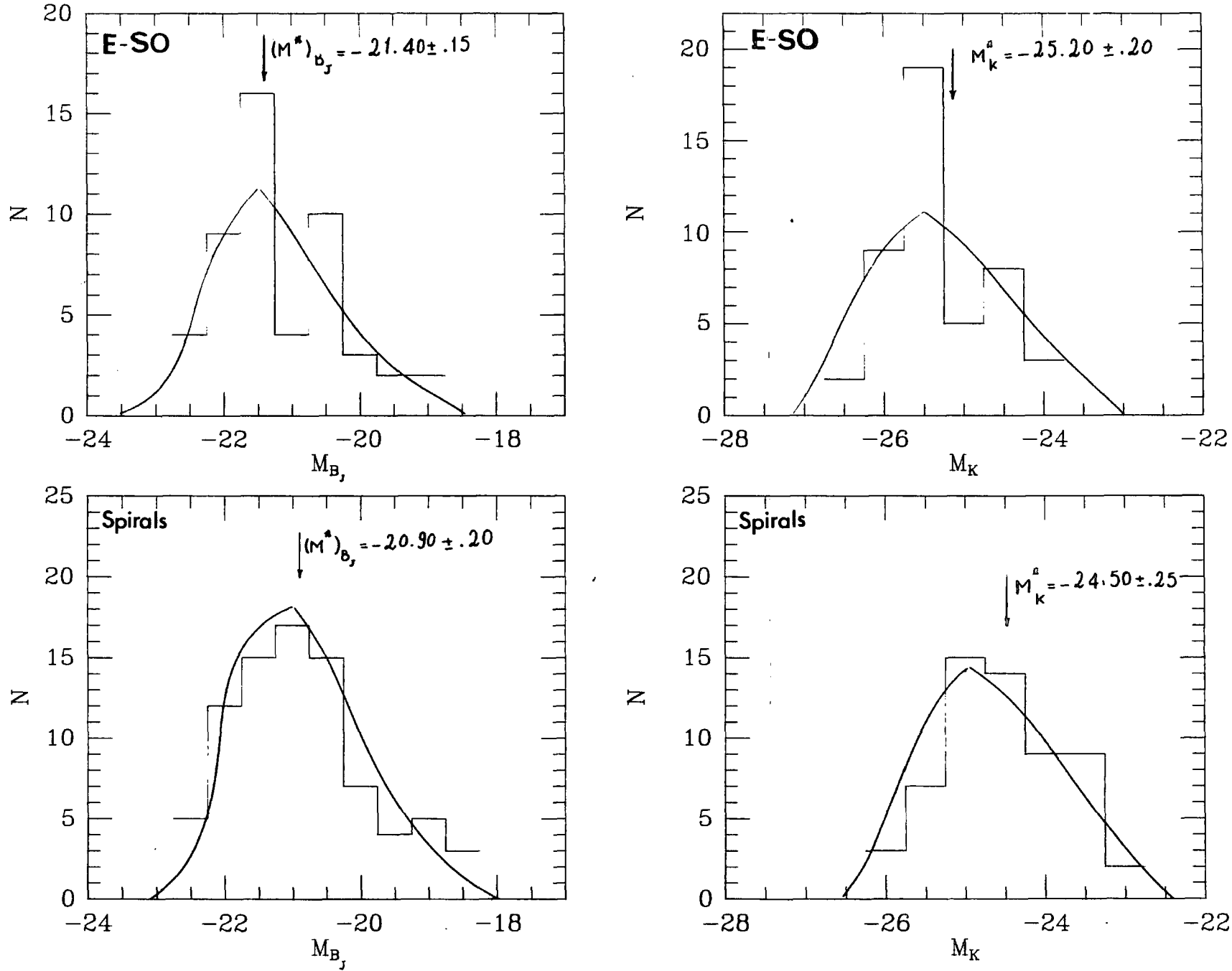
E-SO
$(M^*)_{B_J} = -21.40 \pm .15$
N
M_{B_J}
E-SO
$M_K^* = -25.20 \pm .20$
N
M_K
Spirals
$(M^*)_{B_J} = -20.90 \pm .20$
N
M_{B_J}
Spirals
$M_K^* = -24.50 \pm .25$
N
M_K

Figure 6.8

fraction of their mass being used for disk formation. The difference between the optical luminosity functions in spirals and E-SOs is almost certainly due to the star formation in spirals and its relation with the galaxian mass (Tully et al 1982; see also chapter 5 of this thesis).

The analysis in this section also reveals that one can use an optical survey to predict the properties of its infrared counterpart, using the mean optical–ir colour and allowing for its morphological type–dependence. For example, the infrared luminosity density of the Universe can be derived from its optical luminosity density and the mean optical–ir colour once allowance is made for the effect of morphological type mix. Similarly, the ratio of E–to–spirals at 2.2 μm can be predicted by employing the ratio at optical waveband, the appropriate evolutionary correction and the mean optical–ir colours.

The above conclusions are preliminary and can be improved in two obvious ways. Firstly, by increasing the number of galaxies in each morphological type bin (e.g. obtaining infrared magnitudes for the remaining two fields of the original AARS) one would be able to carry out a more rigorous comparison and inter–compare the infrared luminosity functions for different classes of spiral galaxies. Such a study will be important for elucidating possible differences in mass distribution within galaxies along the Hubble sequence. Secondly, by employing 2–D infrared arrays one could construct an infrared selected survey. A direct comparison between the properties of an infrared and optical selected survey will then provide concrete tests of the results in this section. However, the preliminary results from this study suggest that galaxies with strong/weak near–ir emission at 2 μm can not be very common since the magnitude scale in the infrared luminosity function is predictable from its optical counterpart and the mean optical–ir colours.

In a study of the infrared properties of a sample of optically selected faint galaxies, Ellis and Allen (1983) discovered the existence of early–type galaxies with large infrared colours ($J - K > 1.3$ mag.). With regard to the results in this chapter, the strong near–ir emission from these objects is likely to be due to the effect of redshift (implying large distances for them) and not due to any large intrinsic rest infrared flux. This supports the possibility proposed by Ellis and Allen (1983) that the infrared colours could be used as reliable redshift indicators.

An immediate extension of this program would be to obtain infrared measurements for complete samples of galaxies in rich clusters and to construct the cluster luminosity function at 2.2 μm. A comparison between the infrared luminosity functions in 'field' and cluster will then indicate the extent to which the old population in clusters has been affected by dynamical evolution. For example, if the 'field' and cluster infrared luminosity functions (for a given morphological type) were found to be different, the implication would be that the old population in cluster galaxies had been affected by environmental processes or they have had different formation histories. Moreover, a simultaneous study of the optical and infrared luminosity functions of 'field' and cluster galaxies will be helpful for elucidating the evolution of galaxies (e.g. gas loss effects) in rich clusters.

6.10 Number–Magnitude Counts at Infrared Wavelengths

The form of the galaxy number–magnitude ($N(m)$) relation is widely recognised to be a powerful cosmological probe. Galaxy counts have previously been used to study the homogeneity of the galaxy distribution (Hubble 1926) and to carry out detailed tests of world models (Hubble and Tolman 1935). They can also provide an estimate of the normalisation of luminosity functions and enable a calculation of the mean luminosity density of the Universe (Kirshner et al 1978; Bean 1983).

It is well known that at faint limits ($B \approx 24$ mag.) reached by using new techniques, the dependence of $N(m)$ on the cosmological deceleration parameter, q_0, becomes significant (Peebles 1979b). However, at these faint magnitudes the $N(m)$ relation is also sensitive to the rate of galaxy luminosity evolution (Brown and Tinsely 1974). For example, Shanks et al (1984) found strong evidence for luminosity evolution in their blue counts. By extending their counts to red passbands they showed a much less strong sensitivity to luminosity evolution and therefore proposed that a faint ($R \approx 21$ mag.) galaxy redshift survey may be able to separate the effects of luminosity evolution and cosmology in the red counts. This result is supported by deep CCD counts in red magnitudes which appears to maintain the same count–magnitude slope seen at brighter magnitudes (Hall and Mackay 1984).

It seems that a more promising interpretation of the counts at longer wavelengths is possible because they are less affected by the variety of morphological types than in the optical and because the red (and infrared) evolutionary models are better determined. Moreover, the uncertainties caused by redshift effects and patchy absorption are minimal in these wavelengths.

Employing the results from the last sections I now carry out a study of galaxy number–magnitude counts at 2.2 μm. Of course, the AARS is not a deep enough sample to provide information about q_0. Therefore, the attention is mainly restricted to predicting the infrared number–magnitude counts and to estimate the normalisation of the luminosity function.

Infrared number–magnitude counts for the complete AARS sample are presented in Figure 6.9. Apparent magnitude bins are 0.50 mag. wide and error bars correspond to the square root of the number of galaxies in each bin. The $\log N - m$ relation has a slope close to 0.6 which is the value expected if the galaxies are uniformly distributed and redshift effects are small.

Figure 6.10 presents the infrared number–magnitude counts for the complete samples of E-SOs and spirals separately. To demonstrate the trend for spirals and E-SOs more clearly, different apparent magnitude bins are used for different types. The relation for both types is again consistent with a slope of 0.6. In the next section a comparison will be carried out between the observed counts and the number–magnitude count models in order to estimate the normalisation of the luminosity functions and also to compare the space densities of galaxies between the optical and infrared surveys.

Figure 6.9

Infrared number–magnitude counts for the composite (including all types) AARS sample. The line is the model prediction and is normalised to the observed counts at $K = 11.75$ mag.

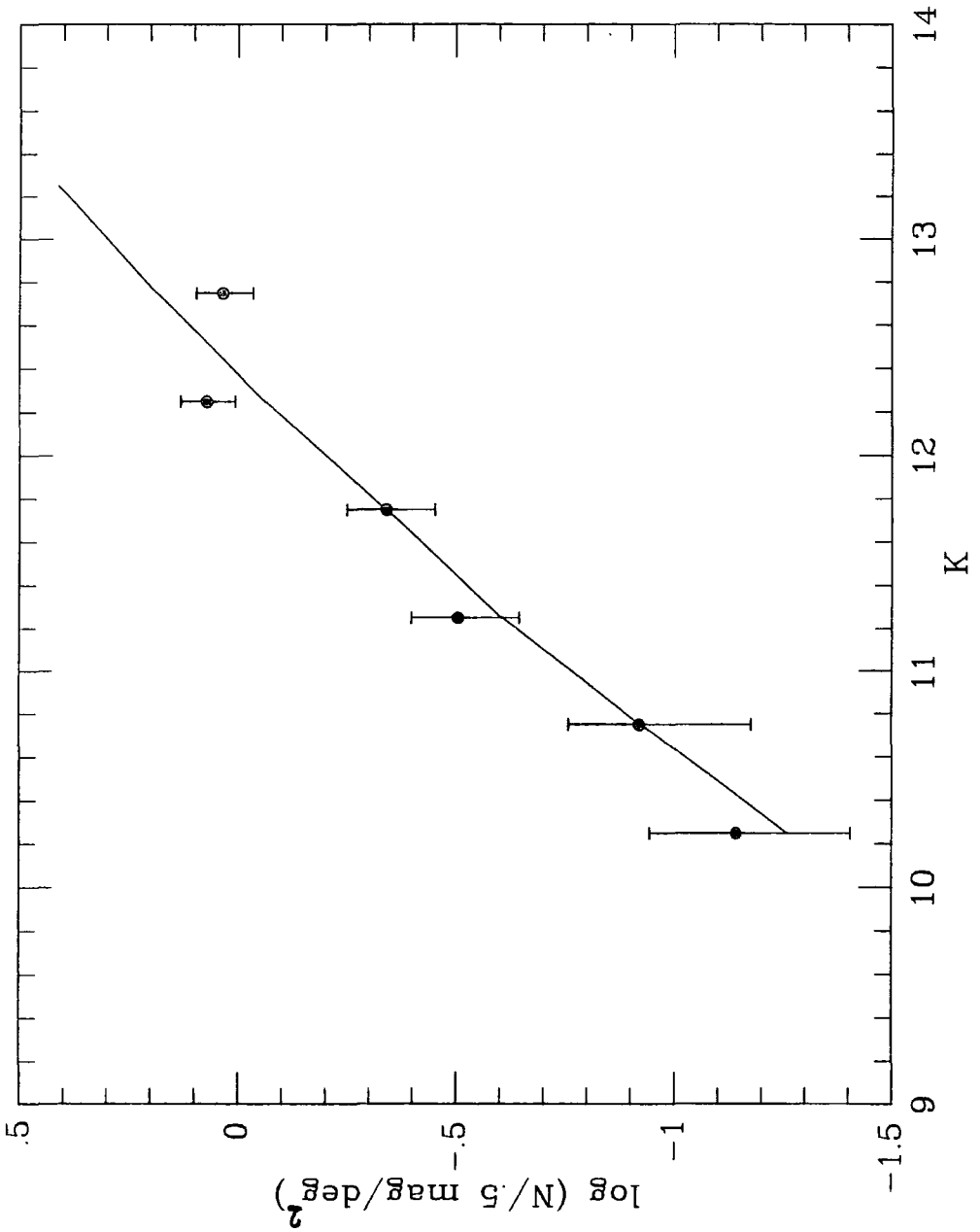

Figure 6.10

The same as Figure 6.9 for E-SOs (⊕) and spirals (×) separately. Solid and dashed lines are model predictions for E-SOs and spirals respectively.

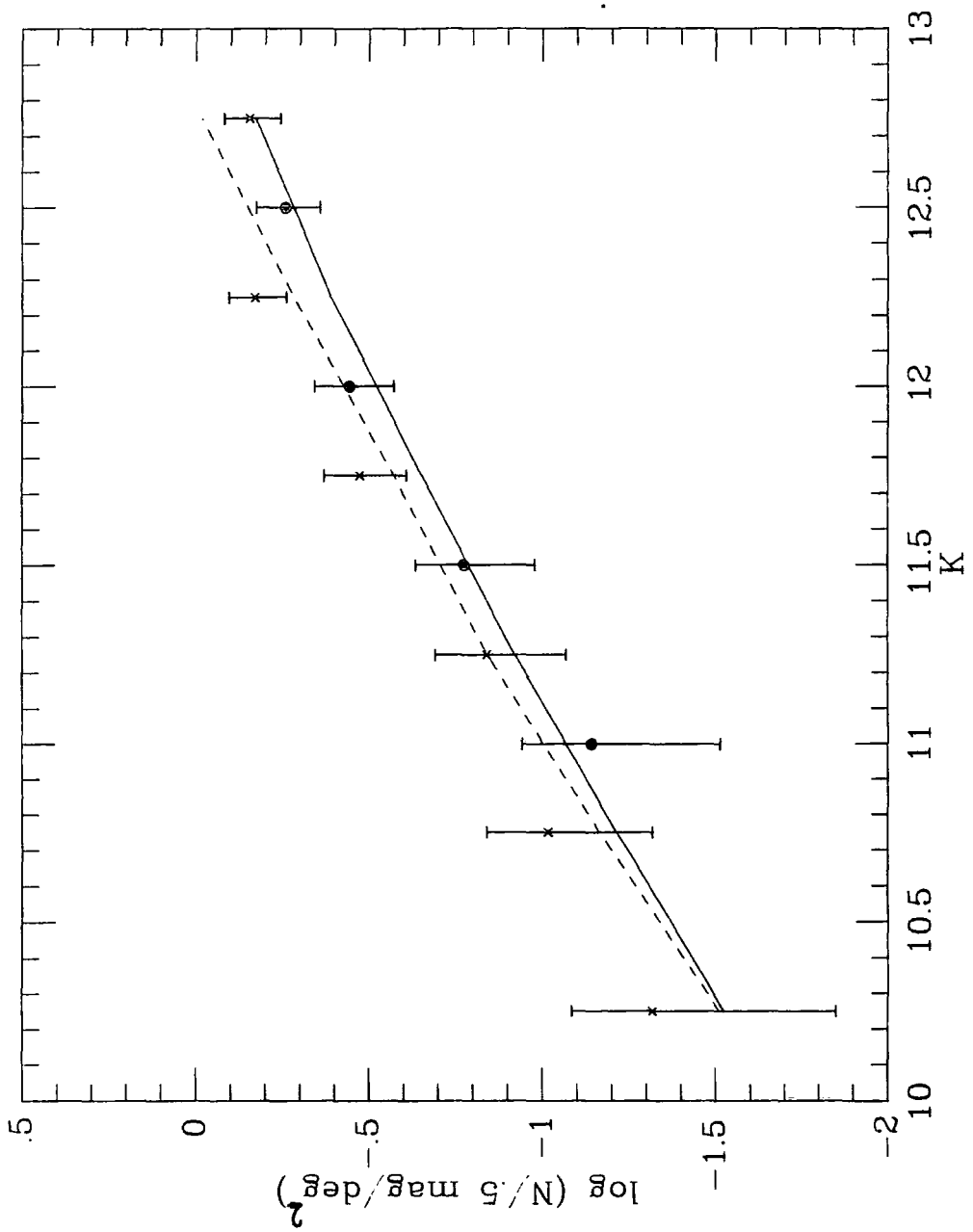

6.10.1 Number–Magnitude Count Models

The theoretical models of the number–magnitude counts are made as follows. The appropriate luminosity function is used to compute the number of galaxies that can be seen in some apparent magnitude interval in the volume associated with a particular redshift shell. By summing over all shells the total number–magnitude counts are computed. At redshift Z, the 'local' galaxy luminosity functions are shifted faintwards to simulate the K–dimming effect. Note that K–corrections at infrared wavelengths are similar for different morphological types, whereas for the purpose of predicting the optical counts, a knowledge of K–corrections as a function of morphological type is essential. In the optical, the fraction of each morphological type of galaxy in the 'field' at some bright magnitude limit is also needed so that the effect of each galaxy type's K–correction on the optical $N(m)$ relation will be correctly weighted. At the depth of the AARS fields the evolutionary effects are assumed to be negligible and hence explicitly neglected in the present models.

The AARS number–magnitude counts at 2.2 μm are constructed using the infrared luminosity function from section 6.8 and the infrared K–corrections from chapter 3. These are then normalised to the observed counts at $K = 11.75$ mag. (Figure 6.9) to estimate ϕ^*. The predicted counts fit the observed $N(m)$ relation fairly well. The bump at $K = 12.25$ mag. is caused by an overdensity in the N2 field and disappears on removing this field. In order to study the reliability of ϕ^*, I estimate it for each of the AARS fields separately. In this case, the observed and predicted counts are adjusted at $K = 12.25$ mag. This magnitude is adopted to be bright enough for all the fields to be complete and yet faint enough to allow a sufficient number of galaxies into the sample. The values of ϕ^* derived from the combined infrared AARS fields and from individual fields separately are listed in Table 6.4. The mean $< \phi^* >$ of the three fields is $(0.71 \pm .14) \times 10^{-3}\ n/Mpc^3$ which agrees closely with $< \phi^* >= (0.66 \pm .12) \times 10^{-3}\ n/Mpc^3$ derived from the traditional method fit to the infrared luminosity function in section 6.4.

I now apply the above analysis to a simulated catalogue in order to estimate the errors in ϕ^* and to study the sensitivity of ϕ^* values to non–uniformities in the AARS fields. A total number of 1000 galaxies was drawn from the infrared luminosity function (section 6.8) and used to construct three different pseudo–catalogues with the same completeness limits and redshift distributions as the AARS fields. The number of galaxies in each simulated catalogue was then fixed to correspond to the total number of galaxies in the complete infrared AARS fields. After 100 simulations the mean values of ϕ^* and their associated errors for individual fields and the combined sample were calculated and are listed in Table 6.4. The simulated results also confirm an overdensity in the N2 field. Considering the errors in the ϕ^* values, however, the N1 and S1 fields appear to have similar number densities.

The optical number–magnitude count model is now constructed, using the blue luminosity function from section 6.8. The mean of the blue K–corrections of all morphological types (section 3.4) is taken and used in this model. The uncertainty caused by this procedure is small since only the models out to a redshift of 0.10 are needed here. At this redshift the correction to blue magnitudes

is less than 0.40 mag. and smaller than the width of the apparent magnitude bins (0.5 mag.) used in the model. Adjusting the observed and predicted counts, the ϕ^* values were estimated for separate fields and all the fields together and are listed in Table 6.4. The simulated pseudo–catalogues were then constructed to resemble the complete optical AARS sample and were used to estimate ϕ^*. The simulated results and their associated errors are listed in Table 6.4 and confirm that the S1 and N1 fields have similar number densities. The overdensity in the N2 field with respect to the other two fields appears to be more pronounced in the optical survey.

Employing the luminosity function parameters for E-SOs and spirals (Figure 6.8) I now predict the number–magnitude count models for different morphological types separately in order to compare the space densities for different types of galaxies in the optical and infrared surveys. The predicted counts are fitted to the observed data in Figure 6.10 and the ϕ^* estimates and their associated errors for E-SOs and spirals are listed in Table 6.5. The errors are estimated from the Monte Carlo simulations.

The results from Table 6.4 imply that the observed number density of galaxies in the N2 field, in both infrared and optical surveys, is larger than the other two fields. The difference is of the order of 2σ and 3σ in the infrared and optical surveys respectively. The simulation results also confirm this conclusion and imply that the difference is almost certainly due to the redshift distributions and existence of a cluster in the N2 field. This also explains the presence of a bump in the infrared counts at $K = 12.25$ mag. since by removing the N2 field the excess density disappears.

Comparing the results from the optical and infrared surveys, it appears that the number densities of S1 and N1 fields are similar. Using all the fields together, I still find a marginally larger number density for the optical survey. This could, perhaps, be explained as a result of the exclusion of blue galaxies fainter than the completeness limit, from the infrared survey.

The number–magnitude counts in Figure 6.10 indicate that in the infrared survey the number density of spirals at $K = 12.5$ mag. is larger than that of E-SOs by about 25%. However, they agree closely at brighter magnitudes ($K \sim 11$ mag.). Since in an infrared selected sample the number of red (early–type) galaxies per unit volume is expected to be larger than in an optical survey, it is difficult to estimate the significance of the above result. Nevertheless, it is of crucial importance in constructing deep infrared number–magnitude count models. Clearly, more infrared data for complete surveys is required to examine this conclusion and also to test the type–dependence of the infrared 'field' luminosity function.

A knowledge of deep number–magnitude counts at 2 μm ($K \sim 18-20$ mag.) will be useful for future studies concerning infrared selected surveys (i.e. surveys constructed by 2–D panoramic detectors). However, an estimate must first be made of the infrared K–corrections at these faint apparent magnitudes (large redshifts). The infrared redshift corrections from chapter 3 cannot be used for this purpose since they are only valid for $Z < 0.10$. Therefore, I estimate these corrections (independent of morphological type) by exploiting the spectral energy

distribution (SED) of a K–star (e.g. αTau) which is known to dominate the stellar population of nearby galaxies at infrared wavelengths. This SED is shifted in redshift steps and at each step is convolved with the response function of the appropriate infrared filter (K filter at 2.2 μm) and its corresponding magnitude is calculated. The difference between the magnitudes at a given redshift and the rest–frame then gives the change in infrared magnitude as a function of redshift. Using this K–correction and the infrared luminosity function parameters from section 6.8, I predict the number–magnitude count models to $K \sim 20$ mag. Note that the infrared K–corrections become morphology–dependent for $Z > 0.50$ (Bruzual 1981). This effect must therefore be taken into account in constructing deep number–magnitude count models at 2.2 μm. Observations of the infrared SEDs for different types of galaxies are required for this purpose and for assessing the synthetic infrared SEDs for galaxies. The assumption of morphological type–independence of the infrared K–corrections for $Z > 0.50$, as adopted in this section, is therefore an oversimplification of the actual problem. The models have been calculated for $q_0 = 0.01, 0.1, 0.5$ and 1, with no evolutionary effects included. They are normalised using the ϕ^* values estimated from the infrared survey (Table 6.4) and are presented in Figure 6.11. These results provide the first deep number–magnitude count predictions at infrared wavelengths and must be compared with the observed counts in future infrared selected surveys. This will be a subject for extensive study with 2–D panoramic infrared detectors.

Table 6.4

Observed and simulated number densities for the AARS fields.

	infrared survey			*optical survey*		
Field	Observed $\phi^* \times 10^3$	simulated $< \phi^* > \times 10^3$	1σ $\times 10^3$	Observed $\phi^* \times 10^3$	simulated $< \phi^* > \times 10^3$	1σ $\times 10^3$
S1	.68	.50	.11	.57	.82	.29
N1	.56	.43	.12	.76	.82	.29
N2	.89	.74	.12	1.48	1.26	.31
All Fields	.62	.59	.12	.90	1.03	.21

Note: ϕ^* is in n/Mpc^3.

Table 6.5

Number densities for different morphological types.
Errors are estimated from the Monte Carlo simulations.

	infrared survey		*optical survey*	
Type	ϕ^* $\times 10^3$	σ $\times 10^3$	ϕ^* $\times 10^3$	σ $\times 10^3$
E-SO	.22	.10	.19	.10
Spirals	.90	.36	.95	.28

Note: ϕ^* is in n/Mpc^3.

Figure 6.11

Deep infrared number–magnitude count predictions ($K \sim 20$ mag.) for $q_0 = 0.01$ (⊖),0.1 (∗),0.5 (×) and 1 (○). Evolutionary effects have not been included in these models.

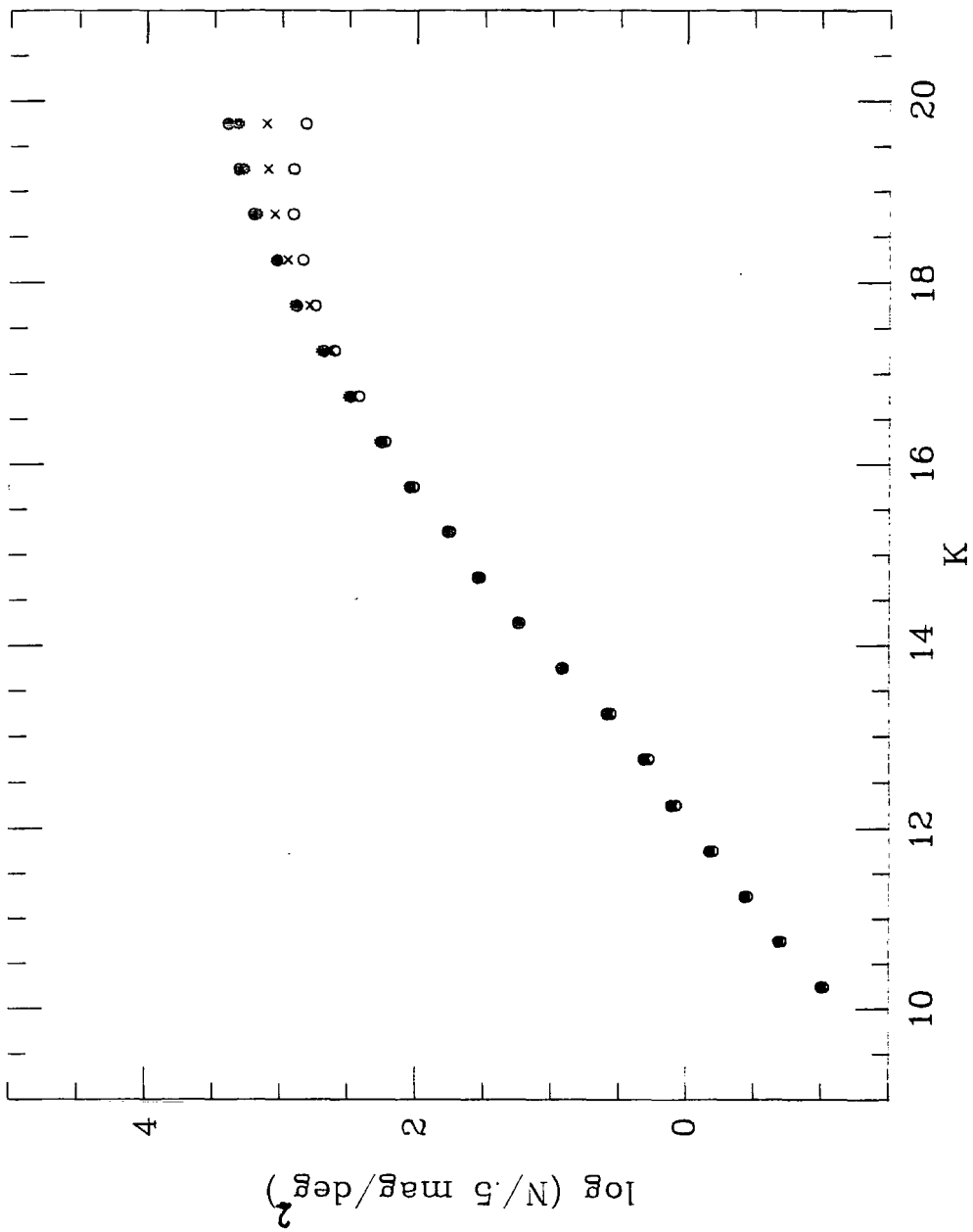

6.11 Summary and Conclusions

A detailed analysis of the infrared luminosity function of 'field' galaxies has been carried out in conjunction with its optical counterpart. A new statistical method has been developed to construct the infrared 'field' luminosity function from a complete optically selected sample. The best estimates for the luminosity function parameters have been used to predict infrared deep number–magnitude counts ($K \sim 18 - 20$ mag.). The main conclusions are summarised as follows:

1. The infrared luminosity function is found to be type–dependent. For a given value of α, the luminosity scale (M_K^*) for E-SOs is brighter than that of the spirals by about 0.70 mag. This implies that the E-SOs and bulges of spirals have different formation or evolutionary histories.

2. The infrared 'field' luminosity function for a given morphological type of galaxies is found to be the same as its optical counterpart shifted by the respective mean optical–ir colour. Therefore, the properties of an infrared survey can be predicted using its optical luminosity function, the mean optical–ir colour and allowing for the morphological type mix in the sample. This supports the idea that galaxies with strong/weak near–ir emission can not be very common.

CHAPTER VII

Summary and Future Prospects

7.1 Summary and Conclusions

The project described in this thesis has investigated the optical and infrared properties of a complete infrared survey of normal galaxies. The redshift range studied is beyond that affected by local velocity perturbations and the survey is expected to be a 'fair' sample of the Universe. The main results from this study are summarised as follows:

1. The optical–infrared and infrared colour–redshift relations of E-SO galaxies can be used successfully to reduce colours and magnitudes to zero redshift. The small scatter in the $(J-K)-Z$ relation ($r.m.s. = 0.04$ mag.) and the fact that for galaxies with redshifts less than unity the $J-K$ colours are not significantly affected by evolution, supports the use of infrared colours as moderately accurate redshift indicator.

   The infrared colour–redshift relations are found to be similar for E-SOs and spirals. This justifies the use of a type–independent K–correction for nearby galaxies of all morphological types.

2. The slopes observed for the optical–infrared and infrared colour–luminosity relations of E-SOs support the conjecture that a single parameter (metallicity) is sufficient to explain the variation in colours of these galaxies at all wavelengths. There is a factor of 10 difference in the mean metallicity of old giants across 5 magnitudes of luminosity in the sample of E-SOs studied here. Using techniques of population synthesis the metallicity range implied is $-.30 < [Fe/H] < .30$ for models with an age of ~ 13 Gyr. and a Salpeter initial mass function (slope $X = 1.35$).

   The existence of a statistically significant $(J-K)-M_K$ relation for E-SOs, does not support the hypothesis proposed by Bothun et al that varying amounts of horizontal branch stars produce the optical colour–luminosity relation for these galaxies.

3. A more effective correlation has been found between metal enrichment and luminosity (steeper $(J-K)-M_K$ and $(B_J-K)-M_K$ relations) for disk galaxies than for the E-SOs. The variation in the mean metallicity of the old disk population is thus larger (by a factor of 4) than that for the spheroidal

systems.

A change is needed in the slope of the IMF of star formation in spirals in order to reproduce their $B_J - K$ colours. Luminous, red spirals ($B_J - K > 3.5$ mag.) are giant dominated ($X = 1.35$) and have a constant metallicity ($[Fe/H] \simeq .30$) but varying ages ($3 < t < 13$ Gyr.). However, blue spirals ($B_J - K < 3.5$ mag.) which are dwarf dominated and hence consistent with a steeper IMF ($X \sim 3$), have lower metallicities ($-2.30 < [Fe/H] < -.30$) and varying ages ($7 < t < 20$ Gyr.).

It is not straightforward to disentangle the effects of age and metallicity in these systems by using infrared and optical–infrared colour indices alone. However, an important result of this study is that a variation in metallicity can also be responsible for changes in the $B_J - K$ colours of disk dominated spirals.

4. The intrinsic scatter in the infrared colour–luminosity relation is small for galaxies of *all* morphological types. This implies a negligible variation in metallicity at a fixed absolute magnitude. In the case of the optical–infrared colours however, a significant intrinsic scatter is found around the colour–luminosity relations for spirals and to a lesser extent for E-SOs. Variations in the residual star formation and bulge–to–disk ratios amongst these galaxies are proposed as likely possibilities. The intrinsic scatter in the optical–infrared colour–luminosity relation of E-SOs is marginal and is most likely due to a difference in the luminosity function of their horizontal branch stars.

   The $(J - K) - K$ relations for E-SO galaxies in the present sample, and the Virgo and Coma clusters agree fairly well though the samples are small. No evidence has been found for an anomalous population of cool stars in the Virgo cluster galaxies and hence the infrared colour–luminosity relation appears to be independent of environment.

   The $J - K$ colours are hardly affected by reddening and the variation in young population amongst the galaxies. Regarding the negligible cosmic scatter in the $(J - K) - M_K$ relation and its apparent universality, the infrared colours could then be considered as potential distance indicators. However, the flat slope (taking colour as independent variable) implies that a 2% accuracy in photometry is needed over a wide luminosity range to achieve cluster distance moduli accurate to .10 mag.

   A relative distance modulus of $3.81 \pm .23$ mag. is derived between the Virgo and Coma clusters, using their E-SO $(J - K) - K$ relation. This value lies in the range of the moduli derived from their redshifts and assuming recent estimates for the infall velocity of the Local group towards the Virgo.

5. A correlation has been found between the residuals around the H surface brightness–M_H and $(B_J - H) - M_H$ relations of spiral galaxies. This relation is demonstrated to be due to a variation in the bulge–to–disk ratios amongst the galaxies. Bulge–to–disk ratio is therefore proposed as a second parameter in the spirals' optical–infrared colour–luminosity relation.

The residuals' relation has been used to correct the optical–infrared colours of spirals for any bulge contamination. This considerably reduces the scatter and also largely removes the morphological type–dependence of the zero–point of their optical–infrared colour–luminosity relation.

The optical–infrared colour–luminosity relation for spiral galaxies in clusters has been examined for environmental effects. Employing a sample of spirals of all types in eight nearby clusters, it has been found that the scatter in the colour–luminosity zero–points between different clusters improves when corrected for the surface brightness (bulge–to–disk ratio) effect. However, there is still evidence for environmental dependence in this relation and an uncertainty of .28 magnitude is estimated in distance moduli derived from this improved optical–infrared colour–luminosity relation. Nevertheless, this relation provides an independent test of distances derived from the infrared Tully–Fisher relation with the advantage that it applies to face–on galaxies. The mean absolute difference between distance moduli to nearby groups and associations derived from the optical–infrared colour–luminosity and infrared Tully–Fisher relations is found to be $|.28|$ magnitude which is of the same order as the uncertainty estimated in the optical–infrared colour–luminosity relation. Considering the dispersion in the Tully–Fisher method, this is an encouraging result implying that the optical–infrared colour–luminosity relation, corrected for surface brightness, could provide an independent test of the distances derived from the Tully–Fisher relation.

6. The infrared luminosity function of 'field' galaxies is type–dependent. For a given value of α, the luminosity scale (M_K^*) for E-SOs is brighter than that of the spirals by about 0.70 magnitude. Since the substantial fraction of the near–infrared light of spirals comes from their bulges, the E-SOs and bulges of spirals may have different formation or evolutionary histories. Alternatively, the difference between the M_K^* values for E-SOs and spirals could be attributed to different mass distributions implying that a fraction of the mass of spirals is being used for disk formation.

   The infrared 'field' luminosity function for a given morphological type of galaxies is found to be the same as its optical counterpart shifted by the respective mean optical–infrared colour. This indicates that the properties of an infrared survey can be predicted from its optical luminosity function, the mean optical–infrared colour and allowing for the morphological type mix in the sample. Therefore, galaxies with strong/weak near–infrared emission cannot be very common.

7.2 Future Prospects

There are two types of projects which can be carried out in the coming years. Firstly, those which are practical in the immediate future using existing instruments and facilities. Secondly, those waiting for more sophisticated instruments and new technologies. In these last pages of this thesis I will concentrate on the prospective projects in the above two categories.

The 'field' E-SO galaxies studied in chapter 4 contains few objects with intermediate luminosities. Observations of E-SOs, spanning a luminosity range of $-22 < M_K < -18$ mag., are needed to improve the knowledge of the colour–luminosity relation over the entire luminosity range and to clarify the relationship between dwarfs and normal ellipticals.

Most of the fundamental results presented in this thesis are concerned with changes observed in the optical–to–infrared colours amongst galaxies of different types. However, a rigorous study of the horizontal branch population and star formation activities also requires U data. A programme to obtain high quality $UBVRI$ photographic and CCD data for all the galaxies studied in this thesis is currently in progress at Durham. This will substantially improve the quality of the optical data and with the infrared data presented here will provide the basis for a thorough comparison with the stellar synthesis models.

Regarding the stellar synthesis models, the tip of the asymptotic giant branch is still an unresolved issue. Synthetic models for composite stellar systems do not contain the full giant branches because these go beyond the tip observed in globular clusters. Observations of asymptotic giant branch stars in globular clusters beyond the tip in their giant branch, and their respective luminosity functions, are needed to improve the existing models. The models also do not contain horizontal branch stars because of their unknown isochrones and luminosity function and the ad hoc way they would have to be included. Until the appropriate luminosity function for these intermediate age stars is found and their evolution across the HR diagram is clearly understood, the horizontal branch population cannot be satisfactorily incorporated into the models.

Optical–to–infrared observations of $\sim$ 100 E-SO galaxies in Coma and other rich clusters are necessary to carry out a rigorous analysis of the environmental dependence of their infrared and optical–infrared colour–luminosity relations. Moreover, infrared data for a complete sample of E-SO galaxies in clusters can also be useful for constructing the cluster luminosity function at 2 μm. A comparison between the cluster and the bright end of the 'field' infrared luminosity functions will then indicate the extent to which the old population in clusters has been affected by dynamical evolution and will reveal possible differences in galaxy formation histories in clusters and general field.

Observations of colour gradients and CO indices of cD galaxies in clusters are needed to study the cooling flow observed in X – ray clusters. Support for the idea that cDs grow via star formation in the cooling flow comes from the X – ray data. These yield a total accreted gas mass equal to the total mass of stars required in the appropriate population synthesis models. These observations are of great importance in understanding the origin of the large mass of cD galaxies.

A study of the universality of $(J-K)-K$ relation for spirals in clusters is crucial for investigating the evolutionary history of their old population as a function of environment. The infrared colour–luminosity relations for spirals in clusters are only available for two nearby clusters, Persus and Pegasus, and *no* such detailed study has yet been carried out.

The sample of galaxies analysed in this thesis is too small to examine the morphological type–dependence of the infrared luminosity function amongst different classes of spirals. This type–dependence, if any, could have important implications in studying the contribution from the old population to the disk light and also in the formation of disks in intermediate to late–type spirals. It is also essential for constructing accurate number–magnitude count models in the infrared in order to compare them with the observed galaxy counts at 2 μm. With the introduction of the $UK9$ detector on the UKIRT, the size of the spiral sample studied in this thesis could be doubled in four nights. Optically selected complete surveys with high quality CCD data and well classified morphological types, accessible from the UKIRT, are now available. A program to obtain K magnitudes for these fields will significantly increase the amount of data for a thorough analysis of the morphological type–dependence of the spirals' infrared luminosity function.

In addition to the projects outlined above, which can be undertaken by using existing facilities and instruments, there are a number of important projects in the field of infrared astronomy which rely on the introduction of new technologies.

Infrared one–dimensional 32 element and two–dimensional 32 × 32 array detectors will be commissioned on the UKIRT by the end of 1986. They will have important applications in both spectroscopic and direct imaging and can extend medium resolution spectroscopy to the J, H and K passbands. Two–dimensional panoramic detectors can be used to construct deep infrared selected surveys ($K \sim 17$ mag.) to carry out a more rigorous comparison of the properties of infrared and optical selected samples and examine the results in chapter 6. This will be essential for establishing deep number–magnitude counts at 2 μm. Since the evolution at infrared wavelengths amongst galaxies is smaller than that in the optical, the infrared number–magnitude count models are more straightforward to construct. Moreover, the infrared observations of spirals will be useful for bulge/disk decontamination. The combination of the optical and infrared counts with self consistent models for both will be a powerful tool for separating the effects of luminosity evolution from those of cosmology.

The launch of the Hubble Space Telescope (HST) is presently planned for 1988. This will certainly make feasible many new and long–standing projects. Of particular interest to the investigations in this thesis is the construction of Near–Infrared Camera and Multi–Object Spectrometer (NICMOS) instrument for the HST. This instrument has both spectroscopic and imaging capability between the wavelengths 0.8 to 2.5 μm. Its multi–object spectrometer uses movable fibre optics to observe four different objects located within a 4 × 4 arcmin. field. NICMOS contains both Germanium (Ge) and Mercury Cadmium Telluride (Hg Cd Te) detectors which will be able to carry out essential near–ir observations.

One of the major goals of the HST is to establish an accurate distance scale. Optical studies of Cepheid variables are now scheduled for galaxies in the Virgo cluster. NICMOS would extend these observations to longer wavelengths. Moreover, since Cepheids are brighter in the infrared, NICMOS's capability will extend the range of possible observations to $K \sim 29$ mag. and therefore, in principle, could detect long period Cepheids beyond Virgo. This would greatly extend the range of distances measured with a primary distance indicator.

The high spatial resolution of NICMOS is ideal to observe close clusters of young stellar objects. These objects are very likely to have been formed from the same protostellar material and during the same epoch. Therefore, a comparison between the evolution of different mass protostars becomes possible which will extend our knowledge of the initial mass function to lower mass systems.

Following the highly successful mission of the Infrared Astronomical Satellite (IRAS), much effort is being put into the *Infrared Space Observatory* (ISO) due to be launched in 1992. The ISO consists of a 0.6 m diameter telescope equipped with a photometer, a 2–D infrared camera array and a spectrometer. The telescope and instruments will be cooled using liquid helium and hydrogen. A space infrared telescope cooled to $\sim 20° K$ and coupled to modern photoconductor detectors will give a sensitivity similar to that of the existing optical photographic

sky surveys. This could therefore provide a direct continuation of studies made by the HST to longer wavelengths. Of the many possible scientific areas where ISO will have an impact, the field of infrared extragalactic astronomy is expected to be of particular importance.

ISO will be most sensitive to the presence of cool stars. These stars contain strong molecular bands of CO at $2.3\,\mu m$ and H_2O at $2.7\,\mu m$ which can be used for population studies and to search for evolutionary effects. Moreover, a search could be carried out for massive galactic halos, composed of low–mass cool dwarf stars which have been postulated to account for the missing mass.

A detailed study of isolated dwarf galaxies can be carried out by the ISO. This would determine whether these galaxies, which contain hot stars, are young, in which case there will be few red giants, or 'rejuvenated', in which case many more evolved stars should be present.

The brightest objects in the Universe are mostly strong sources of infrared radiation, either thermal or non–thermal. Moreover, when an optical object is seen at large distances, the cosmic redshift makes it radiate more strongly in the infrared. The high sensitivity of the ISO will enable us to detect these objects at large distances and to investigate the possibility of using these infrared galaxies as standard candles to fix the cosmic distance scale.

ISO's high sensitivity will provide accurate spectroscopic photometry for the infrared excess galaxies detected by the IRAS. This will enormously enhance the astrophysical information about these objects and the source of their infrared excess.

A more speculative project for the ISO is to search for protogalaxies. These young galaxies are expected to be bright objects with a very high star formation rate. They have not yet been observed in optical wavebands and the counts of faint galaxies do not show the type of excess which would be expected if a population of bright galaxies of this type was present. However, these objects may be so dusty that all the radiation is absorbed by dust and then re–radiated thermally in the far–infrared. While the discovery of such objects in a deep survey by ISO will bring the study of first generations of galaxies within our observational reach, their lack of detection would force us to push back the epoch of galaxy formation to presently unobservable redshifts.

References

Aaronson, M. 1977 Ph.D Thesis, Harvard University.

Aaronson, M. 1978 Astrophys. J., **221**, L103.

Aaronson, M., Cohen, J. G., Mould, J. and Malkan, M. 1978 Astrophys. J., **223**, 824.

Aaronson, M., Huchra, J. and Mould, J. 1979 Astrophys. J., **229**, 1.

Aaronson, M., Mould, J. and Huchra, J. 1980 Astrophys. J., **237**, 655.

Aaronson, M., Mould, J., Huchra, J., Sullivan III, W.T., Schommer, R.A., and Bothun, G.D. 1980 Astrophys. J., **239**, 12.

Aaronson, M., Persson, E. and Frogel, J. 1981 Astrophys. J., **245**, 18.

Aaronson, M., et al 1982a Astrophys. J. Suppl., **50**, 241.

Aaronson, M., Huchra, J., Mould, J., Schecter, P. and Tully, B. 1982b Astrophys. J., **258**, 64.

Aaronson, M. and Mould, J. 1983 Astrophys. J., **265**, 1.

Aaronson, M., Bothun, G., Mould, J.R., Huchra, J., Schommer, R.A., and Cornell, M.E., 1986 Astrophys. J.,**302**, 536

Abell, G.O., 1962 *In problems of Extragalactic Research* ed. C.G.McVitte (NewYork:Macmillan), 213

Abell, G.O., 1976 *In Galaxies and the Universe* eds. A.Sandage, M.Sandage and J.Kristian 601 Chicago university press

Baum, W. 1959 Publ Astron. Soc. Pac., **71**, 106.

Bautz, L.P. and Abell, G.O., 1973 Astrophys. J.,**184**,709.

Bean A.J. 1983, Ph.D. Thesis, University of Durham.

Bean A.J., Efstathiou, G.P., Ellis, R.S., Peterson, B.A. and Shanks, T. 1983 Mon. Not. R. Astr. Soc., **205**, 605.

Bertola, F. , Capaccioli, M. and Oke, J.B 1982 Astrophys. J., **254**, 494.

Boroson, T. 1981 Astrophys. J. Suppl., **46**, 177.

Bosma, A. 1985 Astron. Astrophys., **149**, 482.

Bothun, G. and Caldwell, N., 1984 Astrophys. J. **280**, 528.

Bothun, G.D., Romanishin, W., Strom, S.E. and Strom, K.M. 1984 Astron. J., **89**, 1300.

Bothun, G.D., Mould, J., Schommer, R.A. and Aaronson, M. 1985a Astrophys. J., **291**, 586.

Bothun, G.D., Mould, J.R., Wirth, A. and Caldwell, N., 1985b, Astron. J, **90**, 697.

Bothun, G.D., Aaronson, M., Schommer, R., Huchra, J., Mould, J. and Sullivan, W. 1985c, Astrophys. J. Suppl., **57**, 423.

Bottinelli, L., Gouguenheim, G., Paturel, G., and de Vaucouleurs, G. 1980, Astrophys. J., **242**, L153.

Brown, G.S. and Tinsley, B.M. 1974 Astrophys. J.,**194**,555.

Bruzual, G. 1981 Ph.D Thesis, University of California, Berkely.

Bruzual, G. and Kron, R.G. 1980 Astrophys. J., **241**, 25.

Burstein, D. 1982 Astrophys. J., **253**, 539.

Caldwell, N. 1983 Astron. J., **88**, 804.

Cohen, J. G., Frogel, J.A., and Persson, S.E., 1978, Astrophys. J., **222**, 165.

Couch, W.J. 1982 Ph.D Thesis, Australian National University.

Davis M., and Peebles P.J.E., 1983 Ann. Rev. Astron. Astrophys.,**21**, 109.

de Vaucouleurs, G. 1961 Astrophys. J. Suppl., **5**,233.

de Vaucouleurs, G., de Vaucouleurs, A. and Corwin, H. 1976
Second Reference Catalogue of Bright Galaxies
(Austin: University of Texas press) (RC2).
de Vaucouleurs, G. 1977b in *The Evolution of Galaxies and Stellar Populations*
eds. Tinsley, B. M. and Larson, R. (Yale University Observatory).
de Vaucouleurs, G. 1977a Astrophys. J. Suppl, **33**, 211.
de Vaucouleurs, G., Buta, R., Bottinelli, L., Gouguenheim, L.,
and Paturel, G., 1982 Astrophys. J., **254**, 8.
Dressler,A. 1978 Astrophys. J.,**223**,765.
Dressler,A., Thompson, and Schectman, S. 1985 Astrophys. J., **288**, 481.
Efron, B. 1979 Ann. Statist.,**7**,1.
Efstathiou, G.P., Ellis, R.S., Shanks, T., Bean, A.J. and
Peterson, B.A., 1987, in preparation.
Elias, J., Frogel, J., Mathews, K. and Neugebauer,G. 1982, Astron. J., **88**, 1029.
Ellis, R.S. and Allen, D.A. 1983 Mon. Not. R. astr. Soc., **203**, 685.
Ellis, R.S. 1982, *in origin and early evolution of galaxies.*
eds. Jones, B.J.T. and Jones, J.E., D. Reidel Publ.Co. P.255.
Ellis, R.S. 1984 in *Spectral Evolution of Galaxies*,
RAL Publications 84-008, ed. Gondhalekhar, P.M.
Faber, S. 1973 Astrophys. J., **179**, 731.
Felten, J.E. 1977 Astron. J., **82**,861.
Fisher, J.R. and Tully, R.B. 1981 Astrophys. J. Suppl, **47**, 139.
Freeman, K.C., 1970 Astrophys. J., **160**, 811.
Frogel, J.A., Persson, S.E., Aaronson, M. and Matthews, K.
1978 Astrophys. J., **220**, 75.
Frogel, J.A., Persson, S.E. and Cohen, J.G. 1980, Astrophys. J. **240**, 785.
Frogel, J.A., 1985 Astrophys. J., **298**, 528.
Green, E.M., Demarque, P., and King, C.R., 1985, B.A.A.S., **16**, 997
Griersmith, D. 1980a Astron. J., **85**, 1135.
Griersmith, D. 1980b Astron. J., **85**, 1295.
Griersmith, D., Hyland, A.R. and Jones, T.J. 1982, Astron. J., **87**, 1106.
Gunn, J. and Oke, J.B., 1975, Astrophys. J., **195**,255.
Hall, P. and Mackay, C.D. 1984 Mon. Not. R. Ast. Soc., **210**,979.
Huchra, J., Davis, M., Latham, D. and Tonry, J. 1983,
Astrophys. J. Suppl. **52**, 89 (CFA).
Hubble, E. 1926, Astrophys. J., **64**, 321.
Hubble, E. and Tolman, R.C. 1935 Astrophys. J., **82**,302.
Johnson, H.L. 1966, in *Nebulae and Interstellar Matter*,
ed. B.M. Middlehurst and L.H. Aller (Chicago:
University of Chicago press), p.167
Kennicutt, R.C., Jr., 1983, Astron. J., **88**, 483.
Kiang, T.D. 1961 Mon. Not. R. Ast. Soc., **122**,263.
King, C.R. and Ellis, R.S., 1985, Astrophys. J., **288**, 456
Kirshner, R.P., Oemler, A., and Schechter, P.L., 1978, Astron. J., **83**, 1549
(KOS).
Kraan-Kortweg, R.C. 1983, Astron and Astrophs **125**, 109.
Lampton, M., Margon, B. and Bowyer, S. 1976 Astrophys. J., **208**,177.
Lilly, S.J. 1984, in *Spectral Evolution of Galaxies*
RAL publications 84–008, ed. Gondhalekhar, P.M., P.179
Lilly, S.J. and Longair, M.S. 1982 Mon. Not. R. astr. Soc., **199**, 1053.

Lin, D.N.C., and Faber, S.M., 1983, Astrophys. J., **266**, L21.
Longmore, A.J., Fernley, J.A., and Jameson, R.F. 1986,
Mon. Not. R. ast. Soc., **220**, 279.
Longo, G. and de Vaucouleurs, A., 1983 University of Texas
Monographs in Astronomy No. 3.
Martin R., and Lutz R.K. 1979 in *Image Processing in Astronomy*,
eds. G. Sedmak, M. Cappaccioli and R.J. Allen (Observatorio
Astronomico di Trieste), p. 211
McClure, R.D., Cowley, A.P., and Crampton, D., 1980, Astrophys. J., **236**, 112.
McGonegal, R., McAlary, C.W., McLaren, R.A., and Madore, B.F., 1983
Astrophys. J., **269**, 641.
Miller, R.G. 1974 Biometrika, **61**,1.
Mould, J., Aaronson, M. and Huchra, J. 1980 Astrophys. J. **238**, 458.
O'Connell, R.W., 1976, Astrophys. J., **206**, 370.
O'Connell, R.W., 1980, Astrophys. J., **236**, 430.
O'Connell, R.W., 1983, Astrophys. J., **267**, 80.
Peebles, P.J.E. and Hauser, M.G. 1974 Astrophys. J. Suppl., **28**,19.
Peebles, P.J.E. 1979a, Astron. J., **84**, 730.
Peebles, P.J.E. 1979b, *In Scientific Research with the Space Telescope*
IAU Symp. 54. ed. Longair, M.
Pence, W.D. 1976 Astrophys. J., **203**,39.
Persson,S.E., Frogel, J.A. and Aaronson, M. 1979, Astrophys. J. Suppl., **39**, 61.
Persson, S.E., Aaronson, M., Cohen, J.G, Frogel, J.A., and
Matthews, K., 1983, Astrophys. J., **266**, 105.
Peterson, B.A., Ellis, R.S., Kibblewhite, E.J., Bridgeland, M., Horne, D.
and Hooley, T. 1979 Astrophys. J., **233**,L109
Peterson, B.A., Ellis, R.S., Efstathiou, G., Shanks, T., Bean, A.J.
Fong, R. and Zou, Z. Zen–Long 1986, Mon. Not. R. astr. Soc., **221**, 233.
Quenouille, M.H. 1956 Biometrika, **43**,353.
Rieke, G.H., 1978, Astrophys. J., **226**, 550.
Rieke, G.H., and Lebofsky, M.J., 1978, Astrophys. J., **220**, L37.
Rieke, G.H., and Lebofsky, M.J., 1979,
Ann.Rev.Astron and Astrophys, **17**, 477.
Roberts, M.S., 1978, Astron. J., **83**, 1026.
Rood, H.J. and Baum, W.A. 1967, Astron. J., **72**, 398.
Rubin, V.C., Burstein, D. and Thonnard, N. 1980, Astrophys. J., **242**, L149.
Sandage, A. 1961 *The Hubble Atlas of Galaxies*
(Carnegie Institute of Washington).
Sandage, A. 1972 Astrophys. J., **176**, 21.
Sandage, A. 1973 Astrophys. J., **183**, 711.
Sandage, A. 1975 Astrophys. J., **202**, 563.
Sandage, A. and Tammann, G.A., 1974 Astrophys. J., **194**, 559.
Sandage, A. and Tammann, G.A., 1976 Astrophys. J., **210**, 7.
Sandage, A. and Visvanathan, N. 1978a Astrophys. J., **223**, 707.
Sandage, A. and Visvanathan, N. 1978b Astrophys. J., **225**, 742.
Sandage, A., Tammann, G.A. and Yahil, A. 1979 Astrophys. J., **232**, 352.
Sandage, A., Binggeli, B. and Tammann, G.A. 1985, Astron. J., **90**, 1759.
Schechter, P. 1976 Astrophys. J., **203**, 297.
Schmidt, M. 1968 Astrophys. J., **151**, 393.
Scoville, N.Z., Becklin, E.E., Young, J.S., and Capps, R.W., 1983

Astrophys. J., 271, 512.
Shanks, T., Bean, A.J., Efstathiou, G.P., Ellis, R.S.,
Fong, R. and Peterson,B.A. 1984 Astrophys. J., 274, 529.
Shanks, T., Stevenson, P.R.F., Fong, R. and MacGillivray 1984
Mon. Not. R. Ast. Soc., 206, 767.
Shapiro, S.L. 1971 Astron. J. 76, 291.
Simien, G. and de Vaucouleurs, G. 1983
Internal Kinematics and Dynamics of Galaxies,
ed. E. Athanassoula, IAU Symp. 100, p. 375.
Simien, G. and de Vaucouleurs, G. 1986, Astrophys. J., 302, 564.
Sitko, M.L. 1984 Astrophys. J., 286, 209.
Spinrad, H. 1977, *The Evolution of Galaxies and Stellar Populations*,
eds. B.M. Tinsely and R.B. Larson,
New Haven. Yale Univ. Obs. P. 301
Struck-Marcell, C. and Tinsely, B.M. 1978 Astrophys. J., 221, 562.
Thuan, T.X. 1983 Astrophys. J., 268, 667.
Tinsely, B.M. 1972, Astron and Astrophys., 20, 383.
Tinsely, B.M. 1973, Astrophys. J., 184, L41.
Tinsely, B.M., and Gunn, J.E., 1976 Astrophys. J., 203, 52.
Tonry, J. and Davis, M. 1979, Astron. J., 84, 1511.
Tukey, J.W. 1958 Ann. Math. Statist., 29, 614.
Tully, B., Mould, J. and Aaronson, M. 1982 Astrophys. J., 257, 527.
Turnrose, B.E., 1976, Astrophys. J., 210, 33.
van den Bergh, S. 1960 Pub. David Dunlop Obs., Vol 2, No 6.
van den Bergh, S. 1981 Astrophys. J., 248, L9.
Visvanathan, N. and Sandage, A. 1977 Astrophys. J., 216, 214.
Visvanathan, N. 1983, Astrophys. J., 275, 430.
Weedman, D.W. 1977, Ann.Rev.Astron.Astrophys., 15, 69.
Whitmore, B.C. 1984 Astrophys. J., 278, 61.
Wyse, R. 1982 Mon. Not. R. astr. Soc., 199, 1P.
Yahil, A. 1986 preprint
Zinn, R. 1980, Astrophys. J. Suppl., 42, 19
Zwicky, F. 1957 Morphological Astronomy (Berlin: Springer Verlag), 171.